Respiration patterns in the dark ocean

Olivier Sulpis[1], David Trossman[2], Mark Holzer[3], Emil Jeansson[4], Siv K Lauvset[5], and Jack J Middelburg[6]

[1]CEREGE
[2]University of Maryland, College Park
[3]University of New South Wales
[4]NORCE Norwegian Research Centre, Bjerknes Centre for Climate Research
[5]NORCE Norwegian Research Centre
[6]Utrecht University

March 1, 2023

Abstract

In the dark ocean, respiring organisms are the main sink for dissolved oxygen. The respiration rate in a given seawater volume can be quantified through dissolved oxygen drawdown or organic matter consumption as a function of time. Estimates of dissolved oxygen utilization rates (OUR) abound in the literature, but are typically obtained using proxies of questionable accuracy, often with low vertical resolution, and neglecting key regions such as the Southern and Indian oceans. Respiration rates based on particulate (POC) or dissolved (DOC) organic carbon are also sparsely observed and for DOC unavailable in many regions. Consequently, the relative contributions of POC or DOC as a respiration substrate in the dark ocean are unknown. Here we use recent datasets of true oxygen utilization, seawater age, and DOC to derive OUR and DOC consumption-rate profiles in 10 oceanic regions. We demonstrate that although DOC and POC consumption rates are globally consistent with OUR, they underestimate OUR in the deep, suggesting strong oxygen utilization at the seafloor. In the abyss, we find a negative correlation of DOC consumption rate with seawater age, suggesting that DOC reactivity decreases along the deep branch of the conveyor circulation. Our results highlight that benthic organisms are sensitive to perturbations in the surface production of organic matter and to large-scale circulation changes that affect its supply to the abyss.

Respiration patterns in the dark ocean

Olivier Sulpis[1,2], David S. Trossman[3], Mark Holzer[4], Emil Jeansson[5], Siv K. Lauvset[5] & Jack J. Middelburg[1]

[1]Earth Sciences, Utrecht University, Utrecht, The Netherlands
[2]CEREGE, Aix Marseille Univ, CNRS, IRD, INRAE, Collège de France, Aix-en-Provence, France
[3]Earth System Science Interdisciplinary Center, University of Maryland-College Park, College Park, USA
[4]Department of Applied Mathematics, School of Mathematics and Statistics, University of New South Wales, Sydney, Australia
[5]NORCE Norwegian Research Centre, Bjerknes Centre for Climate Research, Bergen, Norway

Key points

- *DOC* is important for microbial respiration in the abyssal ocean where the DOC consumption rate decreases with seawater mean age
- About 8% of O_2 utilization in the midnight zone and in the abyssal ocean is attributed to processes occurring at the seafloor
- Total dark ocean O_2 consumption (907 Tmol O_2 a^{-1}) is balanced by sediment O_2 (74 Tmol O_2 a^{-1}) and organic C consumption (727 Tmol C a^{-1})

Abstract

In the dark ocean, respiring organisms are the main sink for dissolved oxygen. The respiration rate in a given seawater volume can be quantified through dissolved oxygen drawdown or organic matter consumption as a function of time. Estimates of dissolved oxygen utilization rates (*OUR*) abound in the literature, but are typically obtained using proxies of questionable accuracy, often with low vertical resolution, and neglecting key regions such as the Southern and Indian oceans. Respiration rates based on particulate (*POC*) or dissolved (*DOC*) organic carbon are also sparsely observed and for *DOC* unavailable in many regions. Consequently, the relative contributions of *POC* or *DOC* as a respiration substrate in the dark ocean are unknown. Here we use recent datasets of true oxygen utilization, seawater age, and *DOC* to derive *OUR* and *DOC* consumption-rate profiles in 10 oceanic regions. We demonstrate that although *DOC* and *POC* consumption rates are globally consistent with *OUR*, they underestimate *OUR* in the deep, suggesting strong oxygen utilization at the seafloor. In the abyss, we find a negative correlation of *DOC* consumption rate with seawater age, suggesting that *DOC* reactivity decreases along the deep branch of the conveyor circulation. Our results highlight that benthic organisms are sensitive to perturbations in the surface production of organic matter and to large-scale circulation changes that affect its supply to the abyss.

1. Introduction

Oxygen concentrations in seawater span a wide range, resulting from exchanges with the atmosphere and sediments, production by photosynthesis, respiration by heterotrophs feeding on organic substances and (microbial) oxidation of reduced metabolites such as ammonium. Most organisms in the ocean interior rely on oxygen for respiration, and are thus vulnerable to the current growing deoxygenation observed across the oceans (e.g., Keeling & Garcia, 2002; Whitney et al., 2007; Helm et al., 2011; Oschlies et al., 2018). Yet, the nature of the organic material being used as an energy source for respiration, the rate of respiration, and its spatial distribution are still poorly known in the dark ocean. This impedes accurate assessments of the response of respiring marine organisms to environmental changes.

Marine organic carbon comprises particulate (*POC*) and dissolved (*DOC*) forms, operationally separated by a size limit (Arístegui et al., 2009). More than 99% of the respired *POC* in the dark ocean originates from invertebrate life forms (del Giorgio & Duarte, 2002), such as archaea, bacteria, protozoa, zoo- and phytoplankton, mostly packed within organic aggregates (Mare, 1942; Johannes, 1965; Pomeroy & Johannes, 1968). While organic matter from living organisms is fresh and labile, organic matter from dead organisms and settling aggregates is a heterogeneous mixture of compounds from various origins whose reactivity mostly decreases with its age (Middelburg, 2019; Dittmar et al., 2021). Ocean *DOC* is also characterized by a continuum of composition and reactivity (Hansell, 2013; Hansell & Carlson, 2014), but plays a more ambiguous role in respiration as it is both a substrate and a byproduct of organic matter degradation, released via leakage, unbalanced growth, viral lysis or incomplete digestion and solubilization (Hansell & Carlson, 2014; Middelburg, 2019; Dittmar et al., 2021). What is the reactivity of the *DOC* pool as a function of water depth, how does it vary among regions, and what is the importance of *DOC* relative to *POC* in marine respiration are still unanswered questions.

Globally, marine respiration mostly occurs in the ocean's euphotic layer (del Giorgio & Duarte, 2002). Out of ~50 Gt C a^{-1} of net surface-ocean primary production, between 5 and 12 Gt C a^{-1} are eventually exported as sinking *POC* and advected/diffused *DOC* to the ocean interior (Laws et al., 2000; Andersson et al., 2004; Dunne et al., 2007; Henson et al., 2011; Siegel et al., 2014; DeVries & Weber, 2017; Middelburg, 2019). It is believed that ~80% of the organic carbon exported from the euphotic layer is respired, degraded, and returned to dissolved inorganic carbon in the dark water column, and ~20% at the seafloor (Jahnke, 1996; Andersson et al., 2004; Middelburg, 2019). However, estimates of respiration rates vary widely, with rates estimated from measured or modeled *POC*-flux attenuation usually being much lower than those based on measured respiratory activity, which provides integrated carbon consumption rate over a specific depth range, predicting global, dark-ocean respiration rates as high as 33 Gt C a^{-1} (Arístegui et al., 2003). A more direct approach involves using changes in dissolved oxygen as a function of time, but these data are either limited to the surface layer where incubation time can be short or based on the combination of dissolved oxygen measurements and water-age estimates.

Once a parcel of seawater leaves the surface and enters the ocean interior, its dissolved oxygen concentration should decrease with time, as oxygen is being used by respiring organisms (Craig, 1971). Apparent Oxygen Utilization (*AOU*) is the difference between the dissolved oxygen concentration of seawater at equilibrium with the atmosphere at a given temperature and salinity and the measured dissolved oxygen concentration. *AOU* has been used to estimate oxygen utilization rates (*OUR*) by dividing *AOU* by seawater age (Sarmiento et al.,

1990; Feely et al., 2004; Karstensen et al., 2008). However, this is an imperfect approach because *AOU* usually overestimates oxygen utilization because water parcels are rarely at equilibrium with the atmosphere when they start their journey to the ocean interior (Ito et al., 2004; Duteil et al., 2013; Koeve & Kähler, 2016; DeVries & Holzer, 2019; Holzer, 2022). Alternatively, we can calculate oxygen utilization rates as the dissolved oxygen changes over a given amount of time (Jenkins, 1982; Hinga, 1985; Sonnerup et al., 2013, 2015). This reduces uncertainties related to air-sea disequilibrium, but would require a larger amount of data and accurate seawater ages and implicitly assumes steady-state conditions. Both approaches, i.e., *AOU* divided by seawater age and oxygen changes regressed againts multiple seawater ages, have provided some historical *OUR* estimates in various regions of the Pacific and Atlantic, but the depth resolution is often low, and historically data-scarce oceanic regions such as the Indian or Southern oceans have been largely neglected. Additionally, regional comparisons are difficult because *OUR* depth profiles across ocean basins are not often obtained with the same method.

Our purpose here is to rigorously assess the depth and regional patterns of respiration rates in the dark ocean, using three independent proxies: (i) changes in dissolved oxygen along water-mass pathways, (ii) changes in *DOC* concentration along water-mass pathways and (iii) changes in *POC* sinking fluxes. For (i) and (ii), we use a recently published dataset of Transit Time Distribution (TTD) ages (Jeansson et al., 2021), which provides accurate water-mass-age estimates considering mixing occurring into the ocean interior (Waugh, 2003), a novel True Oxygen Utilization (*TOU*) data product that accounts for air-sea disequilibrium (DeVries & Primeau, 2011; DeVries, 2014; DeVries & Holzer, 2019; Holzer, 2022), and a recently published dataset of quality-controlled, seawater DOC concentration (Hansell et al., 2021), to derive depth profiles of *OUR* and *DOC* consumption rate in 10 major oceanic regions. By separating the water column in three depth realms (twilight zone, midnight zone and abyss, defined later) we demonstrate that although *DOC* and *POC* consumption rates are consistent with *OUR* at a global scale, they persistently underestimate *OUR* in the deeper part of the water column. This suggests strong, ubiquitous oxygen utilization at the seafloor that is not reflected in the *POC* and *DOC* data. These results have implications for Anthropocene-ocean ecosystems, as they highlight that abyssal microbial and animal communities are sensitive to any perturbation in organic material delivery to the deep ocean originating from the surface.

2. Methods

2.1. True oxygen utilization (*TOU*)

True oxygen utilization (*TOU*, Fig. 1) was computed as the difference between the preformed and measured oxygen concentrations. Unlike *AOU*, *TOU* is a model tracer which accounts for oxygen saturation states other than 100% (mostly lower) in surface water at the time of water mass formation as well as interior ocean mixing in the presence of nonlinearity in the solubility of oxygen (Ito et al., 2004; Koeve & Kähler, 2016). Preformed oxygen was estimated by propagating the GLODAPv2.2016 (Lauvset et al., 2016) mapped climatologies of surface oxygen into the ocean interior using OCIM2, a steady-flow data-assimilated ocean circulation inverse model in its 24-level, 2x2-degree control version (DeVries and Holzer, 2019). This model is constrained by observed ^{14}C, CFCs, ^{3}He, surface heat, freshwater fluxes, sea-surface height, temperature and salinity (Holzer et al., 2018; DeVries & Holzer, 2019; Holzer, 2022). Preformed and observed oxygen concentrations were then linearly interpolated in three dimensions from the OCIM2 grid back to GLODAPv2 coordinates. This *TOU* product

compares well with other recent, independent *TOU* estimates (Carter et al., 2021; Cassar et al., 2021), see Fig. S1.

To assess the uncertainty in the model-predicted preformed oxygen concentrations, we compared the preformed oxygen as predicted by 7 different versions of OCIM2 having different vertical resolution (24 levels or 48 levels) and/or different eddy diffusivities (DeVries and Holzer, 2019; Holzer et al., 2021). The mean standard deviation of the preformed oxygen across these 7 simulations was ~6%. The uncertainty of the GLODAPv2 oxygen data is estimated to be about 1% (Olsen et al., 2016). To reflect both the uncertainty surrounding preformed oxygen and that surrounding measured oxygen, we set the relative uncertainty of the *TOU* estimates to a conservative value of 10%.

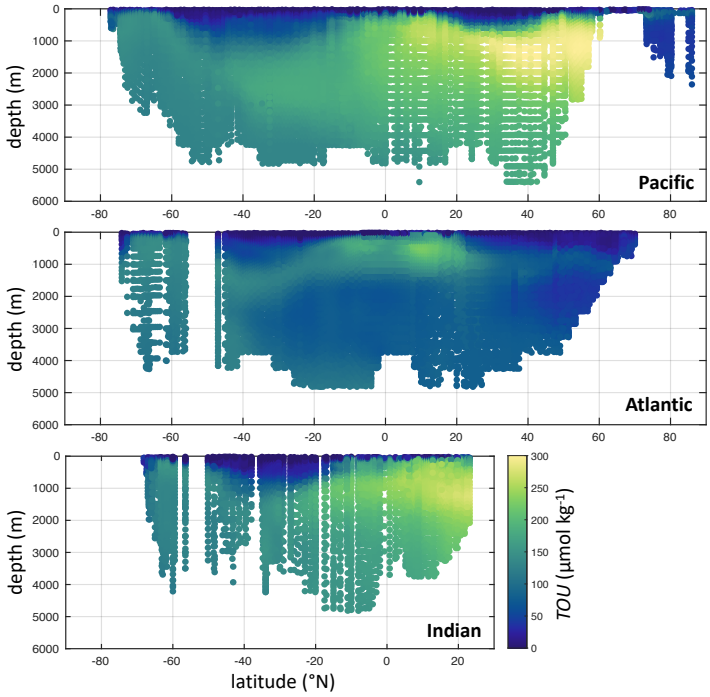

Figure 1. *TOU* depth profiles in the Pacific (all data between 160°W and 180°W), Atlantic (all data between 20°W and 30°W) and Indian (all data between 60°E and 80°E) Oceans.

2.2. Seawater age

The age of seawater was obtained using a two-parameter (mean and width) transit-time-distribution (TTD) approach based on measured GLODAPv2.2016 CFC-12 concentrations (Olsen et al., 2016), assuming a ratio of mean/width of 1. Unlike traditional tracer-based ages, TTD ages keep track of seawater mixing history by including corrections for mixing during transport away from the surface ocean. We assume minimal bias associated with the resulting TTD ages in regions with more than one peak in the TTD (e.g., portions of the Southern Ocean; Trossman et al., 2014) and that the TTD ages are valid up to 300 years from the limited (~80 year) time history of the ventilation tracers used to estimate the TTD. The TTD age product (Jeansson et al., 2021) is available online at https://www.ncei.noaa.gov/access/ocean-carbon-data-system/oceans/ndp_108/ndp108.html. Because of the relatively short history of CFC-12 and the anthropogenic influence on ^{14}C mean ages in younger waters, for samples with CFC-12 TTD ages greater than 300 years, we instead use the seawater 'mean age' from (Gebbie & Huybers, 2012), who applied an inverse modeling technique on GLODAPv1.1 ^{14}C data (Key

et al., 2004). To avoid an abrupt transition between CFC-12 TTD ages and ^{14}C mean ages, for samples with TTD ages between 200 and 300 years, a transition function is applied to compute ages as a weighted average between the CFC-12 TTD ages and ^{14}C mean ages. For all water masses younger than 200 years, we used the CFC-12 TTD ages. This composite seawater age product is shown in Fig. 2. We set the overall relative uncertainty associated with seawater ages to 20%, which should encompass both the uncertainty associated with the TTD method reported by He et al. (2018) and the uncertainty associated with ^{14}C mean ages (Gebbie & Huybers, 2012), neglecting the influence of exotic waters such as from groundwater seepage, hydrothermal vents or ice sheets. This composite age product is broadly consistent within its uncertainty with ages from the OCIM2 model in its 24-level, 2x2-degree control version (DeVries and Holzer, 2019), see Fig. S2.

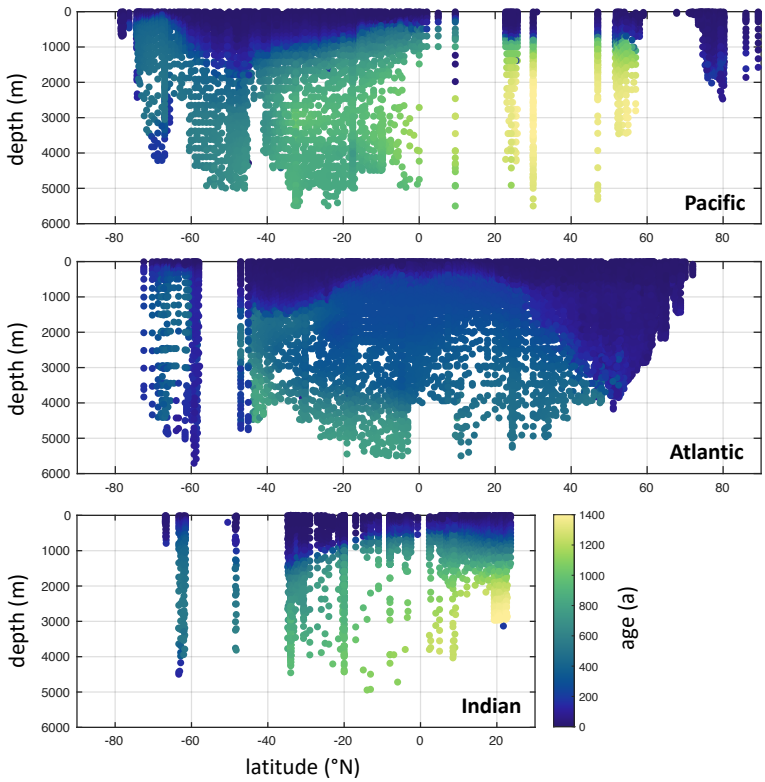

Figure 2. Seawater age depth profiles in the Pacific (all data between 160°W and 180°W), Atlantic (all data between 20°W and 30°W) and Indian (all data between 60°E and 80°E) Oceans.

2.3. Regions

We grouped the data by region using the global open-ocean core biome distribution of Fay and McKinley (2014), which is defined using criteria based on sea surface temperature, chlorophyll-a concentration, sea-ice fraction and maximum mixed-layer depth. Thus, the regions considered for the present analysis are distinguished based on ocean surface biogeochemical factors rather than water masses or topography (Fig. 3a). To avoid issues associated with under-sampled, narrow regions, we merged four biome pairs as defined by Fay and McKinley (2014) into four distinct regions: the equatorial Pacific east and west, the subpolar and the subtropical seasonally stratified North Pacific, the subpolar and the subtropical seasonally stratified North Atlantic, and the subpolar and the subtropical seasonally stratified Southern Ocean. We also excluded the Arctic and southernmost biomes, which are seasonally covered by sea ice, due to fewer data available, and due to the complexity of

isopycnal contours in those regions. Thus, we analyze ten biogeochemically distinct regions here. The exclusion of high-latitude systems implies that our global estimates are conservative. We acknowledge that the choice of regions is subjective, and that other sets of biogeochemical regions have been defined for the mesopelagic realm (Reygondeau et al., 2017; Sutton et al., 2017). Applying our analysis in those regions could be the focus of future work.

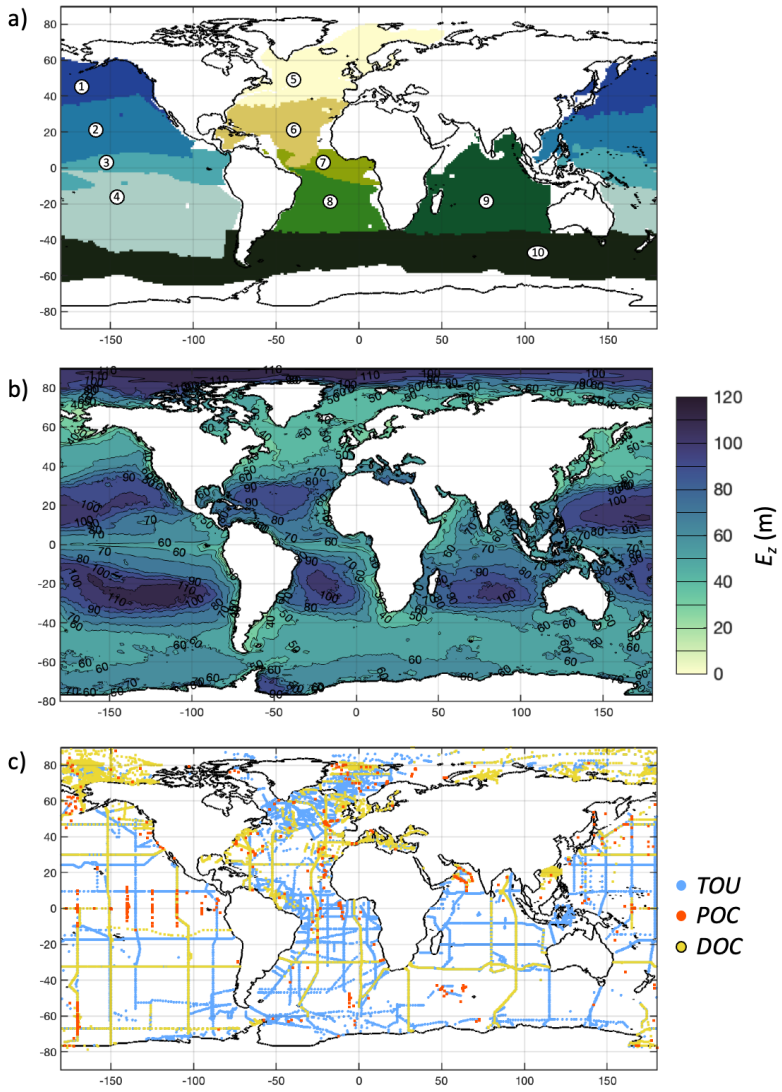

Figure 3. a) Geographical boundaries of the 10 regions used for our study: 1, subpolar North Pacific, 2, subtropical North Pacific, 3, Equatorial Pacific, 4, subtropical South Pacific, 5, subpolar North Atlantic, 6, subtropical North Atlantic, 7, Equatorial Atlantic, 8, subtropical South Atlantic, 9, Indian Ocean and 10, Southern Ocean. **b)** Euphotic zone depth, where contour lines mark 10-m intervals. **c)** Locations of *TOU* (blue circles), *POC* (orange circles) and *DOC* (yellow circles) data points.

2.4. Euphotic-zone-referenced depth metrics

As pointed out by Buesseler et al. (2020), depth patterns related to the marine biological carbon pump can appear quite different depending on whether the *POC* fluxes are assessed at a fixed reference depth (e.g. the air-sea interface) or relative to the depth at the base of the euphotic zone (E_z). Because E_z varies with location, E_z should be a preferred reference depth when comparing among regions (Buesseler et al., 2020). We computed E_z (Fig. 3b) as a

function of the surface chlorophyll concentration following Eq. (10) in the work of Morel et al. (2007), which corresponds to the depth at which the downward photosynthetically active radiation falls to 1% of its subsurface value. Surface chlorophyll concentrations were taken from the Operational Mercator Ocean biogeochemical global ocean analysis and forecast system at 1/4 degree (Global Monitoring and Forecast Center, 2021), averaged between the months of January 2019 and September 2021, which corresponds at the time of writing to all the data available from this source. E_z was then spatially averaged in each region. Regionally-averaged E_z is the deepest in the subtropical North Pacific (89 m below sea surface) and the shallowest in the subpolar North Atlantic (46 m below sea surface). All depth profiles shown here are expressed relative to E_z.

In addition to continuous depth profiles, we also express results in terms of three predefined depth zones: (i) the *twilight zone*, between E_z and E_z + 500 m, (ii) the *midnight zone* (Roth, 2020) between E_z + 500 m and 3 km depth (below sea level), and (iii) the *abyss*, between 3 km depth and the bottom.

2.5. O_2 utilization rate (*OUR*)

For each region, *TOU* data were sorted according to increasing water neutral density (γ), taken from GLODAPv2 (Olsen et al., 2016), and placed into bins centered around predefined γ values; these bins constitute the isopycnals. The density bins span a broad density range, from γ = 20.0 to γ = 28.8 kg m^{-3}, and are separated by a γ increment kept constant over the entire γ range, that randomly varies between 0.0005 and 0.01 across 5000 Monte Carlo simulations. That is, for each Monte Carlo simulation, isopycnals were centered around different neutral density values and included a different amount of data points. This Monte Carlo approach also allows us to propagate the *TOU* uncertainty (10%) and the age uncertainty (20%) into the final respiration rates, as well as to obtain *OUR* estimates centered around different isopycnals and to maximize the depth coverage of the *OUR* profiles. For each density bin, we performed a linear fit of *TOU* versus seawater age using the MATLAB *fitlm* function and the built-in 'robust regression' option that reduces outlier effects. From each fit, we extract the slope, standard error associated with the slope, and the p-value testing the null hypothesis of zero slope, i.e., that *TOU* and age are independent. The slope of the *TOU*-age linear relationship corresponds to *OUR* expressed in μmol kg^{-1} a^{-1}. Only *OUR* resulting from a statistically significant relationship between *TOU* and age ($p < 0.05$) were retained.

To test the robustness of our approach, we also replicated our entire analysis using simply GLODAPv2 oxygen concentrations ([O_2]), instead of *TOU* (Fig. S6). That is, rather than computing *OUR* as the slope of a linear fit of *TOU* versus seawater age, we compute another version of *OUR*, defined as the slope of a linear fit of measured [O_2] versus seawater age along a given isopycnal. At steady state, the main difference between the [O_2] and the *TOU* approaches is how water mixing is dealt with. All results described in this study are based on the *TOU* approach, and a brief comparison with results obtained from the [O_2] approach is provided in the discussion section 4.1.

2.6. *DOC* consumption rate

The procedure to estimate *DOC* consumption rate profiles is identical to that described in the previous subsection for *OUR*, except that instead of *TOU*, *DOC* concentrations are used. We used the dissolved organic matter dataset of Hansell et al. (2021) that includes quality-controlled, in situ *DOC* concentration measurements collected between 1994 and 2019 in all

10 regions, representing a total of more than 90,000 data points, see Fig. 3c. *DOC* concentrations, shown in Fig. 4, were always highest near the ocean surface, commonly above 100 µmol kg^{-1}, and decreased with depth to stabilize at 35-40 µmol kg^{-1}. Seawater ages were assigned to each *DOC* estimate by linearly interpolating the seawater ages shown in Fig. 2 in three dimensions to match the coordinates of the *DOC* samples. Seawater neutral density was absent from the *DOC* dataset, but present in the GLODAPv2 data product. Thus, for each of the 10 regions, whose bounds roughly follow outcropping isopycnal contours, we fitted a linear regression model to predict GLODAPv2 neutral density as a function of GLODAPv2 absolute salinity and conservative temperature. In turn, in each region, the regression model was used to compute the neutral density associated with each *DOC* sample based on the sample's conservative temperature and absolute salinity, calculated with the TEOS-10 toolbox (McDougall & Barker, 2011). Net *DOC* consumption rates are expressed in µmol kg^{-1} a^{-1}, where a positive value indicates *DOC* consumption, and a negative value indicates *DOC* production or input.

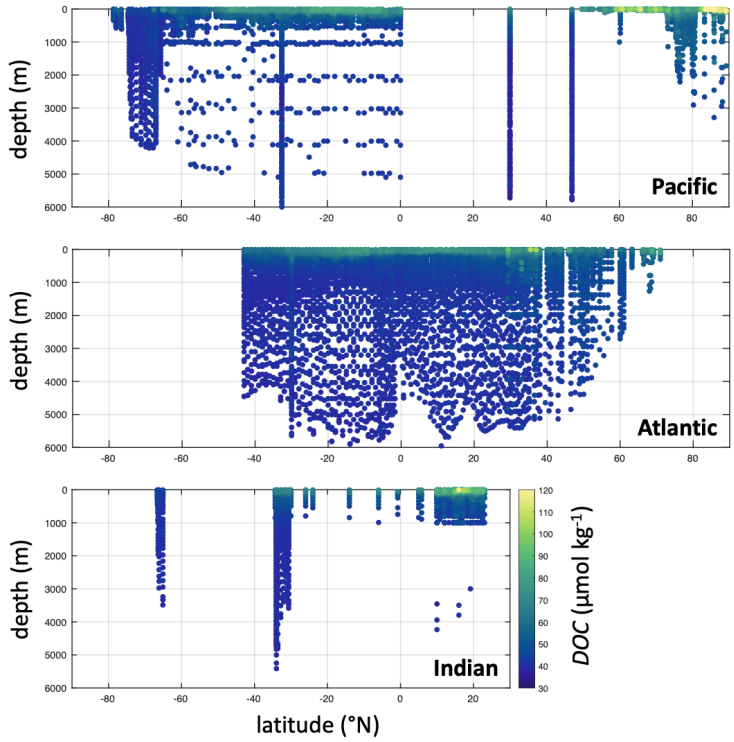

Figure 4. Dissolved organic carbon concentration (*DOC*) depth profiles in the Pacific (all data between 160°W and 180°W), Atlantic (all data between 20°W and 30°W) and Indian (all data between 60°E and 80°E) Oceans.

2.7. *POC* consumption rates

POC flux measurements from the sediment-trap dataset of Mouw et al. (2016) were used. In each region, *POC* fluxes were sorted according to increasing depth and interpolated in the vertical using a cubic smoothing spline from the MATLAB curve-fitting toolbox (smoothing parameter $p = 1\times10^{-6}$, De Boor, 1978). This allows us to turn discrete values into continuous estimates over depth and obtain regionally harmonized depth profiles of *POC* settling fluxes. These fluxes were used to compute *POC* consumption rates in three predefined depth zones, defined in *Methods section 2.4.*: (i) the *twilight zone*, (ii) the *midnight zone*, and (iii) the *abyss*. In each zone, the difference between the deepest and the shallowest flux is

divided by the zone height, and the resulting consumption rate is then converted into μmol kg^{-1} a^{-1}. A positive value indicates *POC* consumption, and a negative value indicates *POC* production.

2.8. Sediment oxygen uptake

To assess the contribution of seafloor processes to the *OUR* throughout the water column, we compared the horizontally integrated *OUR* profiles derived in this study, termed the 'total' *OUR*, with horizontally integrated 'seafloor' *OUR* estimates. We computed seafloor *OUR* using the multicomponent linear regression model of Eq. 5.1 in the work of Jørgensen et al. (2022), which predicts total oxygen uptake rate as a function of seafloor depth and euphotic net primary production. This regression model was established using 798 *in situ* measurements of oxygen utilization rate at the seafloor, distributed throughout the world oceans (Jørgensen et al., 2022). As in the work of Jørgensen et al. (2022), we used the satellite-based monthly climatology of net primary production available from Oregon State University averaged over a 10-year period (1998-2007). Bathymetry data are from the GEBCO Compilation Group (2022).

3. Results

Between the top and bottom of the twilight zone, i.e., within the 500 meters beneath the base of the euphotic layer, *OUR* decreases by about one order of magnitude (Fig. 5, 6). In the twilight zone, the *OUR* attenuation with depth can be well-described with a power law similar to a "Martin curve" (Martin et al., 1987), i.e., $OUR = C \times (z/E_z)^{-b}$, where C is a fitted amplitude, z is the depth below the euphotic zone (depth E_z), and b is a fitted attenuation parameter with a value of 1.21 when data from all regions are merged (Fig. 6). The attenuation parameter describes how steeply *OUR* decreases with depth, and is in practice dependent on the balance between organic matter reactivity, settling velocity and seawater viscosity (Sarmiento & Gruber, 2006; Dinauer et al., 2022). The attenuation parameter varies regionally, and according to our results, is higher (steeper *OUR* decrease) in subtropical regions, and lower (smoother *OUR* decrease) in low- and high-latitudes region (Fig. S3). This is consistent with a more efficient *POC* transfer to the deep ocean (low b) in productive, high-latitudes regions than in low-productivity regions such as subtropical gyres, where more *POC* is consumed near-surface and less reaches the deep ocean (high b). This interpretation agrees with other studies (Berelson, 2001; Sarmiento & Gruber, 2006; Weber et al., 2016; Maerz et al., 2020; Dinauer et al., 2022). Averaged over the entire twilight zone, *OUR* is highest in subpolar regions (subpolar North Pacific and Atlantic, Southern Ocean; 3.6-4.8 μmol kg^{-1} a^{-1}) and lowest in equatorial regions (equatorial Pacific and Atlantic; 2.3-2.6 μmol kg^{-1} a^{-1}), see Fig. 7 and Table S1. We note, however, that a power law does not match well *OUR* in the midnight zone and that the power-law fit was not performed in a log-space, which influences the weighting.

Within the midnight zone, i.e., from the bottom of the twilight zone to 3 km below sea level, *OUR* shows a smoother decrease with depth (Fig. 5) and, except for the Southern Ocean, is less variable regionally than in the twilight zone (Table S1). In the midnight zone, data density is very low in the Southern Ocean, where the only available *OUR* estimates are in or near the upper kilometer of the water column (Fig. 5). This explains the relatively high *OUR* estimate in that region (1.4 ± 0.1 μmol kg^{-1} a^{-1}), when compared to other regions where more data is available deeper, see Fig. 7). In the abyss (below 3 km depth), *OUR* does not show a particular trend with depth (Fig. 5). Among all regions (Fig. 7), abyssal *OUR* lies in a narrow

range, with the lowest values in the Pacific gyres and in the subtropical North Atlantic (Table S1).

DOC consumption-rate profiles (Fig. 8) show patterns similar to those of the *OUR* profiles, decreasing by at least an order of magnitude in the twilight zone. Note that *DOC* is not only consumed in the deep sea, but also produced by solubilization and sloppy feeding, and released from sediments and hydrothermal vents (Hansell and Carlson, 2004; Luther, 2021; Yamashita et al., 2023). Consumption rates are *net* rates and thus occasionally appear negative (net *DOC* source). Negative *DOC* consumption rates are not shown in Fig. 8 for clarity but are included in the budgets shown in Fig. 9, S4 and Table S1.

POC fluxes show an expected decrease with depth in all regions (Fig. S4), but the variability is very large, which hinders interpretation of the data. When merging *POC* fluxes from all regions, the POC flux attenuation with depth is well described by a power law, with an attenuation parameter $b = 0.53$ (Fig. 6). This value is lower than for *OUR*, and lower than from other estimates from the literature (Middelburg, 2019). *POC* fluxes may be underestimated near the surface, due to the presence of "swimmers" in sediment traps (Buesseler et al., 2007) which actively enter the traps and feed on the collected organic material, leading to an underestimation of the flux attenuation. *POC* consumption rates are lower (Fig. 7) in the gyres than in highly productive regions such as the North Atlantic, the Southern Ocean or the low latitudes (Dunne et al., 2007).

DOC consumption rates are generally lower than *POC* consumption rates, but there are important regional exceptions where *DOC* consumption is on par (Southern Ocean) or larger (North Atlantic midnight zone and 5 abyssal regions; Figs. 7, S5, Table S1). In the twilight zone, for 5 regions out of 10 (Fig. 9), the sum of *DOC* and *POC* consumption rates (expressed in moles of C per kg per year) lies within the uncertainty bounds of *OUR* (expressed in terms of moles of O_2 per kg per year). In the midnight zone as well as in the abyss, the sum of *DOC* and *POC* consumption rates is significantly lower than *OUR* in all regions (Fig. 9). This suggests the presence of another sink of O_2 in these two depth zones, likely O_2 utilization at the seafloor (see Discussion). In the abyss, in 5 regions out of 10, the *DOC* consumption rates are significantly higher than the *POC* ones (Fig. 9, Table S1), meaning that *DOC* is the main substrate for abyssal respiration.

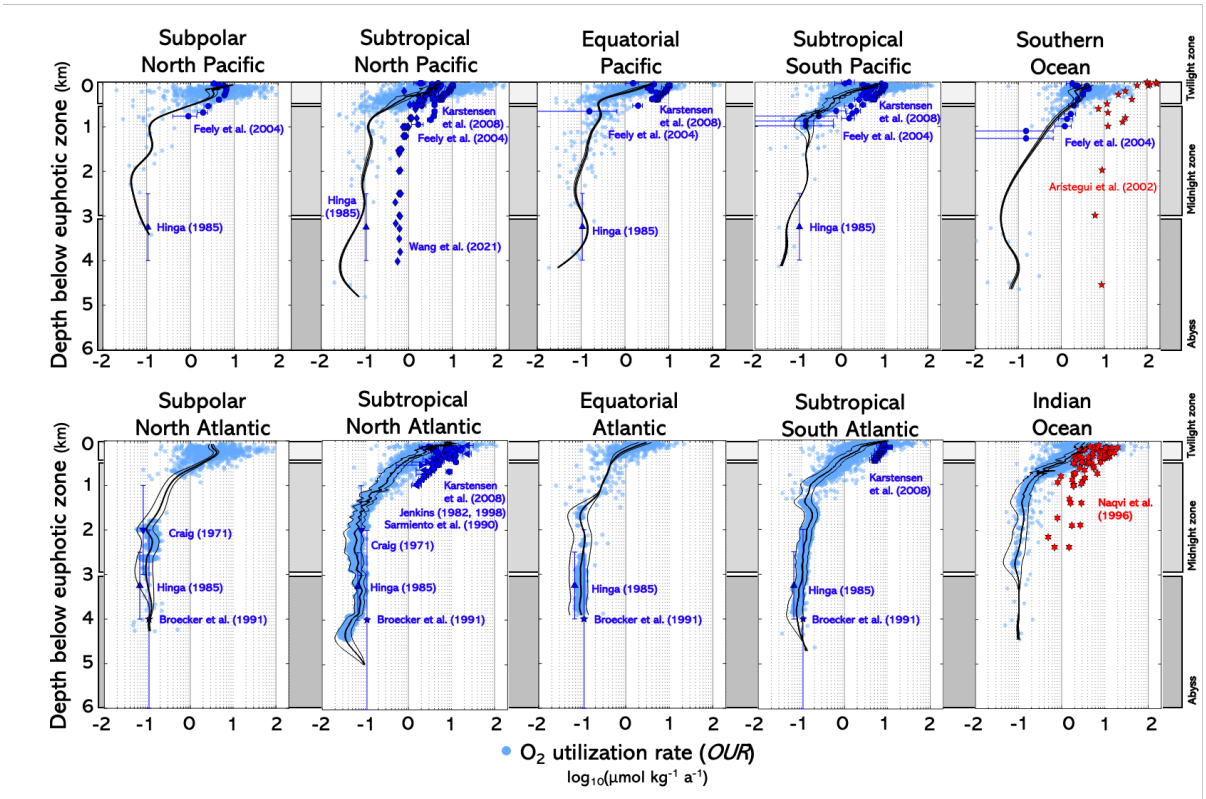

Figure 5. O_2 utilization rate (*OUR*) as a function of the water depth below E_z. Individual respiration rates resulting from 5000 Monte Carlo simulations are plotted as blue circles. The thick black lines are cubic smoothing splines used to interpolate discrete rates over depth and obtain regionally harmonized depth profiles. The thin black lines are cubic smoothing splines computed from individual rates plus or minus their associated uncertainty. Dark blue markers are *OUR* estimates from previous studies. Dark red markers are estimates of the oxygen consumption rate derived from electron transport systems (ETS) activity measurements, taken from two previous studies. The data and brief descriptions of the previous studies' methods are archived on Zenodo (https://doi.org/10.5281/zenodo.7632177).

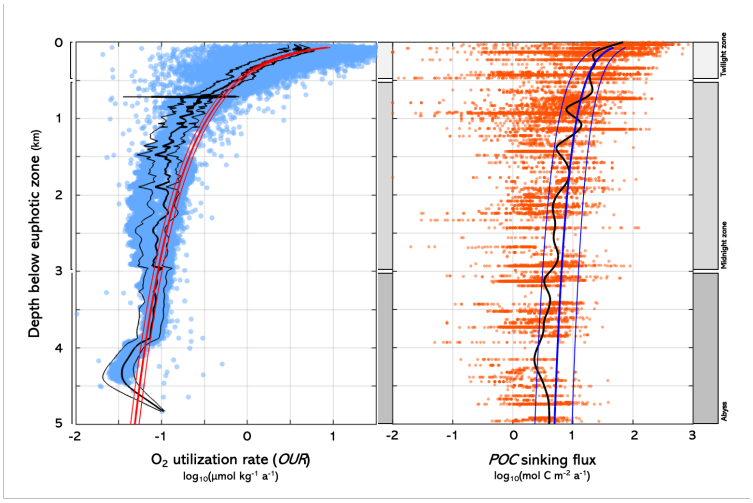

Figure 6. O_2 utilization rate (*OUR*) and *POC* sinking fluxes as a function of the water depth below E_z. Individual respiration rates resulting from 5000 Monte Carlo simulations are plotted as blue circles and individual sediment-trap measurements are plotted as orange circles. The thick black lines are cubic smoothing splines used to interpolate data over depth and obtain regionally harmonized depth profiles. The thin black lines are cubic smoothing splines computed from individual rates plus or minus their associated uncertainty. Solid thin red (for *OUR*) and blue (for *POC* fluxes) lines are fitted power laws, $OUR = 9.2\ (\pm 0.5) \times (z/E_z)^{-1.21\ (\pm 0.02)}$ and *POC* finking flux $= 49\ (\pm 14) \times (z/E_z)^{-0.53\ (\pm 0.06)}$, respectively, and surrounding thin lines represent the uncertainty range.

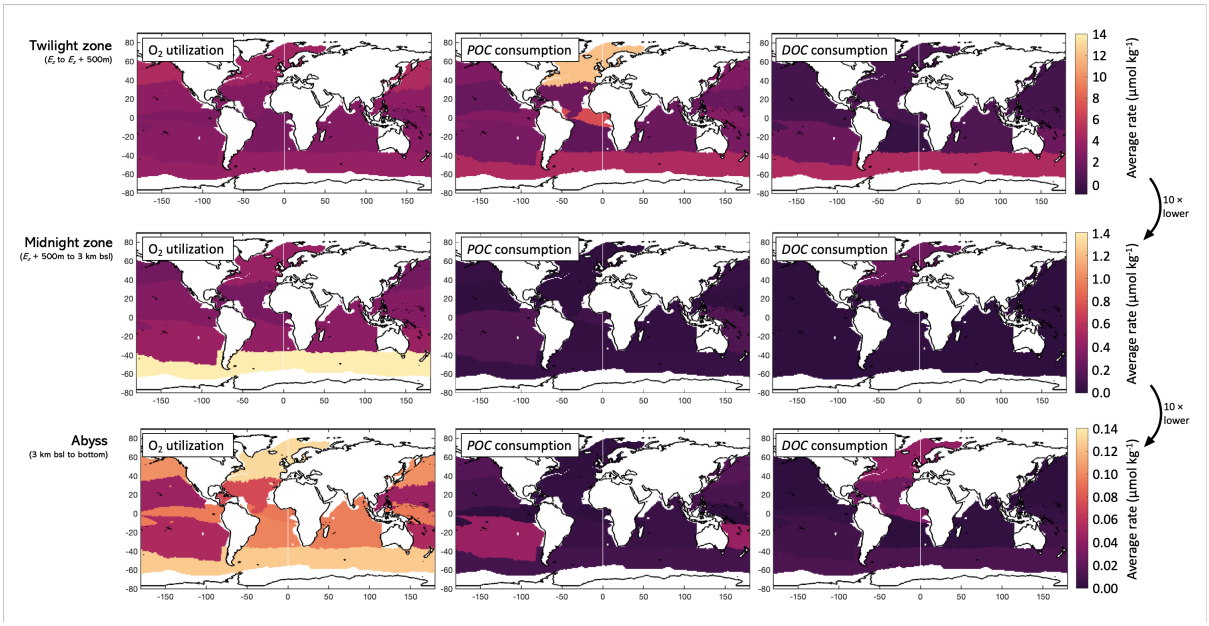

Figure 7. Regionally-averaged rates in all regions and in three depth zones, the twilight zone (top row, E_z to E_z + 500 m), the midnight zone (middle row, E_z + 500 m to 3 km below sea level) and the abyss (bottom row, 3 km below sea level to the bottom). Note the bounds of the color axes are the same for each row, each being an order of magnitude smaller than those of the row above.

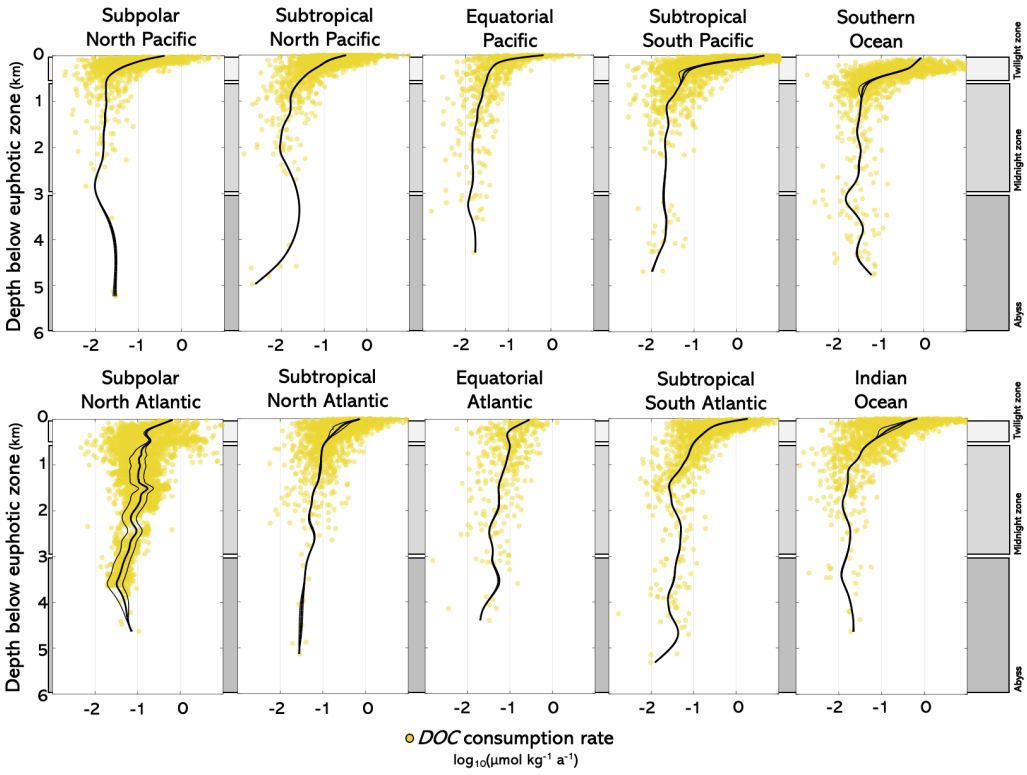

Figure 8. *DOC* consumption rate as a function of the water depth below E_z. Individual consumption rates resulting from 5000 Monte Carlo simulations are plotted as yellow circles. The thick black lines are cubic smoothing splines used to interpolate discrete rates over depth and obtain regionally harmonized depth profiles. The thin black lines are cubic smoothing splines computed from individual rates plus or minus their associated uncertainty.

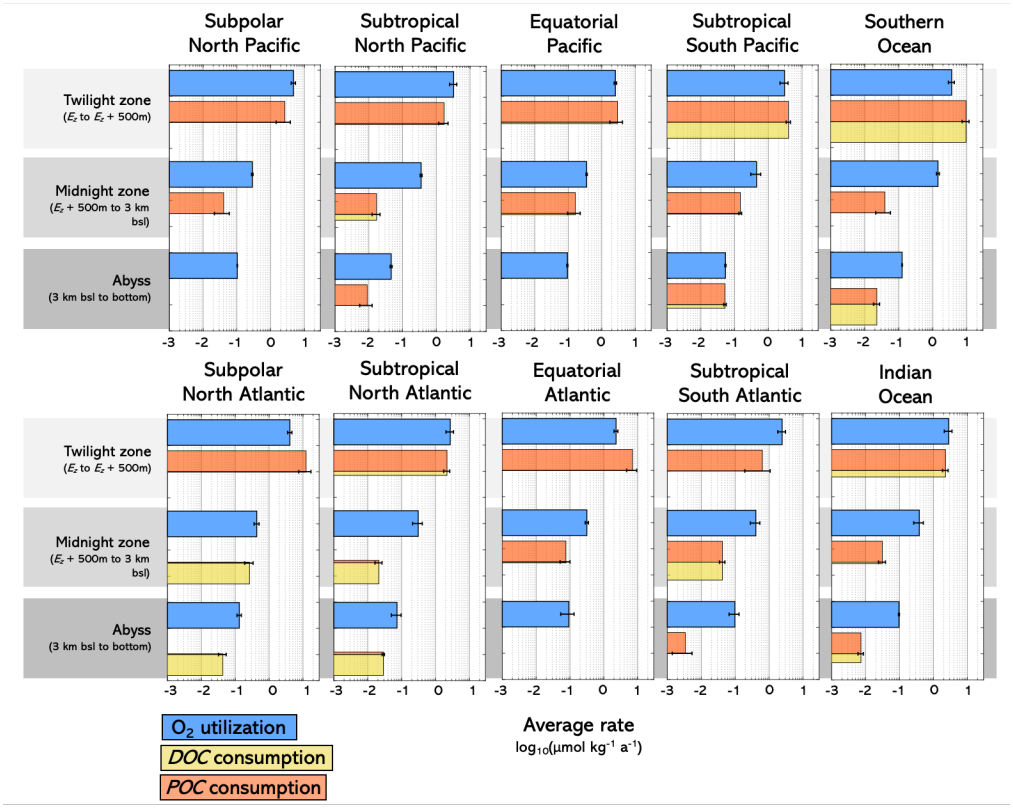

Figure 9. Regionally-averaged rates in three depth zones, the twilight zone (E_z to E_z + 500 m), the midnight zone (E_z + 500 m to 3 km depth) and the abyss (3 km depth to the bottom). All rates are expressed in µmol kg^{-1} a^{-1}. The horizontal length of both the orange and yellow bars represents the sum of the *DOC* and *POC* consumption rates. The vertical width of the orange and yellow bars represents the relative contribution of either *POC* or *DOC* consumption, respectively, to the total *OC* consumption rates. Orange and yellow bars are plotted in all regions and depth zones, but are sometimes too small to be visible. Note that the same data are also reported in Fig. 7, Table S1 and Fig. S5.

4. Discussion

4.1. Comparison with other *OUR* estimates

Most published *OUR* estimates have been derived from measurements of oxygen concentration decrease with incubation time or seawater age (Craig, 1971; Jenkins, 1982; Hinga, 1985; Sarmiento et al., 1990; Jenkins, 1998; Feely et al., 2004; Karstensen et al., 2008; Wang et al., 2021). Other estimates, however, have been obtained indirectly, by measuring the activity of electron transport systems (ETS), a chain of enzymes that passes electrons to electron acceptors such as oxygen and thus providing energy to the living cells of respiring organisms (Cammen et al., 1990). Measuring ETS activity provides the value of the oxygen consumption rate that would occur if all enzymes functioned at maximum activity (Naqvi et al., 1996; Arístegui et al., 2005). In this section, we compare oxygen consumption rates as obtained by these different approaches with ours, both regionally and globally.

Using *AOU* and seawater age estimates, Feely et al. (2004) and Karstensen et al. (2008) computed *OUR* in the Atlantic and Pacific, respectively, ranging between 2 and 10 µmol kg^{-1} a^{-1} in the twilight zone, and decreasing to ~0.1 µmol kg^{-1} a^{-1} at 1000-m depth (Fig. 5). Jenkins (1982) reported *OUR* of 4-20 µmol kg^{-1} a^{-1} in the twilight zone and 1-4 µmol kg^{-1} a^{-1} in the midnight zone of the North Pacific. Wang et al. (2021) reported *OUR* of 8.4 µmol kg^{-1} a^{-1} at a depth of 100-m depth in the South China Sea and 0.66 µmol kg^{-1} a^{-1} at 1500-m depth and also

noted a positive correlation between temperature and respiration rate. Using a tritium box model, Sarmiento et al. (1990) estimated *OUR* between 2.8 and 5.4 μmol kg^{-1} a^{-1} in the top 700 m of the North Atlantic subtropical gyre. Our twilight-zone *OUR* estimates broadly encompass these and other previously reported values. Below 2500-m depth, Hinga (1985) reported *OUR* of 0.11 μmol kg^{-1} a^{-1} in the Pacific and 0.07 μmol kg^{-1} a^{-1} in the Atlantic. Broecker et al. (1991), using O_2 and ^{14}C, report respiration rates of about 0.1 μmol kg^{-1} a^{-1} in the deep Atlantic, in waters below 2000 m. These midnight and abyssal estimates are also quantitatively consistent with our results.

In the Indian and Southern oceans, there are no directly comparable data, but there are oxygen-consumption rate estimates based on respiratory ETS activity. In the Indian Ocean, between 200 and 2400-m depth, assuming Redfieldian organic-matter stoichiometry, Naqvi et al. (1996) report ETS-based estimates of ~3.0 μmol O_2 kg^{-1} a^{-1} for the Arabian Sea and ~1.3 μmol O_2 kg^{-1} a^{-1} for the Bay of Bengal (Fig. 5). For the Indian sector of the Southern Ocean, between 200 and 1000-m depth, the ETS-based results of Arístegui et al. (2002) translate to ~2.4 μmol O_2 kg^{-1} a^{-1} (assuming Redfieldian stoichiometry). Respiration rates inferred from ETS activity thus match our estimates in terms of magnitude in the twilight zone, but strongly overestimates *OUR* at deeper depths. In fact, ETS-based estimates are likely overestimating true respiration rates because, when extrapolated globally, they provide a very high global respiration rate of 33 Gt C a^{-1} (Arístegui et al., 2003).

Integrating O_2 respiration rates over space, we find a global respiration rate below the euphotic zone of 907±165 Tmol O_2 a^{-1}. Assuming an effective molar ratio of O_2 to C of 1.3 during aerobic respiration (Redfield, 1958), this is equivalent to a respiration rate of 8.37±1.52 Gt C a^{-1}. To the degree that aphotic organic matter sources can be neglected, note this is also an estimate for what has been called "export production", a key metric of the ocean's biological pump (Primeau et al., 2013) that accounts for both *POC* and *DOC* export (*POC* and *DOC* contributions discussed in the next subsection). For comparison, integrated over the entire ocean, Antia et al. (2001)'s *POC* flux at the base of the euphotic layer is about 10 Gt C a^{-1} (Arístegui et al., 2005), and other estimates broadly range between 5 and 12 Gt C a^{-1} (Andersson, 2004; Laws et al., 2000; Dunne et al., 2007; Henson et al., 2011; Siegel et al., 2014; DeVries & Weber, 2017; Middelburg, 2019). Note, however, that the *OUR* estimates presented here in theory account for both the respiration in the water column as well as for oxygen utilization at the seafloor (see Section 4.3), and that we do not include high-latitude systems while some of the other estimates do.

As explained in the *methods section 2.5*, to test the robustness of our methods, we have duplicated our *OUR* analysis replacing *TOU* by [O_2]. The *OUR* profiles based on [O_2] (Fig. S6) have depth patterns similar to those obtained using *TOU* (Fig. 5), i.e., a steep decrease in the top kilometre of about two orders of magnitude, and a much smoother decrease below. We note that in the shallowest parts of the depth profiles, [O_2]-based *OUR* seems to consistently overestimate *TOU*-based *OUR*. However, the inferred global oxygen utilization rates based on [O_2] (1066±248 Tmol a^{-1}) and based on *TOU* (907±165 Tmol a^{-1}) are statistically indistinguishable. Overall, this suggests that the choice of respiration proxy has minor influence on the results presented in this study, and that differences in mixing representation across various proxies should not affect our conclusions. Based on a high-complexity Earth system model, Guo et al. (*under review*) have shown that in the tropical South Atlantic, between 1860 and 2100, temporal changes in water mixing patterns may affect measured oxygen utilization and water-age estimates in different ways, which leads to divergence between OUR and the true respiration rate. Even though our tracer CFC and ^{14}C-based ages

480 take mixing into account to some extent, it is worth emphasizing that OUR is simply a proxy
481 for true respiration, and that a difference between both may be present, due to unaccounted
482 small-scale transport processes.
483

484 **4.2. Organic matter cycling**

485 Our *POC* consumption rates agree with those computed from *POC* retrieved in
486 sediment traps in the Pacific (Martin et al., 1987), which range from 0.01 to 0.05 μmol $kg^{-1}a^{-1}$.
487 Reanalyzing data from Menzel & Ryther (1968), Craig (1971) reported a *DOC* consumption
488 rate of 0.029 μmol kg^{-1} a^{-1} for the NADW, which is within the range of our *DOC* consumption
489 rates from the North Atlantic midnight zone (0.020-0.056 μmol kg^{-1} a^{-1}).
490

491 Globally, we find that 511±179 Tmol of *POC* and 216±35 Tmol of *DOC* (hence
492 727±182 Tmol of total OC) are consumed in the dark water column every year. That is, *DOC*
493 consumption accounts for 30±12, 20±9 and 34±15% of organic carbon consumption (and hence
494 export production) in the twilight, midnight and abyssal zones, respectively. This DOC
495 contribution is somewhat lower than that of Pan et al. (2014) who report that up to half of *AOU*
496 was driven by *DOC* consumption in the North Atlantic, and contrasts with Jahnke (1996) who
497 reported that there is no need for *DOC* to account for deep water respiration rates. Note that
498 the presence of non-sinking *POC*, not accounted for here as it is not caught in sediment traps,
499 complicates this interpretation (Baltar et al., 2010). If deep-ocean, water-column respiration is
500 dominated by sinking particles, then this respiration is subject to sporadic, high productivity
501 events and to seasonality (Anderson & Sarmiento, 1994). In addition, the importance of *DOC*
502 as a substrate for deep-ocean, water-column respiration makes circulation changes (e.g.,
503 weakening overturning circulation; Caesar et al., 2018) an important player for deep oxygen
504 cycling, because circulation affects where and how fast *DOC* can be delivered.
505

506 *DOC* with apparent ages of 6000 years was reported in the abyssal (5710 m) subtropical
507 North Pacific (Williams et al., 1988). In abyssal regions, *DOC* concentrations show very little
508 variation around a value of about 35 μmol kg^{-1} (Fig. 4), while the mean age of seawater
509 increases (Fig. 2) along the path of water masses. Altogether, this suggests intense *DOC*
510 recycling by abyssal microbial communities. Our computed *DOC* consumption rates are in
511 general very small and highly variable across regions and depth ranges (Table S1), some being
512 negative, meaning that *DOC* is being regenerated faster than it is consumed. In the abyssal
513 realm, we note a clear negative correlation of *DOC* consumption rates with seawater mean age
514 (R^2 = 0.74, p = 0.001; Fig. 10). While abyssal regions where waters are young (e.g., North
515 Atlantic) show relatively fast *DOC* consumption, abyssal regions where waters are old (e.g.
516 North Pacific) show net *DOC* production. This confirms that dissolved organic matter lability
517 decreases with age (Middelburg, 1989) as its composition shifts from carbohydrates and
518 protein-like compounds toward more refractory lipophilic forms (Benner et al., 1992; Ogawa
519 et al., 2001; Loh et al., 2004) and supports intense abyssal *DOC* recycling. Abyssal *DOC*
520 degradation rates generally decrease with seawater age, supporting the concept of emergent,
521 rather than intrinsic, recalcitrance of dissolved organic matter proposed by Dittmar et al.
522 (2021). According to this concept, individual organic constituents are continuously reworked,
523 within complex ecological networks encompassing all trophic levels, including phytoplankton,
524 bacteria, viruses and grazers. Note that Follett et al. (2014) reported a decreasing trend in the
525 *DOC* concentration with seawater age along the path of the deep branch of the conveyor belt,
526 in which *DOC* loss is not a gradual monotonic process, but shows some variability, for instance,
527 regions with strong *POC* surface export show local abyssal *DOC* concentrations. The low

spatial resolution of our analysis prevents us from seeing such spatial variability in abyssal *DOC* consumption rates.

The deep-ocean intense *DOC* cycling reported here is mostly fueled by *DOC* subducted from the surface and originating from *POC* degradation, which should altogether represent a 1 Gt *DOC* a^{-1} source to the deep ocean (Follett et al., 2014). However, there are other *DOC* sources that complicate the interpretation of our results. Net *DOC* production in the deeper part of the water column may originate from marine sediments, which represent the main sites of organic-matter consumption and burial in the ocean (Burdige & Komada, 2015; Lønborg et al., 2020), hosting microbes in densities up to 1000 times higher than in the upper water column (e.g., Hewson et al., 2001). As a result, *DOC* concentrations in sediments are often an order of magnitude higher than in the water column (Burdige & Gardner, 1998). Thus, marine sediments act as a major *DOC* source, releasing 0.35 Gt of *DOC* a^{-1}, which is comparable to the *DOC* input from rivers (Burdige & Komada, 2015). Moreover, Luther (2021) and Yamashita et al. (2023) recently reported refractory *DOC* release from hydrothermal vents. For these reasons, the *DOC* consumption rates presented here can be interpreted as a lower bound on the true gross *DOC* consumption rate occurring in the water column.

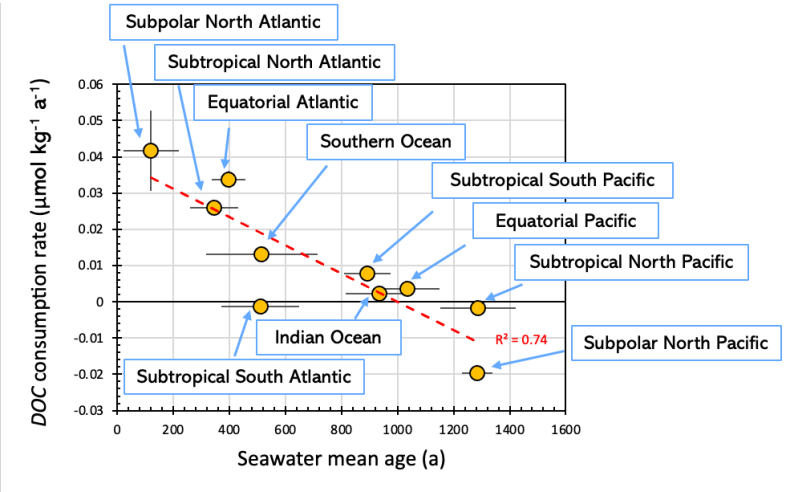

Figure 10. Regionally averaged abyssal *DOC* consumption rates as a function of regionally averaged abyssal seawater ages. Error bars represent the uncertainties associated with either *DOC* consumption rates or seawater mean age as well as the regional variability.

4.3. Seafloor respiration signal

While the *POC* consumption rates presented here should not be influenced by seafloor processes, *OUR* and *DOC* consumption-rate estimates for a given isopycnal could be affected by benthic processes if the isopycnal water mass incrops on the seafloor. In theory, seafloor respiration is reflected throughout the water column, as the oxygen being respired in the dark ocean is supplied by bottom waters. In practice, since our reconstructed *OUR* vertical profiles do not extend all the way to the ocean bottom, deeper isopycnals strongly affected by this benthic respiration may not be included in our analysis. Note that this considers ocean mixing occurring primarily along isopycnals, which is an incomplete picture since it neglects diapycnal mixing and topography-driven mixing, which may carry the oxygen deficit or *DOC* released from seafloor processes into the overlying water column.

Seafloor and total *OUR* were horizontally integrated, to obtain the vertical profiles plotted in Fig. 11. In all regions, total *OUR* declines systematically with water depth, while

seafloor oxygen consumption initially declines with water depth, but increases again because of ocean hypsometry (large parts of the ocean have depths between 3 to 6 km). Consequently, in all regions, except in the north subpolar Pacific, seafloor *OUR* can explain total *OUR* at depths below 2 to 4 km, depending on ocean basin. This pattern is very similar to that reported in Emerson and Hedges (2012) and Middelburg (2019) based on different approaches and datasets. Based on sediment oxygen consumption data, Middelburg (2019) concluded that sediment respiration dominates below 3 km depth because of hypsometry, which amplifies the seafloor respiration signal occurring for these depths. Thus, we conclude that it is very likely that the observed deep-water oxygen concentration changes reflect, to a large extent, respiration at the seafloor. That in all regions, *OUR* in the midnight zone and in the abyss always significantly exceeds the sum of *POC* and *DOC* consumption rates (Fig. 9) confirms that respiration signals from the seafloor can likely be felt even quite high in the water column.

Jahnke (1996) reported 120 Tmol O_2 a^{-1} for respiration below 1000-m depth, including 86 Tmol O_2 a^{-1} (72%) for *POC* respiration at the seafloor. According to another analysis, seafloor respiration accounts for 28% of respired O_2 below 1000-m depth (Andersson, 2004). Here, using the approach of Jørgensen et al. (2022), we find that over the 10 regions used in our study (Fig. 3a), seafloor *OUR* integrates to 74±8 Tmol a^{-1}. Overall, even though seafloor processes likely dominate total oxygen utilization in the abyss, for the entire water column, only (8.2±0.4)% (74/907) of oxygen utilization occurs at the seafloor, probably primarily through the benthic respiration of organic matter. While we interpret non-water-column oxygen utilization in the deep ocean as originating from benthic respiration, exceptions could occur near hydrothermal systems that act as a source of old and refractory *DOC* (Luther, 2021; Yamashita et al., 2023). Hydrothermal plumes also act as a source of powerful oxidants that can oxidize even the most refractory deep-ocean *POC* and *DOC* (Shaw et al., 2021). If that effect is important at a global scale, the fraction of the *POC* and *DOC* consumption rates that is due to aerobic respiration is overestimated in our interpretation.

Finally, important seafloor O_2 utilization that influences oxygen cycling throughout the water-column has implications for our understanding of the marine carbon cycle's response to environmental changes. Changes in the *POC* delivery to the seafloor in the Anthropocene could originate from multiple factors, e.g., migrations, overfishing, eutrophication/fertilization, and ocean afforestation. These perturbations would likely affect early diagenesis and benthic oxygen utilization, even at the deep seafloor. In turn, changes in benthic oxygen fluxes would be propagated throughout the water column, affecting microbial and larger heterotrophic communities populating the dark ocean.

4.4. Integrated budget

We find a global respiration rate below the euphotic zone of 907±165 Tmol O_2 a^{-1}. Subtracting from this rate the oxygen utilization rate at the seafloor (74±8 Tmol O_2 a^{-1}) gives an aphotic water-column respiration rate of 833±165 Tmol O_2 a^{-1}. Assuming a Redfield O_2:C ratio for aerobic respiration (1.3), this translates to a respiration rate of 640±127 Tmol C a^{-1}. This respiration rate is statistically indistinguishable from the global water-column organic carbon consumption rate of 727±182 Tmol C a^{-1} (511±179 Tmol of *POC* and 216±35 Tmol of *DOC*) that we derived in this study, using independent datasets. At the global scale, *OUR*, the *DOC* and *POC* consumption rates, and the seafloor oxygen utilization rates are all consistent with each other and coherent with a globally uniform O_2:C of 1.3. Even though many aspects of the marine carbon and oxygen cycles still deserve further attention, such as identifying *DOC* sources and sinks, or the fate of sedimentary organic carbon, we are now, thanks to decades of

high-quality oceanographic measurements, able to present an internally consistent integrated *OC* and O_2 budget that can be used to calibrate models and assure their validity.

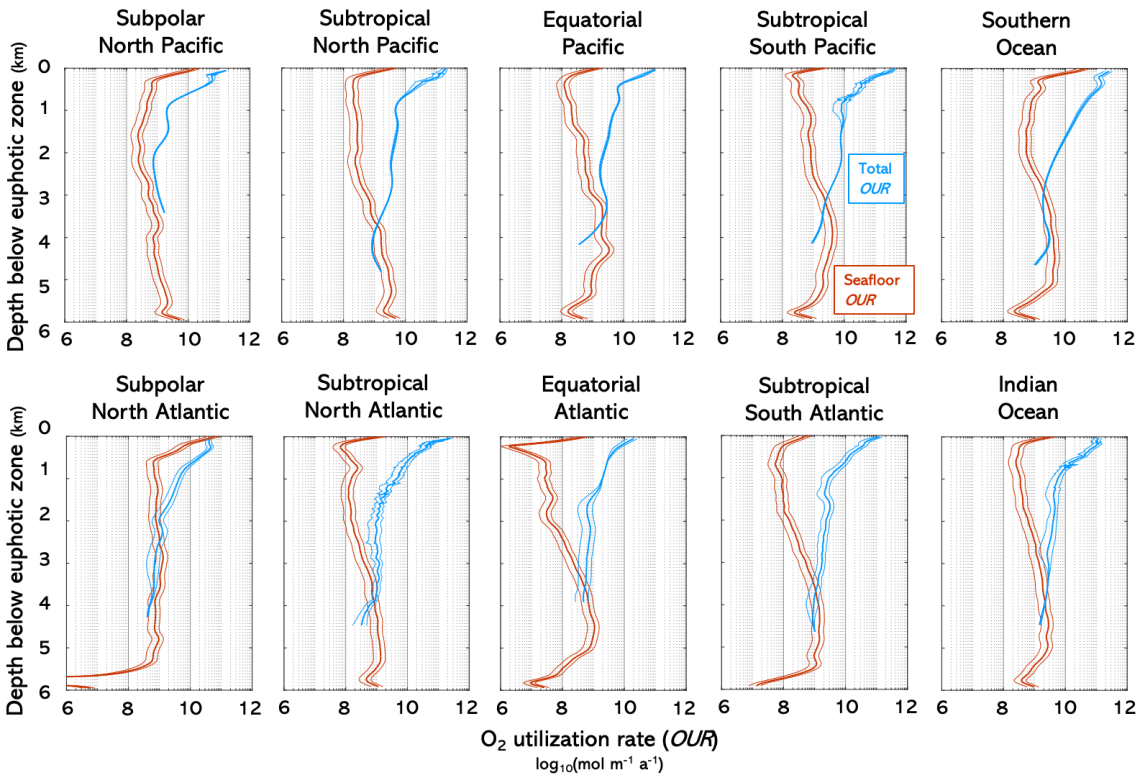

Figure 11. Regionally horizontally integrated averaged O_2 utilization rate (*OUR*) in the water-column per unit depth and at the seafloor as a function of depth below the euphotic zone. Water-column *OUR* corresponds to *TOU* changes with mean age along isopycnals, i.e., the profiles derived in this study and shown in Fig. 5. Seafloor *OUR* are computed from the methods presented in Jørgensen et al. (2022), using euphotic net primary production estimates from Oregon State University and GEBCO bathymetry.

5. Conclusion

We derived depth-profiles of oxygen utilization rate (*OUR*) and *DOC* consumption rate in 10 major biogeographical regions of the ocean. In the kilometer below the euphotic layer, *OUR* decreases by about two orders of magnitude, with the decrease being steeper in low-productivity regions such as subtropical gyres, where more *POC* is consumed near-surface and less reaches the deep ocean, than in low- and high-latitude regions. Seafloor oxygen consumption accounts for nearly all the *OUR* of the abyssal water column. *DOC* consumption rate also decreases by about two orders of magnitude in the kilometer below the euphotic zone. In the abyss, *DOC* consumption rate decreases with increasing seawater age. This is in line with the concept of emergent, rather than intrinsic, recalcitrance of dissolved organic matter. In the water-column, about a third of the respired organic carbon is *DOC* originating from subducted surface water, *POC* degradation, or seafloor and hydrothermal sources.

While our respiration rate profiles and integrated budget are improvements over earlier estimates, there remain considerable uncertainties. We anticipate that further development in the representation of ocean mixing in models will allow for more accurate products of seawater age and oxygen utilization, which may reduce the uncertainty of the respiration rates presented here. Our study also presents results across a set of biogeographical regions which could have

been defined differently and exclude high-latitude and coastal areas that should be the focus of future efforts.

We find a global *OUR* below the euphotic zone of 907±165 Tmol O_2 a^{-1}, 8% of which occurs at the seafloor. Using an Redfield O_2:C of 1.3, this translates to a respiration rate of 640±127 Tmol C a^{-1}, which is consistent with the sum of the *DOC* and *POC* consumption rates estimated in this study, i.e., 727±182 Tmol C a^{-1}. Our analysis shows that measurements of dissolved O_2 and *DOC*, seafloor O_2 utilization, and sediment-trap *POC* can all be reconciled in an integrated global budget.

Acknowledgements

This manuscript has benefited from discussions with many colleagues, in particular, members of the SCOR working group 161 ReMO (Respiration in Mesopelagic Ocean). We thank all of those who contributed to the creation of GLODAPv2 (Key et al., 2015; Lauvset et al., 2016; Olsen et al., 2016), the dissolved organic matter dataset (Hansell et al., 2021), the particulate flux dataset (Mouw et al., 2016), as well as the TTD age (Jeansson et al., 2021) and ^{14}C age (Gebbie & Huybers, 2012) products. This study has been conducted using E.U. Copernicus Marine Service Information. This research was supported by the Netherlands Organisation for Scientific Research (NWO-VENI grant VI.Veni.212.086 to O.S.) and the Netherlands Earth System Science Center. M. H. acknowledges funding from Australian Research Council (ARC) grant DP210101650.

Open research – availability statement

The TTD ages (Jeansson et al., 2021) are made available as GLODAPv2 affiliated data on the NOAA Ocean Carbon Data System website at https://www.ncei.noaa.gov/access/ocean-carbon-data-system/oceans/ndp_108/ndp108.html. Seawater chemistry data are available from the GLODAPv2.2016 in Key et al. (2015), Lauvset et al. (2016) and Olsen et al. (2016), sediment-trap data are available from Mouw et al. (2016), ^{14}C-derived ages are available from Gebbie & Huybers (2012), biome distributions are available from Fay and McKinley (2014), and the dissolved organic matter dataset is available from Hansell et al. (2015).

Supplementary materials

Table S1. Regionally-averaged rates in three depth zones, the twilight zone (E_z to E_z + 500 m), the midnight zone (E_z + 500 m to 3 km below sea level) and the abyss (3 km below sea level to the bottom). All rates are expressed in μmol kg^{-1} a^{-1}. *the rate could not be computed due to missing data, and was instead estimated as the average of the rates in all other regions of similar latitudes, e.g., all subtropical regions (see Fig. 3).

	Subpolar North Pacific	**Subtrop. North Pacific**	**Equat. Pacific**	**Subtrop. South Pacific**	**Subpolar North Atlantic**	**Subtrop. North Atlantic**	**Equat. Atlantic**	**Subtrop. South Atlantic**	**Indian Ocean**	**Southern Ocean**
O_2 utilization rate (*OUR*)										
Twilight zone	$4.8 \times 10^{0} \pm 0.7 \times 10^{0}$	$3.3 \times 10^{0} \pm 0.8 \times 10^{0}$	$2.6 \times 10^{0} \pm 0.2 \times 10^{0}$	$3.0 \times 10^{0} \pm 0.8 \times 10^{0}$	$4.1 \times 10^{0} \pm 0.6 \times 10^{0}$	$2.7 \times 10^{0} \pm 0.7 \times 10^{0}$	$2.3 \times 10^{0} \pm 0.3 \times 10^{0}$	$2.4 \times 10^{0} \pm 0.6 \times 10^{0}$	$2.8 \times 10^{0} \pm 0.7 \times 10^{0}$	$3.6 \times 10^{0} \pm 0.7 \times 10^{0}$
Midnight zone	$2.9 \times 10^{-1} \pm 0.1 \times 10^{-1}$	$3.5 \times 10^{-1} \pm 0.2 \times 10^{-1}$	$3.5 \times 10^{-1} \pm 0.2 \times 10^{-1}$	$4.5 \times 10^{-1} \pm 1.5 \times 10^{-1}$	$4.3 \times 10^{-1} \pm 0.7 \times 10^{-1}$	$3.1 \times 10^{-1} \pm 1.0 \times 10^{-1}$	$3.2 \times 10^{-1} \pm 0.3 \times 10^{-1}$	$4.1 \times 10^{-1} \pm 1.3 \times 10^{-1}$	$3.8 \times 10^{-1} \pm 1.2 \times 10^{-1}$	$1.4 \times 10^{0} \pm 0.1 \times 10^{0}$
Abyss	$1.0 \times 10^{-1} \pm 0.1 \times 10^{-1}$	$4.6 \times 10^{-2} \pm 0.3 \times 10^{-2}$	$9.5 \times 10^{-2} \pm 0.4 \times 10^{-2}$	$5.3 \times 10^{-2} \pm 0.2 \times 10^{-2}$	$1.3 \times 10^{-1} \pm 0.2 \times 10^{-1}$	$7.3 \times 10^{-2} \pm 2.3 \times 10^{-2}$	$9.3 \times 10^{-2} \pm 4.0 \times 10^{-2}$	$9.8 \times 10^{-2} \pm 3.2 \times 10^{-2}$	$9.6 \times 10^{-2} \pm 0.3 \times 10^{-2}$	$1.3 \times 10^{-1} \pm 0.1 \times 10^{-1}$
***POC* consumption rate**										
Twilight zone	$2.6 \times 10^{0} \pm 1.2 \times 10^{0}$	$1.6 \times 10^{0} \pm 0.5 \times 10^{0}$	$2.8 \times 10^{0} \pm 1.2 \times 10^{0}$	$2.2 \times 10^{0} \pm 0.2 \times 10^{0}$	$1.2 \times 10^{1} \pm 0.5 \times 10^{1}$	$1.8 \times 10^{0} \pm 0.4 \times 10^{0}$	$7.0 \times 10^{0} \pm 2.4 \times 10^{0}$	$1.3 \times 10^{0} \pm 0.4 \times 10^{0}$	$*1.7 \times 10^{0} \pm 0.4 \times 10^{0}$	$4.8 \times 10^{0} \pm 2.2 \times 10^{0}$
Midnight zone	$4.2 \times 10^{-2} \pm 1.9 \times 10^{-2}$	$1.3 \times 10^{-2} \pm 0.4 \times 10^{-2}$	$1.5 \times 10^{-1} \pm 0.6 \times 10^{-1}$	$1.4 \times 10^{-1} \pm 0.1 \times 10^{-1}$	$1.2 \times 10^{-2} \pm 0.5 \times 10^{-2}$	$2.2 \times 10^{-3} \pm 0.5 \times 10^{-3}$	$7.2 \times 10^{-2} \pm 2.4 \times 10^{-2}$	$2.3 \times 10^{-2} \pm 0.7 \times 10^{-2}$	$2.9 \times 10^{-2} \pm 0.7 \times 10^{-2}$	$3.9 \times 10^{-2} \pm 1.8 \times 10^{-2}$
Abyss	$1.6 \times 10^{-2} \pm 0.7 \times 10^{-2}$	$1.1 \times 10^{-2} \pm 0.4 \times 10^{-2}$	$-1.9 \times 10^{-2} \pm 0.8 \times 10^{-2}$	$4.4 \times 10^{-2} \pm 0.4 \times 10^{-2}$	$1.4 \times 10^{-3} \pm 0.5 \times 10^{-3}$	$3.0 \times 10^{-3} \pm 0.7 \times 10^{-3}$	$-5.7 \times 10^{-2} \pm 1.9 \times 10^{-2}$	$4.8 \times 10^{-3} \pm 1.5 \times 10^{-3}$	$5.1 \times 10^{-3} \pm 1.2 \times 10^{-3}$	$9.8 \times 10^{-3} \pm 4.5 \times 10^{-3}$
***DOC* consumption rate**										
Twilight zone	$3.0 \times 10^{-2} \pm 1.0 \times 10^{-2}$	$8.9 \times 10^{-2} \pm 2.3 \times 10^{-2}$	$1.7 \times 10^{-1} \pm 0.2 \times 10^{-1}$	$1.7 \times 10^{0} \pm 0.5 \times 10^{0}$	$2.6 \times 10^{-1} \pm 1.1 \times 10^{-1}$	$3.7 \times 10^{-1} \pm 0.8 \times 10^{-1}$	$3.9 \times 10^{-2} \pm 0.9 \times 10^{-2}$	$-6.3 \times 10^{-1} \pm 1.7 \times 10^{-1}$	$5.3 \times 10^{-1} \pm 0.9 \times 10^{-1}$	$4.8 \times 10^{0} \pm 0.4 \times 10^{0}$
Midnight zone	$-9.9 \times 10^{-4} \pm 8.9 \times 10^{-4}$	$3.7 \times 10^{-3} \pm 1.0 \times 10^{-3}$	$1.0 \times 10^{-2} \pm 0.1 \times 10^{-2}$	$5.0 \times 10^{-3} \pm 2.0 \times 10^{-3}$	$2.5 \times 10^{-1} \pm 0.7 \times 10^{-1}$	$1.9 \times 10^{-2} \pm 0.5 \times 10^{-2}$	$3.6 \times 10^{-3} \pm 4.4 \times 10^{-3}$	$1.9 \times 10^{-2} \pm 0.3 \times 10^{-2}$	$2.0 \times 10^{-3} \pm 1.8 \times 10^{-3}$	$-7.9 \times 10^{-5} \pm 251.2 \times 10^{-5}$
Abyss	$-2.0 \times 10^{-2} \pm 0.2 \times 10^{-2}$	$-1.8 \times 10^{-3} \pm 0.3 \times 10^{-3}$	$3.7 \times 10^{-3} \pm 0.3 \times 10^{-3}$	$7.7 \times 10^{-3} \pm 1.3 \times 10^{-3}$	$4.2 \times 10^{-2} \pm 1.1 \times 10^{-2}$	$2.6 \times 10^{-2} \pm 0.2 \times 10^{-2}$	$3.4 \times 10^{-2} \pm 0.2 \times 10^{-2}$	$-1.4 \times 10^{-3} \pm 1.3 \times 10^{-3}$	$2.2 \times 10^{-3} \pm 0.5 \times 10^{-3}$	$1.3 \times 10^{-2} \pm 0.1 \times 10^{-2}$

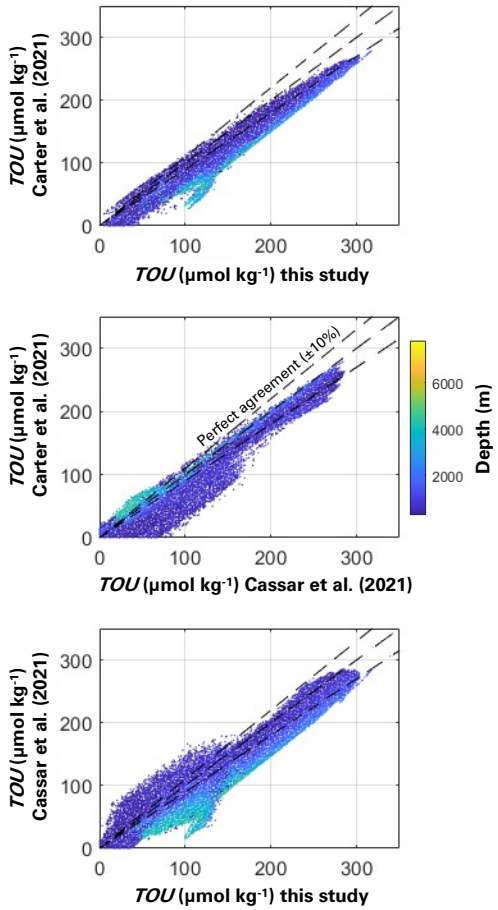

Figure S1. Comparison of *TOU* estimates from this study (GLODAPv2 and OCIM) with those from Carter et al. (2021) and Cassar et al. (2021). All data shown are deeper than 300 m and only in the defined biomes.

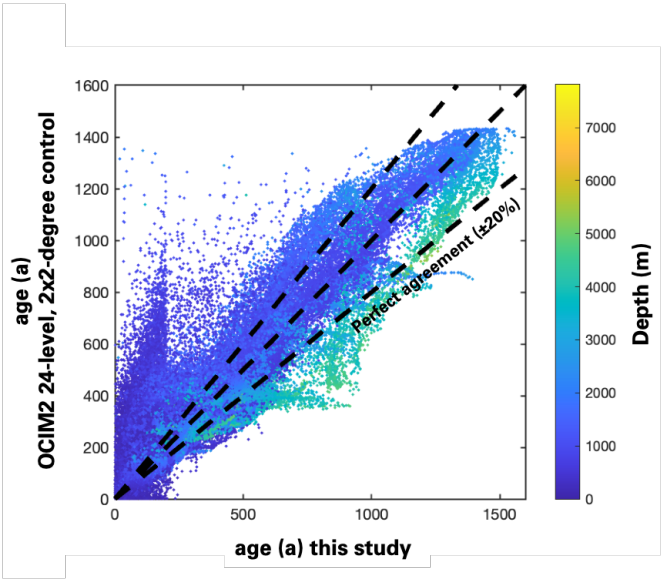

Figure S2. Comparison of seawater age estimates from this study with those from the OCIM2 model, in its 24-level, 2x2-degree control version (DeVries and Holzer, 2019).

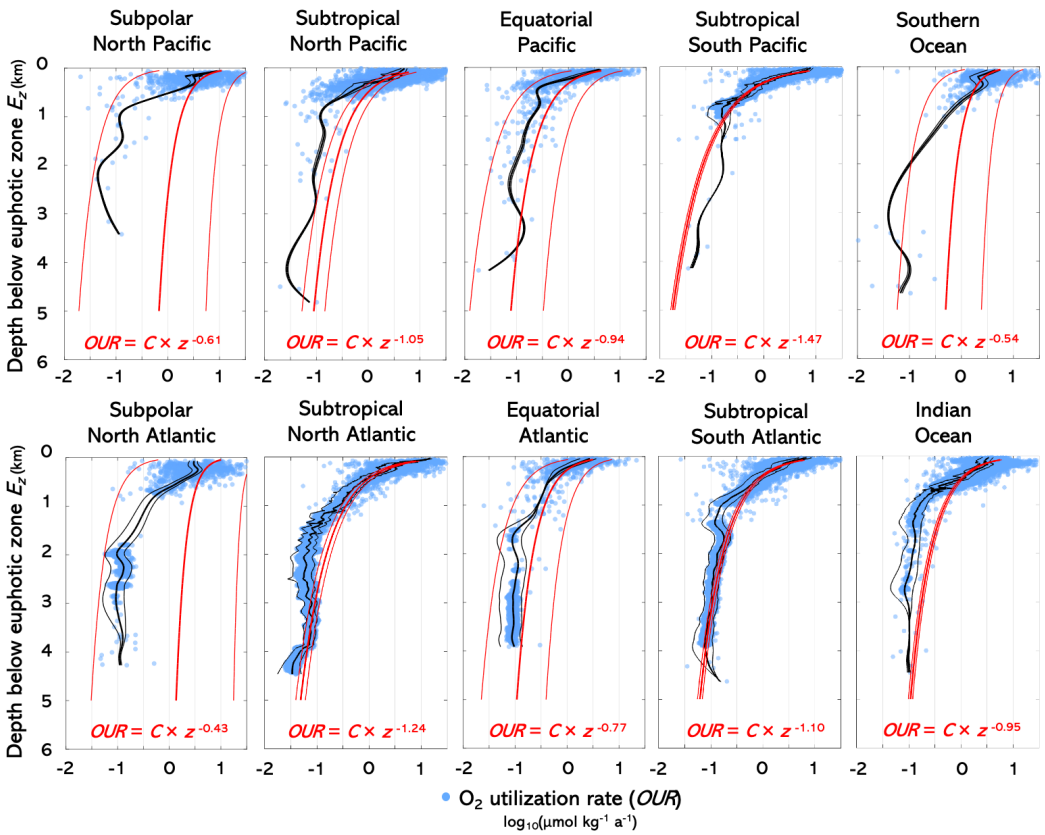

Figure S3. O_2 utilization rate (*OUR*) as a function of the water depth below E_z. Individual respiration rates resulting from 5000 Monte Carlo simulations are plotted as blue circles. The thick black lines are cubic smoothing splines used to interpolate discrete rates over depth and obtain regionally harmonized depth profiles. The surrounding thin black lines are cubic smoothing splines computed from individual rates plus or minus their associated uncertainty. Thick solid red lines are fitted power laws, whose equations are shown in the Figure, and the thin red lines represent plus or minus one uncertainty.

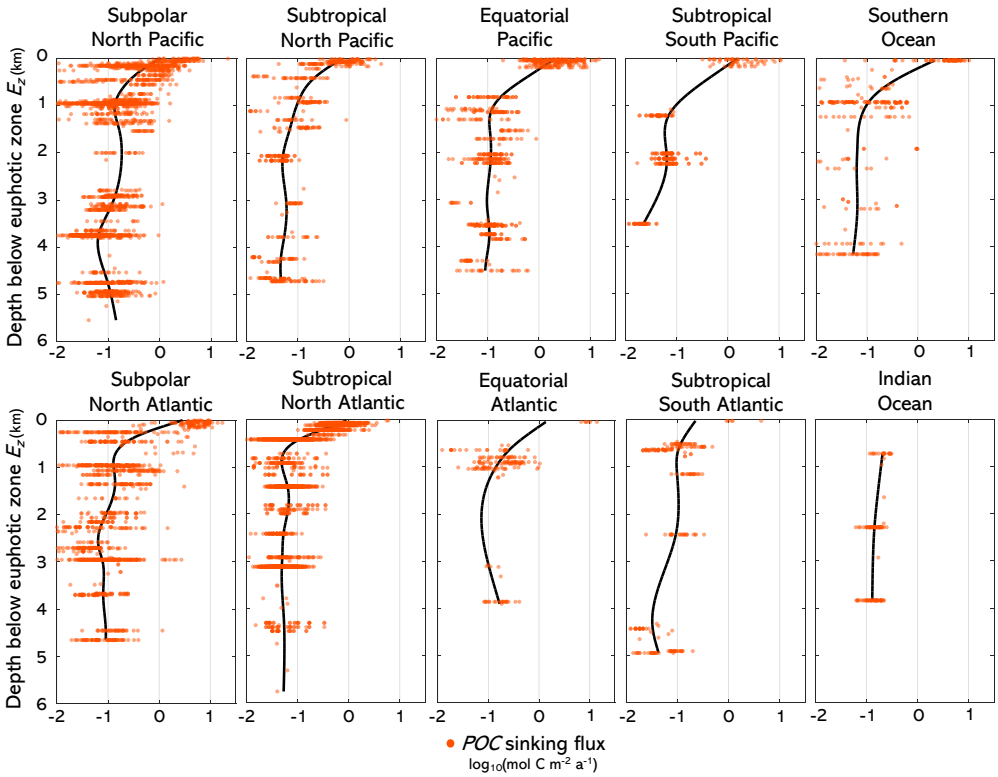

Figure S4. *POC* sinking fluxes as measured by sediment traps as a function of the water depth below E_z. Individual measurements are plotted as orange dots. The thick black lines are cubic smoothing splines used to interpolate discrete rates over depth and obtain regionally harmonized depth profiles.

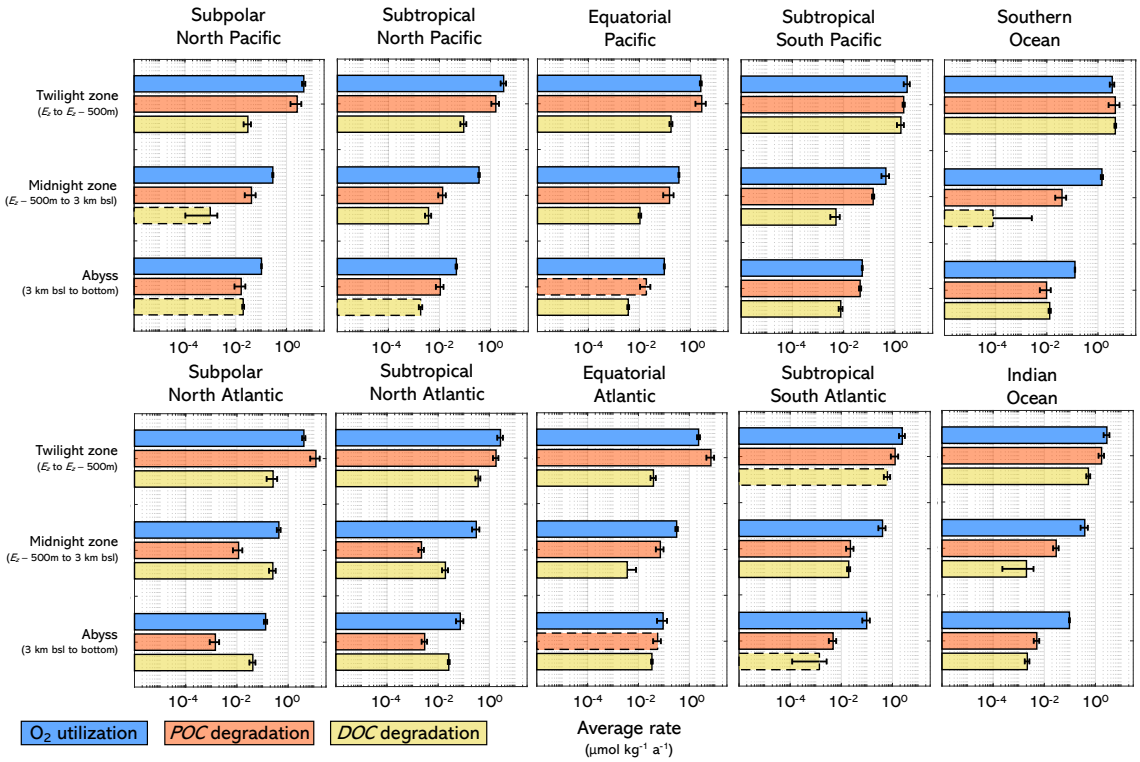

Figure S5. Regionally-averaged rates in three depth zones, the twilight zone (E_z to E_z – 500 m), the midnight zone (E_z – 500 m to 3 km below sea level) and the abyss (3 km below sea level to the bottom). All rates are expressed in μmol kg^{-1} a^{-1}. Dashed-contoured bars indicate negative values. Blue stands for oxygen utilization rate, orange is for *POC* consumption rate and yellow for *DOC* degradation rate.

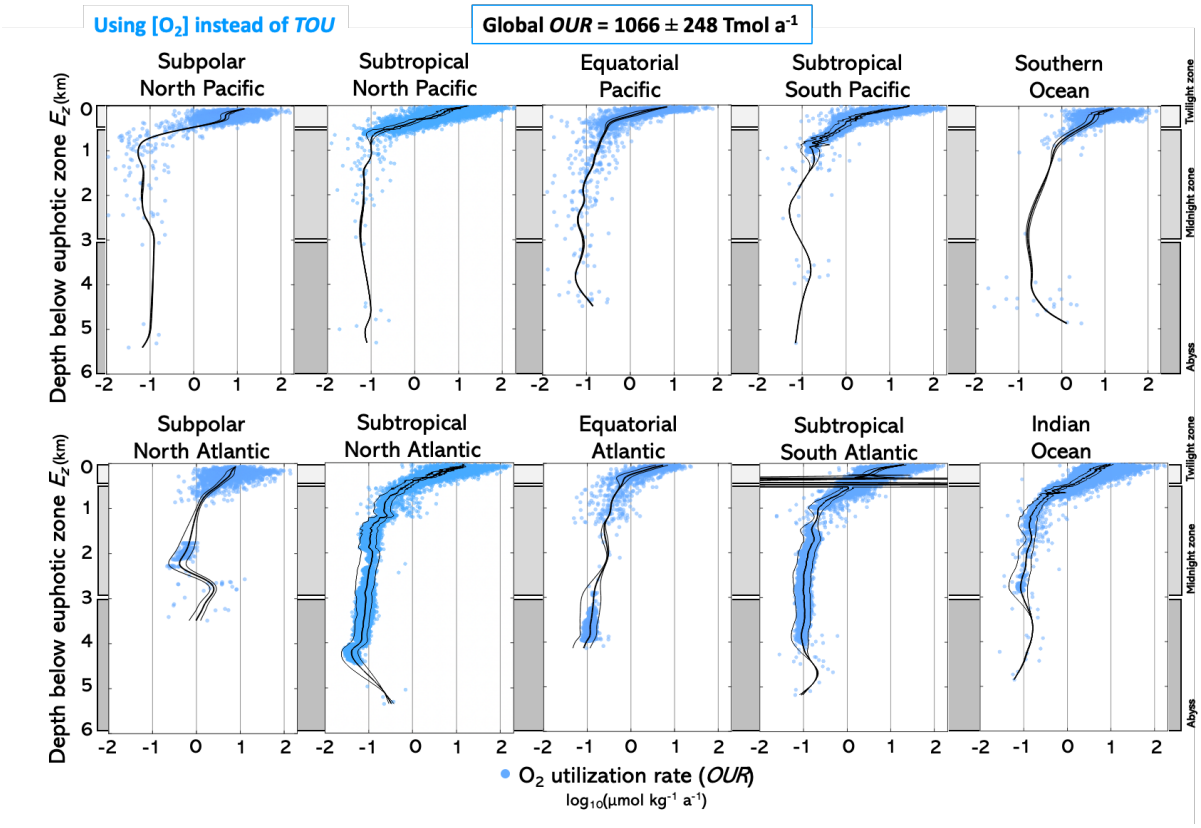

Figure S6. O_2 utilization rate (*OUR*), computed as the change in oxygen concentration [O_2] as a function of age, as a function of the water depth below E_z. This differs from the results presented in Fig. 5, in which *TOU* was used as a proxy for oxygen consumption, rather than [O_2]. Individual respiration rates resulting from 5000 Monte Carlo simulations are plotted as blue circles. The thick black lines are cubic smoothing splines used to interpolate discrete rates over depth and obtain regionally harmonized depth profiles. The thin black lines are cubic smoothing splines computed from individual rates plus or minus their associated uncertainty.

References

Anderson, L. A., & Sarmiento, J. L. (1994). Redfield ratios of remineralization determined by nutrient data analysis. *Global Biogeochemical Cycles*, *8*(1), 65–80.

Andersson, J. H., Wijsman, J. W. M., Herman, P. M. J., Middelburg, J. J., Soetaert, K., & Heip, C. (2004). Respiration patterns in the deep ocean. *Geophysical Research Letters*, *31*(3). https://doi.org/10.1029/2003GL018756

Antia, A. N., Koeve, W., Fischer, G., Blanz, T., Schulz-Bull, D., Schölten, J., Neuer, S., Kremling, K., Kuss, J., Peinert, R., Hebbeln, D., Bathmann, U., Conte, M., Fehner, U., & Zeitzschel, B. (2001). Basin-wide particulate carbon flux in the Atlantic Ocean: Regional export patterns and potential for atmospheric CO2 sequestration. *Global Biogeochemical Cycles*, *15*(4), 845–862. https://doi.org/10.1029/2000GB001376

Arístegui, J., Agustí, S., & Duarte, C. M. (2003). Respiration in the dark ocean. *Geophysical Research Letters*, *30*(2). https://doi.org/10.1029/2002gl016227

Arístegui, J., Agustí, S., Middelburg, J. J., & Duarte, C. M. (2005). Respiration in the mesopelagic and bathypelagic zones of the oceans. In P. A. del Giorgio & P. Williams (Eds.), *Respiration in Aquatic Ecosystems*.

Arístegui, J., Gasol, J. M., Duarte, C. M., & Herndl, G. J. (2009). Microbial oceanography of the dark ocean's pelagic realm. *Limnology and Oceanography*, *54*(5), 1501–1529.

Arístegui, J., Denis, M., Almunia, J., & Montero, M. F. (2002). Water-column remineralization in the Indian sector of the Southern Ocean during early spring. *Deep Sea Research Part II: Topical Studies in Oceanography*, *49*(9–10), 1707–1720. https://doi.org/10.1016/S0967-0645(02)00008-5

Baltar, F., Arístegui, J., Sintes, E., Gasol, J. M., Reinthaler, T., & Herndl, G. J. (2010). Significance of non-sinking particulate organic carbon and dark CO2fixation to heterotrophic carbon demand in the mesopelagic northeast Atlantic. *Geophysical Research Letters*, *37*(9), n/a-n/a. https://doi.org/10.1029/2010gl043105

Benner, R., Pakulski, J. D., McCarthy, M., Hedges, J. I., & Hatcher, P. G. (1992). Bulk Chemical Characteristics of Dissolved Organic Matter in the Ocean. *Science*, *255*(5051), 1561–1564. https://doi.org/10.1126/science.255.5051.1561

Berelson, W. M. (2001). Particle settling rates increase with depth in the ocean. *Deep-Sea Research II*, 49(1-3), 237–251. https://doi.org/10.1016/S0967-0645(01)00102-3

Broecker, W. S., Blanton, S., Smethie, W. M., & Ostlund, G. (1991). Radiocarbon decay and oxygen utilization in the Deep Atlantic Ocean. *Global Biogeochemical Cycles*, *5*(1), 87–117. https://doi.org/10.1029/90GB02279

Buesseler, K. O., Antia, A. N., Chen, M., Fowler, S. W., Gardner, W. D., Gustafsson, O., Harada, K., Michaels, A. F., Rutgers van der Loeff, M., Sarin, M., Steinberg, D. K., & Trull, T. (2007). An assessment of the use of sediment traps for estimating upper ocean particle fluxes. *Journal of Marine Research*, *65*, 345–416.

Buesseler, K. O., Boyd, P. W., Black, E. E., & Siegel, D. A. (2020). Metrics that matter for assessing the ocean biological carbon pump. *Proc Natl Acad Sci U S A*, *117*(18), 9679–9687. https://doi.org/10.1073/pnas.1918114117

Burdige, D. J., & Gardner, K. G. (1998). Molecular weight distribution of dissolved organic carbon in marine sediment pore waters. *Marine Chemistry*, *62*(1), 45–64. https://doi.org/10.1016/S0304-4203(98)00035-8

840 Burdige, D. J., & Komada, T. (2015). Sediment Pore Waters. In *Biogeochemistry of Marine*
841 *Dissolved Organic Matter* (pp. 535–577). Elsevier. https://doi.org/10.1016/B978-0-
842 12-405940-5.00012-1

843 Caesar, L., Rahmstorf, S., Robinson, A., Feulner, G., & Saba, V. (2018). Observed
844 fingerprint of a weakening Atlantic Ocean overturning circulation. *Nature*, *556*(7700),
845 Article 7700. https://doi.org/10.1038/s41586-018-0006-5

846 Cammen, L., Corwin, S., & Christensen, J. (1990). Electron transport system (ETS) activity
847 as a measure of benthic macrofaunal metabolism. *Marine Ecology Progress Series*,
848 *65*, 171–182. https://doi.org/10.3354/meps065171

849 Carter, B. R., Feely, R. A., Lauvset, S. K., Olsen, A., DeVries, T., & Sonnerup, R. (2021).
850 Preformed Properties for Marine Organic Matter and Carbonate Mineral Cycling
851 Quantification. *Global Biogeochemical Cycles*, *35*(1).
852 https://doi.org/10.1029/2020gb006623

853 Cassar, N., Nicholson, D., Khatiwala, S., & Cliff, E. (2021). Decomposing the Oxygen Signal
854 in the Ocean Interior: Beyond Decomposing Organic Matter. *Geophysical Research*
855 *Letters*, *48*(18), e2021GL092621. https://doi.org/10.1029/2021GL092621

856 Craig, H. (1971). The deep metabolism: Oxygen consumption in abyssal ocean water.
857 *Journal of Geophysical Research (1896-1977)*, *76*(21), 5078–5086.
858 https://doi.org/10.1029/JC076i021p05078

859 De Boor, C. (1978). *A practical guide to splines* (Vol. 27). Springer-verlag.

860 del Giorgio, P. A., & Duarte, C. M. (2002). Respiration in the open ocean. *Nature*, *420*, 379–
861 384.

862 DeVries, T. (2014). The oceanic anthropogenic CO2 sink: Storage, air-sea fluxes, and
863 transports over the industrial era. *Global Biogeochemical Cycles*, *28*(7), 631–647.
864 https://doi.org/10.1002/2013GB004739

865 DeVries, T., & Holzer, M. (2019). Radiocarbon and Helium Isotope Constraints on Deep
866 Ocean Ventilation and Mantle- ^{3} He Sources. *Journal of Geophysical Research:*
867 *Oceans*, *124*(5), 3036–3057. https://doi.org/10.1029/2018JC014716

868 DeVries, T., & Primeau, F. (2011). Dynamically and Observationally Constrained Estimates
869 of Water-Mass Distributions and Ages in the Global Ocean. *Journal of Physical*
870 *Oceanography*, *41*(12), 2381–2401. https://doi.org/10.1175/jpo-d-10-05011.1

871 DeVries, T., & Weber, T. (2017). The export and fate of organic matter in the ocean: New
872 constraints from combining satellite and oceanographic tracer observations. *Global*
873 *Biogeochemical Cycles*, *31*(3), 535–555. https://doi.org/10.1002/2016GB005551

874 Dinauer, A., Laufkötter, C., Doney, S. C., & Joos, F. (2022). What controls the large-scale
875 efficiency of carbon transfer through the ocean's mesopelagic zone? Insights from a
876 new, mechanistic model (MSPACMAM). *Global Biogeochemical Cycles*, *n/a*(n/a),
877 e2021GB007131. https://doi.org/10.1029/2021GB007131

878 Dittmar, T., Lennartz, S. T., Buck-Wiese, H., Hansell, D. A., Santinelli, C., Vanni, C.,
879 Blasius, B., & Hehemann, J.-H. (2021). Enigmatic persistence of dissolved organic
880 matter in the ocean. *Nature Reviews Earth & Environment Volume*, *2*, 570–583.

881 Dunne, J. P., Sarmiento, J. L., & Gnanadesikan, A. (2007). A synthesis of global particle
882 export from the surface ocean and cycling through the ocean interior and on the
883 seafloor. *Global Biogeochemical Cycles*, *21*(4).
884 https://doi.org/10.1029/2006gb002907

885 Duteil, O., Koeve, W., Oschlies, A., Bianchi, D., Galbraith, E., Kriest, I., & Matear, R.
886 (2013). A novel estimate of ocean oxygen utilisation points to a reduced rate of
887 respiration in the ocean interior. *Biogeosciences*, *10*(11), 7723–7738.
888 https://doi.org/10.5194/bg-10-7723-2013

889 Emerson, S. & Hedges, J. (2012). Chemical Oceanography and the Marine Carbon Cycle.
890 Cambridge University Press, Cambridge.

891 Fay, A. R., & McKinley, G. A. (2014). Global open-ocean biomes: Mean and temporal
892 variability. *Earth System Science Data*, *6*(2), 273–284. https://doi.org/10.5194/essd-6-
893 273-2014

894 Feely, R. A., Sabine, C. L., Schlitzer, R., Bullister, J. L., Mecking, S., & Greeley, D. (2004).
895 Oxygen Utilization and Organic Carbon Remineralization in the Upper Water Column
896 of the Pacific Ocean. *Journal of Oceanography*, *60*, 45–52.

897 Follet, C. L., Repeta, D. J., Rothman, D. H., Xu, L. & Santinelli, C. (2014) Hidden cycle
898 dissolved organic carbon in the deep ocean. *Proceedings of the National Academy of*
899 *Sciences*, *111*(47), 16706–16711. https://doi.org/10.1073/pnas.1407445111

900 Gebbie, G., & Huybers, P. (2012). The Mean Age of Ocean Waters Inferred from
901 Radiocarbon Observations: Sensitivity to Surface Sources and Accounting for Mixing
902 Histories. *Journal of Physical Oceanography*, *42*(2), 291–305.
903 https://doi.org/10.1175/jpo-d-11-043.1

904 GEBCO Compilation Group (2022) GEBCO_2022 Grid
905 (doi:10.5285/e0f0bb80-ab44-2739-e053-6c86abc0289c)

906 Global Monitoring and Forecast Center. (2021). *Operational Mercator Ocean*
907 *biogeochemical global ocean analysis and forecast system at 1/4 degree.*
908 https://resources.marine.copernicus.eu/?option=com_csw&view=details&product_id=
909 GLOBAL_ANALYSIS_FORECAST_BIO_001_028

910 Guo, H., Kriest, I., Oschlies, A. & Koeve, W. (under review). Can oxygen utilization rate be
911 used to track the long-term changes of aerobic respiration in the mesopelagic ocean?
912 *Authorea*, https://doi.org/10.22541/essoar.167205906.61781285/v1.

913 Hansell, D. A. (2013). Recalcitrant Dissolved Organic Carbon Fractions. *Annu. Rev. Mar.*
914 *Sci.*, *5*, 421–445.

915 Hansell, D. A., & Carlson, C. A. (2014). *Biogeochemistry of Marine Dissolved Organic*
916 *Matter*. Academic Press.

917 Hansell, D. A., Carlson, C. A., Rainer, M. W., Álvarez-Salgado, X. A., Yamashita, Y.,
918 Romera-Castillo, C., & Bif, M. B. (2021). *Compilation of dissolved organic matter*
919 *(DOM) data obtained from global ocean observations from 1994 to 2020 (NCEI*
920 *Accession 0227166)*. NOAA National Centers for Environmental Information.

921 He, Y.-C., Tjiputra, J., Langehaug, H. R., Jeansson, E., Gao, Y., Schwinger, J., & Olsen, A.
922 (2018). A Model-Based Evaluation of the Inverse Gaussian Transit-Time Distribution
923 Method for Inferring Anthropogenic Carbon Storage in the Ocean. *Journal of*
924 *Geophysical Research: Oceans*, *123*(3), 1777–1800.
925 https://doi.org/10.1002/2017jc013504

926 Helm, K. P., Bindoff, N. L., Church, J. A. (2011). Observed decreases in oxygen content of
927 the global ocean. *Geophysical Research Letters, 38*(23).
928 https://doi.org/10.1029/2011GL049513

Henson, S. A., Sanders, R., Madsen, E., Morris, P. J., Le Moigne, F., & Quartly, G. D. (2011). A reduced estimate of the strength of the ocean's biological carbon pump. *Geophysical Research Letters*, *38*(4). https://doi.org/10.1029/2011GL046735

Hewson, I., O'Neil, J. M., Fuhrman, J. A., & Dennison, W. C. (2001). Virus-like particle distribution and abundance in sediments and overlying waters along eutrophication gradients in two subtropical estuaries. *Limnology and Oceanography*, *46*(7), 1734–1746. https://doi.org/10.4319/lo.2001.46.7.1734

Hinga, K. R. (1985). Evidence for a higher average primary productivity in the Pacific than in the Atlantic Ocean. *Deep Sea Research Part A. Oceanographic Research Papers*, *32*(2), 117–126. https://doi.org/10.1016/0198-0149(85)90023-8

Holzer, M. (2022). The Fate of Oxygen in the Ocean and Its Sensitivity to Local Changes in Biological Production. *Journal of Geophysical Research: Oceans*, *127*(8), e2022JC018802. https://doi.org/10.1029/2022JC018802

Holzer, M., Smethie, W. M., & Ting, Y. (2018). Ventilation of the Subtropical North Atlantic: Locations and Times of Last Ventilation Estimated Using Tracer Constraints From GEOTRACES Section GA03. *Journal of Geophysical Research: Oceans*, *123*(4), 2332–2352. https://doi.org/10.1002/2017JC013698

Ito, T., Follows, M. J., & Boyle, E. A. (2004). Is AOU a good measure of respiration in the oceans? *Geophysical Research Letters*, *31*(17), n/a-n/a. https://doi.org/10.1029/2004gl020900

Jahnke, R. A. (1996). The global ocean flux of particulate organic carbon: Areal distribution and magnitude. *Global Biogeochemical Cycles*, *10*(1), 71–88. https://doi.org/10.1029/95gb03525

Jeansson, E., Steinfeldt, R., & Tanhua, T. (2021). *Water Mass Ages Based On GLODAPv2 Data Product (NCEI Accession 0226793)*. NOAA, National Centers for Environmental Information.

Jenkins, W. J. (1982). Oxygen utilization rates in North Atlantic subtropical gyre and primary production in oligotrophic systems. *Nature*, *300*(5889), 246–248.

Jenkins, W. J. (1998). Studying subtropical thermocline ventilation and circulation using tritium and 3He. *Journal of Geophysical Research: Oceans*, *103*(C8), 15817–15831. https://doi.org/10.1029/98JC00141

Johannes, R. E. (1965). Influence of Marine Protozoa on Nutrient Regeneration1. *Limnology and Oceanography*, *10*(3), 434–442. https://doi.org/10.4319/lo.1965.10.3.0434

Jørgensen, B. B., Wenzhöfer, F., Egger, M., & Glud, R. N. (2022). Sediment oxygen consumption: Role in the global marine carbon cycle. *Earth-Science Reviews*, *228*, 103987. https://doi.org/10.1016/j.earscirev.2022.103987

Karstensen, J., Stramma, L., & Visbeck, M. (2008). Oxygen minimum zones in the eastern tropical Atlantic and Pacific oceans. *Progress in Oceanography*, *77*(4), 331–350. https://doi.org/10.1016/j.pocean.2007.05.009

Keeling, R. F., & Garcia, H. E. (2002). The change in oceanic O2 inventory associated with recent global warming. *Proceedings of the National Academy of Sciences*, *99*(12), 7848–7853. https://doi.org/10.1073/pnas.122154899

Key, R. M., Kozyr, A., Sabine, C. L., Lee, K., Wanninkhof, R., Bullister, J. L., Feely, R. A., Millero, F. J., Mordy, C., & Peng, T.-H. (2004). A global ocean carbon climatology: Results from Global Data Analysis Project (GLODAP). *Global Biogeochemical Cycles*, *18*(4). https://doi.org/10.1029/2004GB002247

975 Key, R. M., Olsen, A., van Heuven, S., Lauvset, S. K., Velo, A., Lin, X., Schirnick, C.,
976 Kozyr, A., Tanhua, T., Hoppema, M., Jutterström, S., Steinfeldt, R., Jeansson, E.,
977 Ishii, M., Perez, F. F. & Suzuki, T. (2015). Global Ocean Data Analysis Project,
978 Version 2 (GLODAPv2), https://doi.org/10.3334/CDIAC/OTG.
979 NDP093_GLODAPv2

980 Koeve, W., & Kähler, P. (2016). Oxygen utilization rate (OUR) underestimates ocean
981 respiration: A model study. *Global Biogeochemical Cycles*, *30*(8), 1166–1182.
982 https://doi.org/10.1002/2015gb005354

983 Lauvset, S. K., Key, R. M., Olsen, A., van Heuven, S., Velo, A., Lin, X., Schirnick, C.,
984 Kozyr, A., Tanhua, T., Hoppema, M., Jutterström, S., Steinfeldt, R., Jeansson, E.,
985 Ishii, M., Perez, F. F., Suzuki, T., & Watelet, S. (2016). A new global interior ocean
986 mapped climatology: The 1° × 1° GLODAP version 2. *Earth System Science Data*,
987 *8*(2), 325–340. https://doi.org/10.5194/essd-8-325-2016

988 Laws, E. A., Falkowski, P. G., Smith Jr., W. O., Ducklow, H., & McCarthy, J. J. (2000).
989 Temperature effects on export production in the open ocean. *Global Biogeochemical*
990 *Cycles*, *14*(4), 1231–1246. https://doi.org/10.1029/1999GB001229

991 Loh, A. N., Bauer, J. E., & Druffel, E. R. M. (2004). Variable ageing and storage of dissolved
992 organic components in the open ocean. *Nature*, *430*(7002), Article 7002.
993 https://doi.org/10.1038/nature02780

994 Lønborg, C., Carreira, C., Jickells, T., & Álvarez-Salgado, X. A. (2020). Impacts of Global
995 Change on Ocean Dissolved Organic Carbon (DOC) Cycling. *Frontiers in Marine*
996 *Science*, *0*. https://doi.org/10.3389/fmars.2020.00466

997 Luther, G. W. (2021). Hydrothermal Vents Are a Source of Old Refractory Organic Carbon
998 to the Deep Ocean. *Geophysical Research Letters*, *48*(17), e2021GL094869.
999 https://doi.org/10.1029/2021GL094869

1000 Maerz, J., Six, K. D., Stemmler, I., Ahmerkamp, S., & Ilyina, T. (2020). Microstructure and
1001 composition of marine aggregates as co-determinants for vertical particulate organic
1002 carbon transfer in the global ocean. *Biogeosciences*, *17*(7), 1765–1803.
1003 https://doi.org/10.5194/bg-17-1765-2020

1004 Mare, M. F. (1942). A study of a marine benthic community with special reference to the
1005 micro-organisms. *Journal of the Marine Biological Association of the United*
1006 *Kingdom*, *25*(3), 517–554. https://doi.org/10.1017/S0025315400055132

1007 Martin, J. H., Knauer, G. A., Karl, D. M., & Broenkow, W. W. (1987). VERTEX: carbon
1008 cycling in the northeast Pacific. *Deep Sea Research Part A. Oceanographic Research*
1009 *Papers*, *34*(2), 267–285.

1010 McDougall, T. J., & Barker, P. M. (2011). *Getting started with TEOS-10 and the Gibbs*
1011 *Seawater (GSW) Oceanographic Toolbox, 28pp., SCOR/IAPSO WG127, ISBN 978-0-*
1012 *646-55621-5.*

1013 Menzel, D. W., & Ryther, J. H. (1968). Organic carbon and the oxygen minimum in the
1014 South Atlantic Ocean. *Deep Sea Research and Oceanographic Abstracts*, *15*(3), 327–
1015 337. https://doi.org/10.1016/0011-7471(68)90009-0

1016 Middelburg, J. J. (1989). A simple rate model for organic matter decomposition in marine
1017 sediments. *Geochimica et Cosmochimica Acta*, *53*(7), 1577–1581.
1018 https://doi.org/10.1016/0016-7037(89)90239-1

1019 Middelburg, J. J. (2019). *Marine Carbon Biogeochemistry: A Primer for Earth System*
1020 *Scientists*. Springer International Publishing. https://doi.org/10.1007/978-3-030-
1021 10822-9

1022 Morel, A., Huot, Y., Gentili, B., Werdell, P. J., Hooker, S. B., & Franz, B. A. (2007).
1023 Examining the consistency of products derived from various ocean color sensors in
1024 open ocean (Case 1) waters in the perspective of a multi-sensor approach. *Remote*
1025 *Sensing of Environment*, *111*(1), 69–88. https://doi.org/10.1016/j.rse.2007.03.012

1026 Mouw, C. B., Barnett, A., McKinley, G. A., Gloege, L., & Pilcher, D. (2016). Global ocean
1027 particulate organic carbon flux merged with satellite parameters. *Earth System*
1028 *Science Data*, *8*(2), 531–541. https://doi.org/10.5194/essd-8-531-2016

1029 Naqvi, S. W. A., Shailaja, M. S., Dileep Kumar, M., & Sen Gupta, R. (1996). Respiration
1030 rates in subsurface waters of the northern Indian Ocean: Evidence for low
1031 decomposition rates of organic matter within the water column in the Bay of Bengal.
1032 *Deep Sea Research Part II: Topical Studies in Oceanography*, *43*(1), 73–81.
1033 https://doi.org/10.1016/0967-0645(95)00080-1

1034 Ogawa, H., Amagai, Y., Koike, I., Kaiser, K., & Benner, R. (2001). Production of Refractory
1035 Dissolved Organic Matter by Bacteria. *Science*, *292*(5518), 917–920.
1036 https://doi.org/10.1126/science.1057627

1037 Olsen, A., Key, R. M., van Heuven, S., Lauvset, S. K., Velo, A., Lin, X., Schirnick, C.,
1038 Kozyr, A., Tanhua, T., Hoppema, M., Jutterström, S., Steinfeldt, R., Jeansson, E.,
1039 Ishii, M., Pérez, F. F., & Suzuki, T. (2016). The Global Ocean Data Analysis Project
1040 version 2 (GLODAPv2) – an internally consistent data product for the world ocean.
1041 *Earth System Science Data*, *8*, 297–323. https://doi.org/10.5194/essd-8-297-2016

1042 Oschlies, A., Brandt, P., Stramma, L., & Schmidtko, S. (2018). Drivers and mechanisms of
1043 ocean deoxygenation. *Nature Geoscience*, *11*(7), 467–473.
1044 https://doi.org/10.1038/s41561-018-0152-2

1045 Pan, X., Achterberg, E. P., Sanders, R., Poulton, A. J., Oliver, K. I. C., & Robinson, C.
1046 (2014). Dissolved organic carbon and apparent oxygen utilization in the Atlantic
1047 Ocean. *Deep Sea Research Part I: Oceanographic Research Papers*, *85*, 80–87.
1048 https://doi.org/10.1016/j.dsr.2013.12.003

1049 Pomeroy, L. R., & Johannes, R. E. (1968). Occurrence and respiration of ultraplankton in the
1050 upper 500 meters of the ocean. *Deep Sea Research and Oceanographic Abstracts*,
1051 *15*(3), 381–391. https://doi.org/10.1016/0011-7471(68)90014-4

1052 Primeau, F. W., Holzer, M. & DeVries, T. (2013). Southern Ocean nutrient trapping and the
1053 efficiency of the biological pump. *Journal of Geophysical Research: Oceans*, *118* (5),
1054 2547–2564.

1055 Redfield, A. C. (1958). The biological control of chemical factors in the environment.
1056 *American Scientist*, *46*, 205–221.

1057 Reygondeau, G., Guidi, L., Beaugrand, G., Henson, S. A., Koubbi, P., MacKenzie, B. R.,
1058 Sutton, T. T., Fioroni, M. & Maury, O. (2017). Global biogeochemical provinces of
1059 the mesopelagic zone. *Journal of Biogeography*, *45*(2), 500-514,
1060 https://doi.org/10.1111/jbi.13149.

1061 Roth, A. (2020, September 22). Bringing the Ocean's Midnight Zone Into the Light. *The New*
1062 *York Times*. https://www.nytimes.com/2020/09/22/science/monterey-bay-aquarium-
1063 midnight-zone.html

1064 Sarmiento, J. L., Thiele, G., Key, R. M., & Moore, W. S. (1990). Oxygen and nitrate new
1065 production and remineralization in the North Atlantic subtropical gyre. *Journal of*
1066 *Geophysical Research: Oceans*, *95*(C10), 18303–18315.
1067 https://doi.org/10.1029/JC095iC10p18303

1068 Sarmiento, J. L. & Gruber, N. (2006). Ocean Biogeochemical Dynamics, Princeton Univ.
1069 Press, Princeton.

1070 Shaw, T. J., Luther, G. W., Rosas, R., Oldham, V. E., Coffey, N. R., Ferry, J. L., Dias, D. M.
1071 C., Yücel, M., & Thibault de Chanvalon, A. (2021). Fe-catalyzed sulfide oxidation in
1072 hydrothermal plumes is a source of reactive oxygen species to the ocean. *Proceedings*
1073 *of the National Academy of Sciences*, *118*(40), e2026654118.
1074 https://doi.org/10.1073/pnas.2026654118

1075 Siegel, D. A., Buesseler, K. O., Doney, S. C., Sailley, S. F., Behrenfeld, M. J., & Boyd, P. W.
1076 (2014). Global assessment of ocean carbon export by combining satellite observations
1077 and food-web models. *Global Biogeochemical Cycles*, *28*(3), 181–196.
1078 https://doi.org/10.1002/2013gb004743

1079 Sonnerup, R. E., Mecking, S., & Bullister, J. L. (2013). Transit time distributions and oxygen
1080 utilization rates in the Northeast Pacific Ocean from chlorofluorocarbons and sulfur
1081 hexafluoride. *Deep Sea Research Part I: Oceanographic Research Papers*, *72*, 61–71.
1082 https://doi.org/10.1016/j.dsr.2012.10.013

1083 Sonnerup, R. E., Mecking, S., Bullister, J. L., & Warner, M. J. (2015). Transit time
1084 distributions and oxygen utilization rates from chlorofluorocarbons and sulfur
1085 hexafluoride in the Southeast Pacific Ocean. *Journal of Geophysical Research:*
1086 *Oceans*, *120*(5), 3761–3776. https://doi.org/10.1002/2015jc010781

1087 Sutton, T. T., Clark, M. R., Dunn, D. C., Halpin, P. N., Rogers, A. D., Guinotte, J., Bograd,
1088 S. J., Angel, M. V., Perez, J. A. A., Wishner, K., Haedrich, R. L., Lindsay, D. J.,
1089 Drazen, J. C., Vereshchaka, A., Piatkowski, U., Morato, T., Błachowiak-Samołyk, K.,
1090 Robison, B. H., Gjerde, K. M., Pierrot-Bults, A., Bernal, P., Reygondeau, G. & Heino,
1091 M. (2017). A global biogeographic classification of the mesopelagic zone. *Deep Sea*
1092 *Research Part I*, *126*, 85–102. https://doi.org/10.1016/j.dsr.2017.05.006.

1093 Trossman, D. S., Thompson, L., Mecking, S., Warner, M. J., Bryan, F. O., & Peacock, S.
1094 (2014). Evaluation of oceanic transport parameters using transient tracers from
1095 observations and model output. *Ocean Modelling*, *74*, 1–21.
1096 https://doi.org/10.1016/j.ocemod.2013.11.001

1097 Wang, W., Cai, M., Huang, P., Ke, H., Liu, M., Liu, L., Deng, H., Luo, B., Wang, C., Zheng,
1098 X., & Li, W. (2021). Transit Time Distributions and Apparent Oxygen Utilization
1099 Rates in Northern South China Sea Using Chlorofluorocarbons and Sulfur
1100 Hexafluoride Data—Wang—2021—Journal of Geophysical Research: Oceans—
1101 Wiley Online Library. *Journal of Geophysical Research Oceans*, *126*(8).
1102 https://agupubs-onlinelibrary-wiley-
1103 com.proxy.library.uu.nl/doi/10.1029/2021JC017535

1104 Waugh, D. W. (2003). Relationships among tracer ages. *Journal of Geophysical Research*,
1105 *108*(C5). https://doi.org/10.1029/2002jc001325

1106 Weber, T., Cram, J. A., Leung, S. W., DeVries, T., & Deutsch, C. (2016). Deep ocean
1107 nutrients imply large latitudinal variation in particle transfer efficiency. *Proc Natl*
1108 *Acad Sci USA*, *113*(31), 8606–8611. https://doi.org/10.1073/pnas.1604414113

1109 Whitney, F. A., Freeland, H. J., & Robert, M. (2007). Persistently declining oxygen levels in
1110 the interior waters of the eastern subarctic Pacific. *Progress in Oceanography*, *75*(2),
1111 179-199. https://doi.org/10.1016/j.pocean.2007.08.007
1112 Williams, P. M., Druffel, E. R. M., Williams, P., & Druffel, E. (1988). Dissolved Organic
1113 Matter in the Ocean: Comments on a Controversy. *Oceanography*, *1*(1), 14–17.
1114 Yamashita, Y., Mori, M. & Ogawa, H. (2023). Hydrothermal-derived black carbon as a
1115 source of recalcitrant dissolved organic carbon in the ocean. *Science Advances 9*(6),
1116 eade3807. https://doi.org/10.1126/sciadv.ade3807.
1117

Respiration patterns in the dark ocean

Olivier Sulpis[1,2], David S. Trossman[3], Mark Holzer[4], Emil Jeansson[5], Siv K. Lauvset[5] & Jack J. Middelburg[1]

[1]Earth Sciences, Utrecht University, Utrecht, The Netherlands
[2]CEREGE, Aix Marseille Univ, CNRS, IRD, INRAE, Collège de France, Aix-en-Provence, France
[3]Earth System Science Interdisciplinary Center, University of Maryland-College Park, College Park, USA
[4]Department of Applied Mathematics, School of Mathematics and Statistics, University of New South Wales, Sydney, Australia
[5]NORCE Norwegian Research Centre, Bjerknes Centre for Climate Research, Bergen, Norway

Key points

- *DOC* is important for microbial respiration in the abyssal ocean where the DOC consumption rate decreases with seawater mean age
- About 8% of O_2 utilization in the midnight zone and in the abyssal ocean is attributed to processes occurring at the seafloor
- Total dark ocean O_2 consumption (907 Tmol O_2 a^{-1}) is balanced by sediment O_2 (74 Tmol O_2 a^{-1}) and organic C consumption (727 Tmol C a^{-1})

Abstract

In the dark ocean, respiring organisms are the main sink for dissolved oxygen. The respiration rate in a given seawater volume can be quantified through dissolved oxygen drawdown or organic matter consumption as a function of time. Estimates of dissolved oxygen utilization rates (*OUR*) abound in the literature, but are typically obtained using proxies of questionable accuracy, often with low vertical resolution, and neglecting key regions such as the Southern and Indian oceans. Respiration rates based on particulate (*POC*) or dissolved (*DOC*) organic carbon are also sparsely observed and for *DOC* unavailable in many regions. Consequently, the relative contributions of *POC* or *DOC* as a respiration substrate in the dark ocean are unknown. Here we use recent datasets of true oxygen utilization, seawater age, and *DOC* to derive *OUR* and *DOC* consumption-rate profiles in 10 oceanic regions. We demonstrate that although *DOC* and *POC* consumption rates are globally consistent with *OUR*, they underestimate *OUR* in the deep, suggesting strong oxygen utilization at the seafloor. In the abyss, we find a negative correlation of *DOC* consumption rate with seawater age, suggesting that *DOC* reactivity decreases along the deep branch of the conveyor circulation. Our results highlight that benthic organisms are sensitive to perturbations in the surface production of organic matter and to large-scale circulation changes that affect its supply to the abyss.

1. Introduction

Oxygen concentrations in seawater span a wide range, resulting from exchanges with the atmosphere and sediments, production by photosynthesis, respiration by heterotrophs feeding on organic substances and (microbial) oxidation of reduced metabolites such as ammonium. Most organisms in the ocean interior rely on oxygen for respiration, and are thus vulnerable to the current growing deoxygenation observed across the oceans (e.g., Keeling & Garcia, 2002; Whitney et al., 2007; Helm et al., 2011; Oschlies et al., 2018). Yet, the nature of the organic material being used as an energy source for respiration, the rate of respiration, and its spatial distribution are still poorly known in the dark ocean. This impedes accurate assessments of the response of respiring marine organisms to environmental changes.

Marine organic carbon comprises particulate (*POC*) and dissolved (*DOC*) forms, operationally separated by a size limit (Arístegui et al., 2009). More than 99% of the respired *POC* in the dark ocean originates from invertebrate life forms (del Giorgio & Duarte, 2002), such as archaea, bacteria, protozoa, zoo- and phytoplankton, mostly packed within organic aggregates (Mare, 1942; Johannes, 1965; Pomeroy & Johannes, 1968). While organic matter from living organisms is fresh and labile, organic matter from dead organisms and settling aggregates is a heterogeneous mixture of compounds from various origins whose reactivity mostly decreases with its age (Middelburg, 2019; Dittmar et al., 2021). Ocean *DOC* is also characterized by a continuum of composition and reactivity (Hansell, 2013; Hansell & Carlson, 2014), but plays a more ambiguous role in respiration as it is both a substrate and a byproduct of organic matter degradation, released via leakage, unbalanced growth, viral lysis or incomplete digestion and solubilization (Hansell & Carlson, 2014; Middelburg, 2019; Dittmar et al., 2021). What is the reactivity of the *DOC* pool as a function of water depth, how does it vary among regions, and what is the importance of *DOC* relative to *POC* in marine respiration are still unanswered questions.

Globally, marine respiration mostly occurs in the ocean's euphotic layer (del Giorgio & Duarte, 2002). Out of ~50 Gt C a^{-1} of net surface-ocean primary production, between 5 and 12 Gt C a^{-1} are eventually exported as sinking *POC* and advected/diffused *DOC* to the ocean interior (Laws et al., 2000; Andersson et al., 2004; Dunne et al., 2007; Henson et al., 2011; Siegel et al., 2014; DeVries & Weber, 2017; Middelburg, 2019). It is believed that ~80% of the organic carbon exported from the euphotic layer is respired, degraded, and returned to dissolved inorganic carbon in the dark water column, and ~20% at the seafloor (Jahnke, 1996; Andersson et al., 2004; Middelburg, 2019). However, estimates of respiration rates vary widely, with rates estimated from measured or modeled *POC*-flux attenuation usually being much lower than those based on measured respiratory activity, which provides integrated carbon consumption rate over a specific depth range, predicting global, dark-ocean respiration rates as high as 33 Gt C a^{-1} (Arístegui et al., 2003). A more direct approach involves using changes in dissolved oxygen as a function of time, but these data are either limited to the surface layer where incubation time can be short or based on the combination of dissolved oxygen measurements and water-age estimates.

Once a parcel of seawater leaves the surface and enters the ocean interior, its dissolved oxygen concentration should decrease with time, as oxygen is being used by respiring organisms (Craig, 1971). Apparent Oxygen Utilization (*AOU*) is the difference between the dissolved oxygen concentration of seawater at equilibrium with the atmosphere at a given temperature and salinity and the measured dissolved oxygen concentration. *AOU* has been used to estimate oxygen utilization rates (*OUR*) by dividing *AOU* by seawater age (Sarmiento et al.,

1990; Feely et al., 2004; Karstensen et al., 2008). However, this is an imperfect approach because *AOU* usually overestimates oxygen utilization because water parcels are rarely at equilibrium with the atmosphere when they start their journey to the ocean interior (Ito et al., 2004; Duteil et al., 2013; Koeve & Kähler, 2016; DeVries & Holzer, 2019; Holzer, 2022). Alternatively, we can calculate oxygen utilization rates as the dissolved oxygen changes over a given amount of time (Jenkins, 1982; Hinga, 1985; Sonnerup et al., 2013, 2015). This reduces uncertainties related to air-sea disequilibrium, but would require a larger amount of data and accurate seawater ages and implicitly assumes steady-state conditions. Both approaches, i.e., *AOU* divided by seawater age and oxygen changes regressed againts multiple seawater ages, have provided some historical *OUR* estimates in various regions of the Pacific and Atlantic, but the depth resolution is often low, and historically data-scarce oceanic regions such as the Indian or Southern oceans have been largely neglected. Additionally, regional comparisons are difficult because *OUR* depth profiles across ocean basins are not often obtained with the same method.

Our purpose here is to rigorously assess the depth and regional patterns of respiration rates in the dark ocean, using three independent proxies: (i) changes in dissolved oxygen along water-mass pathways, (ii) changes in *DOC* concentration along water-mass pathways and (iii) changes in *POC* sinking fluxes. For (i) and (ii), we use a recently published dataset of Transit Time Distribution (TTD) ages (Jeansson et al., 2021), which provides accurate water-mass-age estimates considering mixing occurring into the ocean interior (Waugh, 2003), a novel True Oxygen Utilization (*TOU*) data product that accounts for air-sea disequilibrium (DeVries & Primeau, 2011; DeVries, 2014; DeVries & Holzer, 2019; Holzer, 2022), and a recently published dataset of quality-controlled, seawater DOC concentration (Hansell et al., 2021), to derive depth profiles of *OUR* and *DOC* consumption rate in 10 major oceanic regions. By separating the water column in three depth realms (twilight zone, midnight zone and abyss, defined later) we demonstrate that although *DOC* and *POC* consumption rates are consistent with *OUR* at a global scale, they persistently underestimate *OUR* in the deeper part of the water column. This suggests strong, ubiquitous oxygen utilization at the seafloor that is not reflected in the *POC* and *DOC* data. These results have implications for Anthropocene-ocean ecosystems, as they highlight that abyssal microbial and animal communities are sensitive to any perturbation in organic material delivery to the deep ocean originating from the surface.

2. Methods

2.1. True oxygen utilization (*TOU*)

True oxygen utilization (*TOU*, Fig. 1) was computed as the difference between the preformed and measured oxygen concentrations. Unlike *AOU*, *TOU* is a model tracer which accounts for oxygen saturation states other than 100% (mostly lower) in surface water at the time of water mass formation as well as interior ocean mixing in the presence of nonlinearity in the solubility of oxygen (Ito et al., 2004; Koeve & Kähler, 2016). Preformed oxygen was estimated by propagating the GLODAPv2.2016 (Lauvset et al., 2016) mapped climatologies of surface oxygen into the ocean interior using OCIM2, a steady-flow data-assimilated ocean circulation inverse model in its 24-level, 2x2-degree control version (DeVries and Holzer, 2019). This model is constrained by observed ^{14}C, CFCs, ^{3}He, surface heat, freshwater fluxes, sea-surface height, temperature and salinity (Holzer et al., 2018; DeVries & Holzer, 2019; Holzer, 2022). Preformed and observed oxygen concentrations were then linearly interpolated in three dimensions from the OCIM2 grid back to GLODAPv2 coordinates. This *TOU* product

compares well with other recent, independent *TOU* estimates (Carter et al., 2021; Cassar et al., 2021), see Fig. S1.

To assess the uncertainty in the model-predicted preformed oxygen concentrations, we compared the preformed oxygen as predicted by 7 different versions of OCIM2 having different vertical resolution (24 levels or 48 levels) and/or different eddy diffusivities (DeVries and Holzer, 2019; Holzer et al., 2021). The mean standard deviation of the preformed oxygen across these 7 simulations was ~6%. The uncertainty of the GLODAPv2 oxygen data is estimated to be about 1% (Olsen et al., 2016). To reflect both the uncertainty surrounding preformed oxygen and that surrounding measured oxygen, we set the relative uncertainty of the *TOU* estimates to a conservative value of 10%.

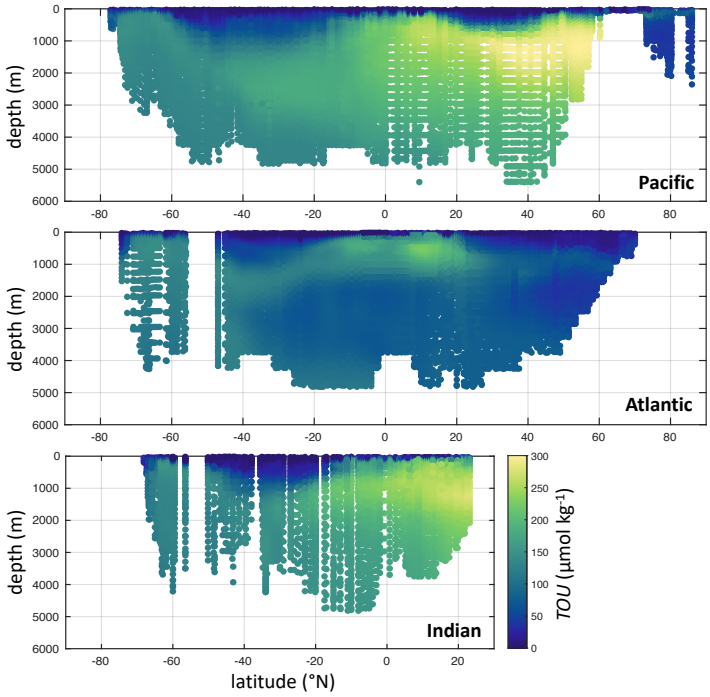

Figure 1. *TOU* depth profiles in the Pacific (all data between 160°W and 180°W), Atlantic (all data between 20°W and 30°W) and Indian (all data between 60°E and 80°E) Oceans.

2.2. Seawater age

The age of seawater was obtained using a two-parameter (mean and width) transit-time-distribution (TTD) approach based on measured GLODAPv2.2016 CFC-12 concentrations (Olsen et al., 2016), assuming a ratio of mean/width of 1. Unlike traditional tracer-based ages, TTD ages keep track of seawater mixing history by including corrections for mixing during transport away from the surface ocean. We assume minimal bias associated with the resulting TTD ages in regions with more than one peak in the TTD (e.g., portions of the Southern Ocean; Trossman et al., 2014) and that the TTD ages are valid up to 300 years from the limited (~80 year) time history of the ventilation tracers used to estimate the TTD. The TTD age product (Jeansson et al., 2021) is available online at https://www.ncei.noaa.gov/access/ocean-carbon-data-system/oceans/ndp_108/ndp108.html. Because of the relatively short history of CFC-12 and the anthropogenic influence on ^{14}C mean ages in younger waters, for samples with CFC-12 TTD ages greater than 300 years, we instead use the seawater 'mean age' from (Gebbie & Huybers, 2012), who applied an inverse modeling technique on GLODAPv1.1 ^{14}C data (Key

et al., 2004). To avoid an abrupt transition between CFC-12 TTD ages and ^{14}C mean ages, for samples with TTD ages between 200 and 300 years, a transition function is applied to compute ages as a weighted average between the CFC-12 TTD ages and ^{14}C mean ages. For all water masses younger than 200 years, we used the CFC-12 TTD ages. This composite seawater age product is shown in Fig. 2. We set the overall relative uncertainty associated with seawater ages to 20%, which should encompass both the uncertainty associated with the TTD method reported by He et al. (2018) and the uncertainty associated with ^{14}C mean ages (Gebbie & Huybers, 2012), neglecting the influence of exotic waters such as from groundwater seepage, hydrothermal vents or ice sheets. This composite age product is broadly consistent within its uncertainty with ages from the OCIM2 model in its 24-level, 2x2-degree control version (DeVries and Holzer, 2019), see Fig. S2.

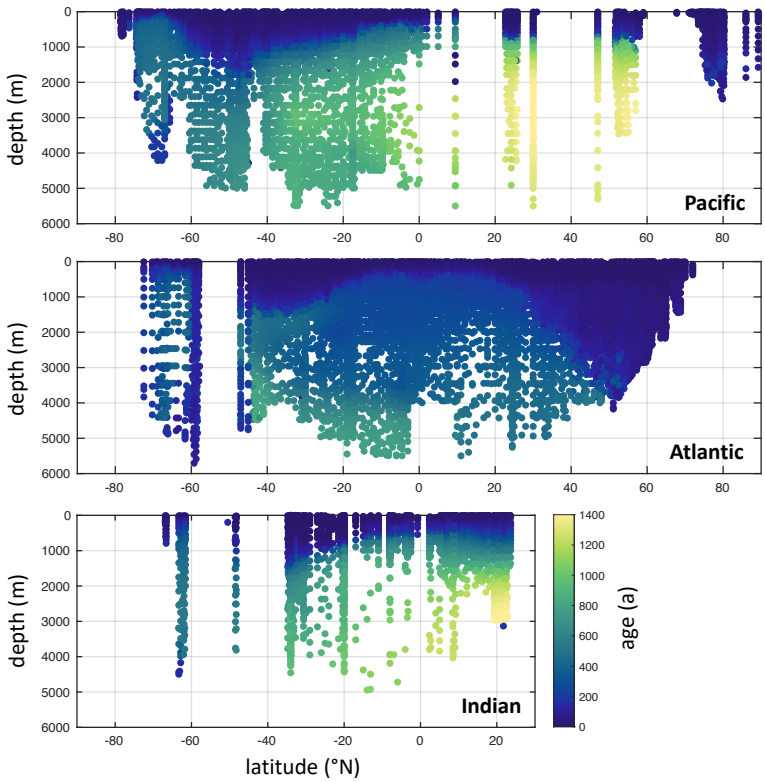

Figure 2. Seawater age depth profiles in the Pacific (all data between 160°W and 180°W), Atlantic (all data between 20°W and 30°W) and Indian (all data between 60°E and 80°E) Oceans.

2.3. Regions

We grouped the data by region using the global open-ocean core biome distribution of Fay and McKinley (2014), which is defined using criteria based on sea surface temperature, chlorophyll-a concentration, sea-ice fraction and maximum mixed-layer depth. Thus, the regions considered for the present analysis are distinguished based on ocean surface biogeochemical factors rather than water masses or topography (Fig. 3a). To avoid issues associated with under-sampled, narrow regions, we merged four biome pairs as defined by Fay and McKinley (2014) into four distinct regions: the equatorial Pacific east and west, the subpolar and the subtropical seasonally stratified North Pacific, the subpolar and the subtropical seasonally stratified North Atlantic, and the subpolar and the subtropical seasonally stratified Southern Ocean. We also excluded the Arctic and southernmost biomes, which are seasonally covered by sea ice, due to fewer data available, and due to the complexity of

isopycnal contours in those regions. Thus, we analyze ten biogeochemically distinct regions here. The exclusion of high-latitude systems implies that our global estimates are conservative. We acknowledge that the choice of regions is subjective, and that other sets of biogeochemical regions have been defined for the mesopelagic realm (Reygondeau et al., 2017; Sutton et al., 2017). Applying our analysis in those regions could be the focus of future work.

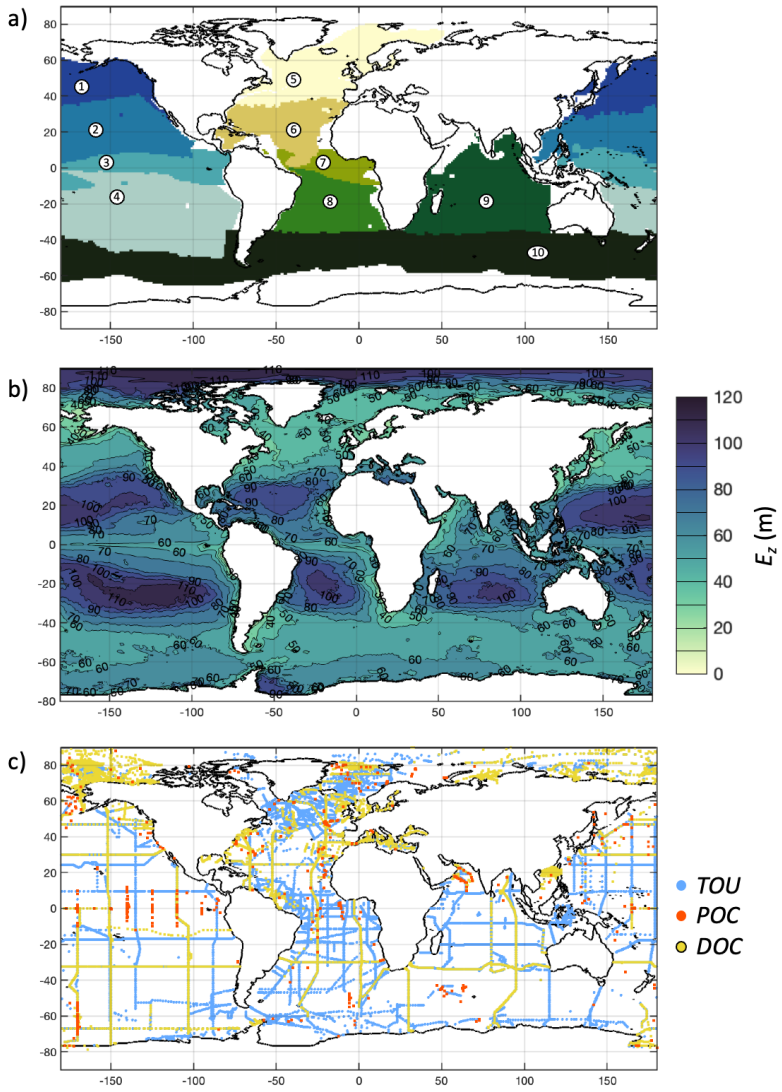

Figure 3. a) Geographical boundaries of the 10 regions used for our study: 1, subpolar North Pacific, 2, subtropical North Pacific, 3, Equatorial Pacific, 4, subtropical South Pacific, 5, subpolar North Atlantic, 6, subtropical North Atlantic, 7, Equatorial Atlantic, 8, subtropical South Atlantic, 9, Indian Ocean and 10, Southern Ocean. **b)** Euphotic zone depth, where contour lines mark 10-m intervals. **c)** Locations of *TOU* (blue circles), *POC* (orange circles) and *DOC* (yellow circles) data points.

2.4. Euphotic-zone-referenced depth metrics

As pointed out by Buesseler et al. (2020), depth patterns related to the marine biological carbon pump can appear quite different depending on whether the *POC* fluxes are assessed at a fixed reference depth (e.g. the air-sea interface) or relative to the depth at the base of the euphotic zone (E_z). Because E_z varies with location, E_z should be a preferred reference depth when comparing among regions (Buesseler et al., 2020). We computed E_z (Fig. 3b) as a

function of the surface chlorophyll concentration following Eq. (10) in the work of Morel et al. (2007), which corresponds to the depth at which the downward photosynthetically active radiation falls to 1% of its subsurface value. Surface chlorophyll concentrations were taken from the Operational Mercator Ocean biogeochemical global ocean analysis and forecast system at 1/4 degree (Global Monitoring and Forecast Center, 2021), averaged between the months of January 2019 and September 2021, which corresponds at the time of writing to all the data available from this source. E_z was then spatially averaged in each region. Regionally-averaged E_z is the deepest in the subtropical North Pacific (89 m below sea surface) and the shallowest in the subpolar North Atlantic (46 m below sea surface). All depth profiles shown here are expressed relative to E_z.

In addition to continuous depth profiles, we also express results in terms of three predefined depth zones: (i) the *twilight zone*, between E_z and E_z + 500 m, (ii) the *midnight zone* (Roth, 2020) between E_z + 500 m and 3 km depth (below sea level), and (iii) the *abyss*, between 3 km depth and the bottom.

2.5. O_2 utilization rate (*OUR*)

For each region, *TOU* data were sorted according to increasing water neutral density (γ), taken from GLODAPv2 (Olsen et al., 2016), and placed into bins centered around predefined γ values; these bins constitute the isopycnals. The density bins span a broad density range, from γ = 20.0 to γ = 28.8 kg m^{-3}, and are separated by a γ increment kept constant over the entire γ range, that randomly varies between 0.0005 and 0.01 across 5000 Monte Carlo simulations. That is, for each Monte Carlo simulation, isopycnals were centered around different neutral density values and included a different amount of data points. This Monte Carlo approach also allows us to propagate the *TOU* uncertainty (10%) and the age uncertainty (20%) into the final respiration rates, as well as to obtain *OUR* estimates centered around different isopycnals and to maximize the depth coverage of the *OUR* profiles. For each density bin, we performed a linear fit of *TOU* versus seawater age using the MATLAB *fitlm* function and the built-in 'robust regression' option that reduces outlier effects. From each fit, we extract the slope, standard error associated with the slope, and the p-value testing the null hypothesis of zero slope, i.e., that *TOU* and age are independent. The slope of the *TOU*-age linear relationship corresponds to *OUR* expressed in μmol kg^{-1} a^{-1}. Only *OUR* resulting from a statistically significant relationship between *TOU* and age ($p < 0.05$) were retained.

To test the robustness of our approach, we also replicated our entire analysis using simply GLODAPv2 oxygen concentrations ([O_2]), instead of *TOU* (Fig. S6). That is, rather than computing *OUR* as the slope of a linear fit of *TOU* versus seawater age, we compute another version of *OUR*, defined as the slope of a linear fit of measured [O_2] versus seawater age along a given isopycnal. At steady state, the main difference between the [O_2] and the *TOU* approaches is how water mixing is dealt with. All results described in this study are based on the *TOU* approach, and a brief comparison with results obtained from the [O_2] approach is provided in the discussion section 4.1.

2.6. *DOC* consumption rate

The procedure to estimate *DOC* consumption rate profiles is identical to that described in the previous subsection for *OUR*, except that instead of *TOU*, *DOC* concentrations are used. We used the dissolved organic matter dataset of Hansell et al. (2021) that includes quality-controlled, in situ *DOC* concentration measurements collected between 1994 and 2019 in all

10 regions, representing a total of more than 90,000 data points, see Fig. 3c. *DOC* concentrations, shown in Fig. 4, were always highest near the ocean surface, commonly above 100 µmol kg^{-1}, and decreased with depth to stabilize at 35-40 µmol kg^{-1}. Seawater ages were assigned to each *DOC* estimate by linearly interpolating the seawater ages shown in Fig. 2 in three dimensions to match the coordinates of the *DOC* samples. Seawater neutral density was absent from the *DOC* dataset, but present in the GLODAPv2 data product. Thus, for each of the 10 regions, whose bounds roughly follow outcropping isopycnal contours, we fitted a linear regression model to predict GLODAPv2 neutral density as a function of GLODAPv2 absolute salinity and conservative temperature. In turn, in each region, the regression model was used to compute the neutral density associated with each *DOC* sample based on the sample's conservative temperature and absolute salinity, calculated with the TEOS-10 toolbox (McDougall & Barker, 2011). Net *DOC* consumption rates are expressed in µmol kg^{-1} a^{-1}, where a positive value indicates *DOC* consumption, and a negative value indicates *DOC* production or input.

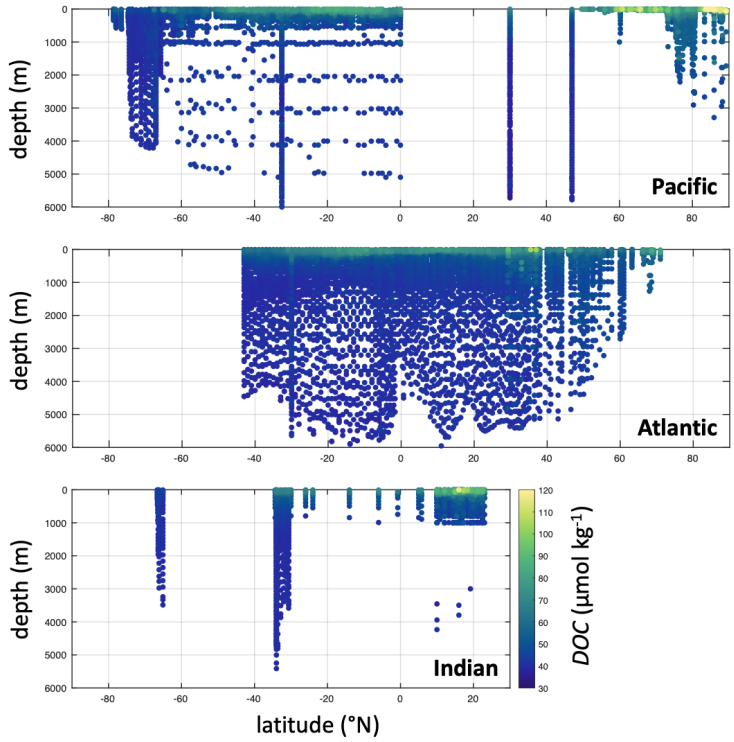

Figure 4. Dissolved organic carbon concentration (*DOC*) depth profiles in the Pacific (all data between 160°W and 180°W), Atlantic (all data between 20°W and 30°W) and Indian (all data between 60°E and 80°E) Oceans.

2.7. *POC* consumption rates

POC flux measurements from the sediment-trap dataset of Mouw et al. (2016) were used. In each region, *POC* fluxes were sorted according to increasing depth and interpolated in the vertical using a cubic smoothing spline from the MATLAB curve-fitting toolbox (smoothing parameter $p = 1\times10^{-6}$, De Boor, 1978). This allows us to turn discrete values into continuous estimates over depth and obtain regionally harmonized depth profiles of *POC* settling fluxes. These fluxes were used to compute *POC* consumption rates in three predefined depth zones, defined in *Methods section 2.4.*: (i) the *twilight zone*, (ii) the *midnight zone*, and (iii) the *abyss*. In each zone, the difference between the deepest and the shallowest flux is

divided by the zone height, and the resulting consumption rate is then converted into μmol kg^{-1} a^{-1}. A positive value indicates *POC* consumption, and a negative value indicates *POC* production.

2.8. Sediment oxygen uptake

To assess the contribution of seafloor processes to the *OUR* throughout the water column, we compared the horizontally integrated *OUR* profiles derived in this study, termed the 'total' *OUR*, with horizontally integrated 'seafloor' *OUR* estimates. We computed seafloor *OUR* using the multicomponent linear regression model of Eq. 5.1 in the work of Jørgensen et al. (2022), which predicts total oxygen uptake rate as a function of seafloor depth and euphotic net primary production. This regression model was established using 798 *in situ* measurements of oxygen utilization rate at the seafloor, distributed throughout the world oceans (Jørgensen et al., 2022). As in the work of Jørgensen et al. (2022), we used the satellite-based monthly climatology of net primary production available from Oregon State University averaged over a 10-year period (1998-2007). Bathymetry data are from the GEBCO Compilation Group (2022).

3. Results

Between the top and bottom of the twilight zone, i.e., within the 500 meters beneath the base of the euphotic layer, *OUR* decreases by about one order of magnitude (Fig. 5, 6). In the twilight zone, the *OUR* attenuation with depth can be well-described with a power law similar to a "Martin curve" (Martin et al., 1987), i.e., $OUR = C \times (z/E_z)^{-b}$, where C is a fitted amplitude, z is the depth below the euphotic zone (depth E_z), and b is a fitted attenuation parameter with a value of 1.21 when data from all regions are merged (Fig. 6). The attenuation parameter describes how steeply *OUR* decreases with depth, and is in practice dependent on the balance between organic matter reactivity, settling velocity and seawater viscosity (Sarmiento & Gruber, 2006; Dinauer et al., 2022). The attenuation parameter varies regionally, and according to our results, is higher (steeper *OUR* decrease) in subtropical regions, and lower (smoother *OUR* decrease) in low- and high-latitudes region (Fig. S3). This is consistent with a more efficient *POC* transfer to the deep ocean (low b) in productive, high-latitudes regions than in low-productivity regions such as subtropical gyres, where more *POC* is consumed near-surface and less reaches the deep ocean (high b). This interpretation agrees with other studies (Berelson, 2001; Sarmiento & Gruber, 2006; Weber et al., 2016; Maerz et al., 2020; Dinauer et al., 2022). Averaged over the entire twilight zone, *OUR* is highest in subpolar regions (subpolar North Pacific and Atlantic, Southern Ocean; 3.6-4.8 μmol kg^{-1} a^{-1}) and lowest in equatorial regions (equatorial Pacific and Atlantic; 2.3-2.6 μmol kg^{-1} a^{-1}), see Fig. 7 and Table S1. We note, however, that a power law does not match well *OUR* in the midnight zone and that the power-law fit was not performed in a log-space, which influences the weighting.

Within the midnight zone, i.e., from the bottom of the twilight zone to 3 km below sea level, *OUR* shows a smoother decrease with depth (Fig. 5) and, except for the Southern Ocean, is less variable regionally than in the twilight zone (Table S1). In the midnight zone, data density is very low in the Southern Ocean, where the only available *OUR* estimates are in or near the upper kilometer of the water column (Fig. 5). This explains the relatively high *OUR* estimate in that region (1.4 ± 0.1 μmol kg^{-1} a^{-1}), when compared to other regions where more data is available deeper, see Fig. 7). In the abyss (below 3 km depth), *OUR* does not show a particular trend with depth (Fig. 5). Among all regions (Fig. 7), abyssal *OUR* lies in a narrow

range, with the lowest values in the Pacific gyres and in the subtropical North Atlantic (Table S1).

DOC consumption-rate profiles (Fig. 8) show patterns similar to those of the *OUR* profiles, decreasing by at least an order of magnitude in the twilight zone. Note that *DOC* is not only consumed in the deep sea, but also produced by solubilization and sloppy feeding, and released from sediments and hydrothermal vents (Hansell and Carlson, 2004; Luther, 2021; Yamashita et al., 2023). Consumption rates are *net* rates and thus occasionally appear negative (net *DOC* source). Negative *DOC* consumption rates are not shown in Fig. 8 for clarity but are included in the budgets shown in Fig. 9, S4 and Table S1.

POC fluxes show an expected decrease with depth in all regions (Fig. S4), but the variability is very large, which hinders interpretation of the data. When merging *POC* fluxes from all regions, the POC flux attenuation with depth is well described by a power law, with an attenuation parameter $b = 0.53$ (Fig. 6). This value is lower than for *OUR*, and lower than from other estimates from the literature (Middelburg, 2019). *POC* fluxes may be underestimated near the surface, due to the presence of "swimmers" in sediment traps (Buesseler et al., 2007) which actively enter the traps and feed on the collected organic material, leading to an underestimation of the flux attenuation. *POC* consumption rates are lower (Fig. 7) in the gyres than in highly productive regions such as the North Atlantic, the Southern Ocean or the low latitudes (Dunne et al., 2007).

DOC consumption rates are generally lower than *POC* consumption rates, but there are important regional exceptions where *DOC* consumption is on par (Southern Ocean) or larger (North Atlantic midnight zone and 5 abyssal regions; Figs. 7, S5, Table S1). In the twilight zone, for 5 regions out of 10 (Fig. 9), the sum of *DOC* and *POC* consumption rates (expressed in moles of C per kg per year) lies within the uncertainty bounds of *OUR* (expressed in terms of moles of O_2 per kg per year). In the midnight zone as well as in the abyss, the sum of *DOC* and *POC* consumption rates is significantly lower than *OUR* in all regions (Fig. 9). This suggests the presence of another sink of O_2 in these two depth zones, likely O_2 utilization at the seafloor (see Discussion). In the abyss, in 5 regions out of 10, the *DOC* consumption rates are significantly higher than the *POC* ones (Fig. 9, Table S1), meaning that *DOC* is the main substrate for abyssal respiration.

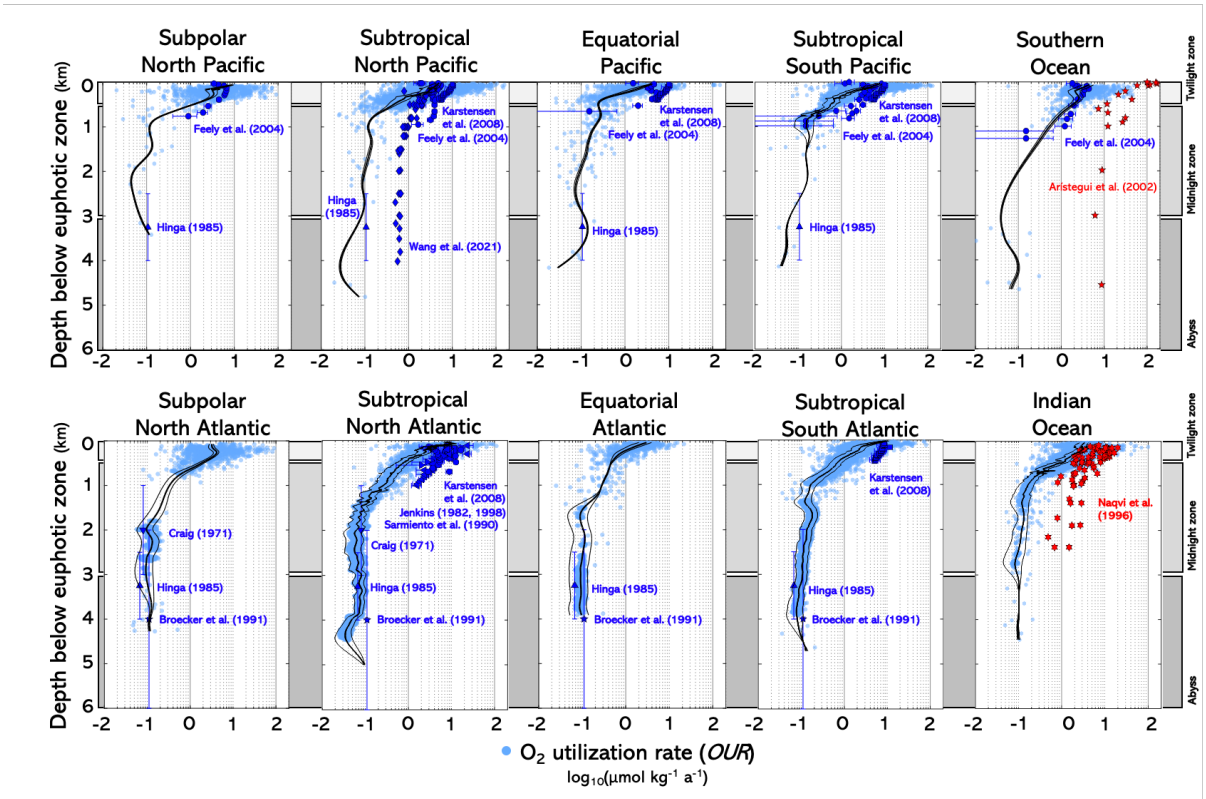

Figure 5. O_2 utilization rate (*OUR*) as a function of the water depth below E_z. Individual respiration rates resulting from 5000 Monte Carlo simulations are plotted as blue circles. The thick black lines are cubic smoothing splines used to interpolate discrete rates over depth and obtain regionally harmonized depth profiles. The thin black lines are cubic smoothing splines computed from individual rates plus or minus their associated uncertainty. Dark blue markers are *OUR* estimates from previous studies. Dark red markers are estimates of the oxygen consumption rate derived from electron transport systems (ETS) activity measurements, taken from two previous studies. The data and brief descriptions of the previous studies' methods are archived on Zenodo (https://doi.org/10.5281/zenodo.7632177).

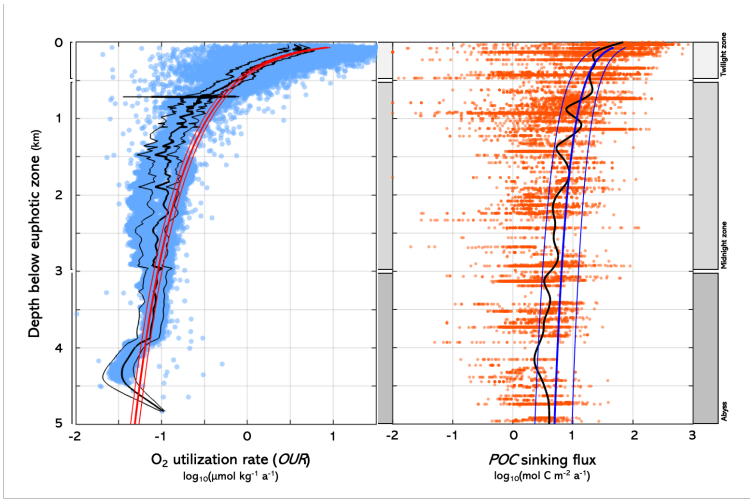

Figure 6. O_2 utilization rate (*OUR*) and *POC* sinking fluxes as a function of the water depth below E_z. Individual respiration rates resulting from 5000 Monte Carlo simulations are plotted as blue circles and individual sediment-trap measurements are plotted as orange circles. The thick black lines are cubic smoothing splines used to interpolate data over depth and obtain regionally harmonized depth profiles. The thin black lines are cubic smoothing splines computed from individual rates plus or minus their associated uncertainty. Solid thin red (for *OUR*) and blue (for *POC* fluxes) lines are fitted power laws, $OUR = 9.2\ (\pm 0.5) \times (z/E_z)^{-1.21\ (\pm 0.02)}$ and *POC* finking flux $= 49\ (\pm 14) \times (z/E_z)^{-0.53\ (\pm 0.06)}$, respectively, and surrounding thin lines represent the uncertainty range.

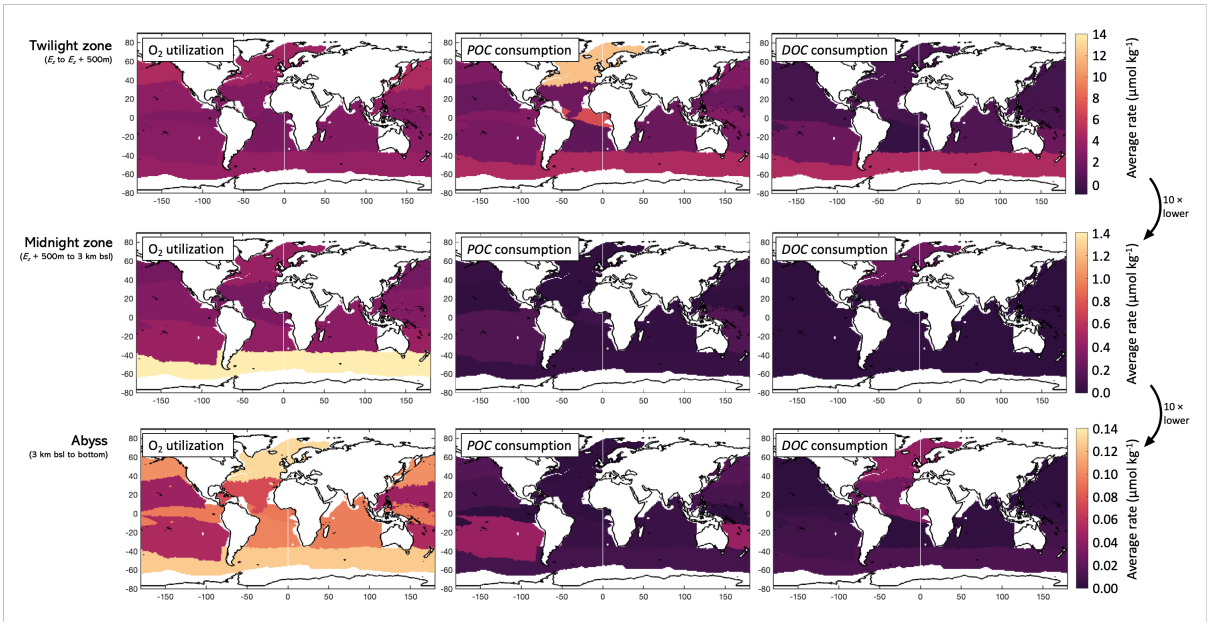

Figure 7. Regionally-averaged rates in all regions and in three depth zones, the twilight zone (top row, E_z to E_z + 500 m), the midnight zone (middle row, E_z + 500 m to 3 km below sea level) and the abyss (bottom row, 3 km below sea level to the bottom). Note the bounds of the color axes are the same for each row, each being an order of magnitude smaller than those of the row above.

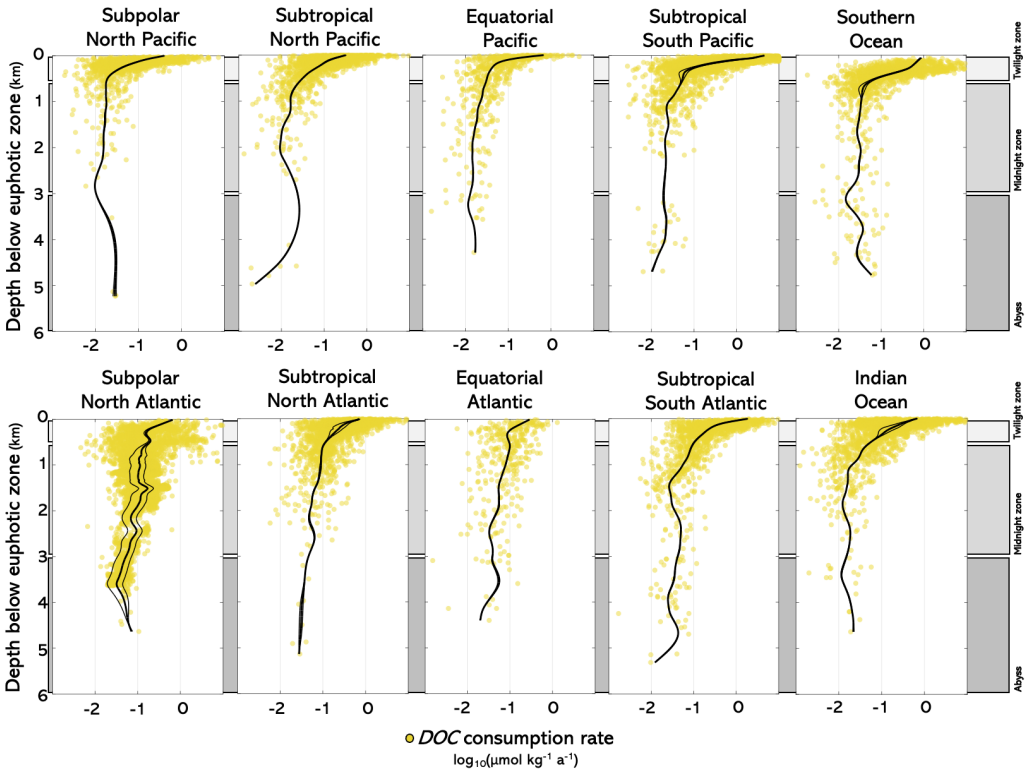

Figure 8. *DOC* consumption rate as a function of the water depth below E_z. Individual consumption rates resulting from 5000 Monte Carlo simulations are plotted as yellow circles. The thick black lines are cubic smoothing splines used to interpolate discrete rates over depth and obtain regionally harmonized depth profiles. The thin black lines are cubic smoothing splines computed from individual rates plus or minus their associated uncertainty.

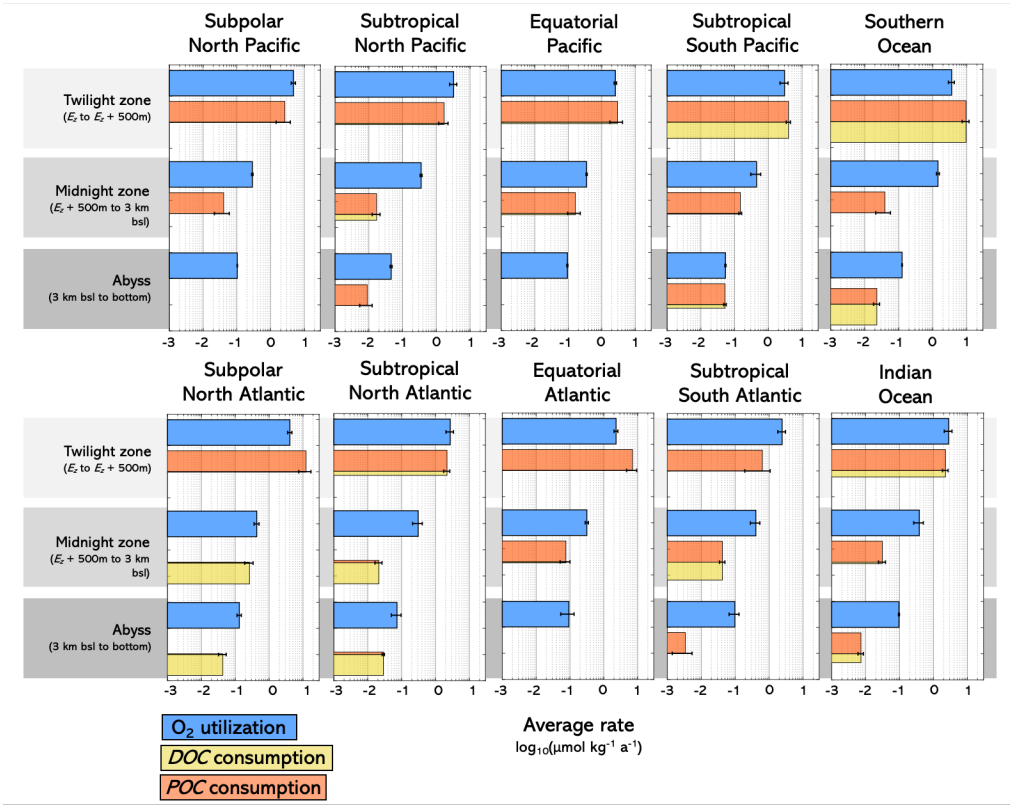

Figure 9. Regionally-averaged rates in three depth zones, the twilight zone (E_z to E_z + 500 m), the midnight zone (E_z + 500 m to 3 km depth) and the abyss (3 km depth to the bottom). All rates are expressed in µmol kg^{-1} a^{-1}. The horizontal length of both the orange and yellow bars represents the sum of the *DOC* and *POC* consumption rates. The vertical width of the orange and yellow bars represents the relative contribution of either *POC* or *DOC* consumption, respectively, to the total *OC* consumption rates. Orange and yellow bars are plotted in all regions and depth zones, but are sometimes too small to be visible. Note that the same data are also reported in Fig. 7, Table S1 and Fig. S5.

4. Discussion

4.1. Comparison with other *OUR* estimates

Most published *OUR* estimates have been derived from measurements of oxygen concentration decrease with incubation time or seawater age (Craig, 1971; Jenkins, 1982; Hinga, 1985; Sarmiento et al., 1990; Jenkins, 1998; Feely et al., 2004; Karstensen et al., 2008; Wang et al., 2021). Other estimates, however, have been obtained indirectly, by measuring the activity of electron transport systems (ETS), a chain of enzymes that passes electrons to electron acceptors such as oxygen and thus providing energy to the living cells of respiring organisms (Cammen et al., 1990). Measuring ETS activity provides the value of the oxygen consumption rate that would occur if all enzymes functioned at maximum activity (Naqvi et al., 1996; Arístegui et al., 2005). In this section, we compare oxygen consumption rates as obtained by these different approaches with ours, both regionally and globally.

Using *AOU* and seawater age estimates, Feely et al. (2004) and Karstensen et al. (2008) computed *OUR* in the Atlantic and Pacific, respectively, ranging between 2 and 10 µmol kg^{-1} a^{-1} in the twilight zone, and decreasing to ~0.1 µmol kg^{-1} a^{-1} at 1000-m depth (Fig. 5). Jenkins (1982) reported *OUR* of 4-20 µmol kg^{-1} a^{-1} in the twilight zone and 1-4 µmol kg^{-1} a^{-1} in the midnight zone of the North Pacific. Wang et al. (2021) reported *OUR* of 8.4 µmol kg^{-1} a^{-1} at a depth of 100-m depth in the South China Sea and 0.66 µmol kg^{-1} a^{-1} at 1500-m depth and also

noted a positive correlation between temperature and respiration rate. Using a tritium box model, Sarmiento et al. (1990) estimated *OUR* between 2.8 and 5.4 μmol kg^{-1} a^{-1} in the top 700 m of the North Atlantic subtropical gyre. Our twilight-zone *OUR* estimates broadly encompass these and other previously reported values. Below 2500-m depth, Hinga (1985) reported *OUR* of 0.11 μmol kg^{-1} a^{-1} in the Pacific and 0.07 μmol kg^{-1} a^{-1} in the Atlantic. Broecker et al. (1991), using O_2 and ^{14}C, report respiration rates of about 0.1 μmol kg^{-1} a^{-1} in the deep Atlantic, in waters below 2000 m. These midnight and abyssal estimates are also quantitatively consistent with our results.

In the Indian and Southern oceans, there are no directly comparable data, but there are oxygen-consumption rate estimates based on respiratory ETS activity. In the Indian Ocean, between 200 and 2400-m depth, assuming Redfieldian organic-matter stoichiometry, Naqvi et al. (1996) report ETS-based estimates of ~3.0 μmol O_2 kg^{-1} a^{-1} for the Arabian Sea and ~1.3 μmol O_2 kg^{-1} a^{-1} for the Bay of Bengal (Fig. 5). For the Indian sector of the Southern Ocean, between 200 and 1000-m depth, the ETS-based results of Arístegui et al. (2002) translate to ~2.4 μmol O_2 kg^{-1} a^{-1} (assuming Redfieldian stoichiometry). Respiration rates inferred from ETS activity thus match our estimates in terms of magnitude in the twilight zone, but strongly overestimates *OUR* at deeper depths. In fact, ETS-based estimates are likely overestimating true respiration rates because, when extrapolated globally, they provide a very high global respiration rate of 33 Gt C a^{-1} (Arístegui et al., 2003).

Integrating O_2 respiration rates over space, we find a global respiration rate below the euphotic zone of 907±165 Tmol O_2 a^{-1}. Assuming an effective molar ratio of O_2 to C of 1.3 during aerobic respiration (Redfield, 1958), this is equivalent to a respiration rate of 8.37±1.52 Gt C a^{-1}. To the degree that aphotic organic matter sources can be neglected, note this is also an estimate for what has been called "export production", a key metric of the ocean's biological pump (Primeau et al., 2013) that accounts for both *POC* and *DOC* export (*POC* and *DOC* contributions discussed in the next subsection). For comparison, integrated over the entire ocean, Antia et al. (2001)'s *POC* flux at the base of the euphotic layer is about 10 Gt C a^{-1} (Arístegui et al., 2005), and other estimates broadly range between 5 and 12 Gt C a^{-1} (Andersson, 2004; Laws et al., 2000; Dunne et al., 2007; Henson et al., 2011; Siegel et al., 2014; DeVries & Weber, 2017; Middelburg, 2019). Note, however, that the *OUR* estimates presented here in theory account for both the respiration in the water column as well as for oxygen utilization at the seafloor (see Section 4.3), and that we do not include high-latitude systems while some of the other estimates do.

As explained in the *methods section 2.5*, to test the robustness of our methods, we have duplicated our *OUR* analysis replacing *TOU* by [O_2]. The *OUR* profiles based on [O_2] (Fig. S6) have depth patterns similar to those obtained using *TOU* (Fig. 5), i.e., a steep decrease in the top kilometre of about two orders of magnitude, and a much smoother decrease below. We note that in the shallowest parts of the depth profiles, [O_2]-based *OUR* seems to consistently overestimate *TOU*-based *OUR*. However, the inferred global oxygen utilization rates based on [O_2] (1066±248 Tmol a^{-1}) and based on *TOU* (907±165 Tmol a^{-1}) are statistically indistinguishable. Overall, this suggests that the choice of respiration proxy has minor influence on the results presented in this study, and that differences in mixing representation across various proxies should not affect our conclusions. Based on a high-complexity Earth system model, Guo et al. (*under review*) have shown that in the tropical South Atlantic, between 1860 and 2100, temporal changes in water mixing patterns may affect measured oxygen utilization and water-age estimates in different ways, which leads to divergence between OUR and the true respiration rate. Even though our tracer CFC and ^{14}C-based ages

480 take mixing into account to some extent, it is worth emphasizing that OUR is simply a proxy
481 for true respiration, and that a difference between both may be present, due to unaccounted
482 small-scale transport processes.
483

484 **4.2. Organic matter cycling**

485 Our *POC* consumption rates agree with those computed from *POC* retrieved in
486 sediment traps in the Pacific (Martin et al., 1987), which range from 0.01 to 0.05 μmol $kg^{-1}a^{-1}$.
487 Reanalyzing data from Menzel & Ryther (1968), Craig (1971) reported a *DOC* consumption
488 rate of 0.029 μmol kg^{-1} a^{-1} for the NADW, which is within the range of our *DOC* consumption
489 rates from the North Atlantic midnight zone (0.020-0.056 μmol kg^{-1} a^{-1}).
490

491 Globally, we find that 511±179 Tmol of *POC* and 216±35 Tmol of *DOC* (hence
492 727±182 Tmol of total OC) are consumed in the dark water column every year. That is, *DOC*
493 consumption accounts for 30±12, 20±9 and 34±15% of organic carbon consumption (and hence
494 export production) in the twilight, midnight and abyssal zones, respectively. This DOC
495 contribution is somewhat lower than that of Pan et al. (2014) who report that up to half of *AOU*
496 was driven by *DOC* consumption in the North Atlantic, and contrasts with Jahnke (1996) who
497 reported that there is no need for *DOC* to account for deep water respiration rates. Note that
498 the presence of non-sinking *POC*, not accounted for here as it is not caught in sediment traps,
499 complicates this interpretation (Baltar et al., 2010). If deep-ocean, water-column respiration is
500 dominated by sinking particles, then this respiration is subject to sporadic, high productivity
501 events and to seasonality (Anderson & Sarmiento, 1994). In addition, the importance of *DOC*
502 as a substrate for deep-ocean, water-column respiration makes circulation changes (e.g.,
503 weakening overturning circulation; Caesar et al., 2018) an important player for deep oxygen
504 cycling, because circulation affects where and how fast *DOC* can be delivered.
505

506 *DOC* with apparent ages of 6000 years was reported in the abyssal (5710 m) subtropical
507 North Pacific (Williams et al., 1988). In abyssal regions, *DOC* concentrations show very little
508 variation around a value of about 35 μmol kg^{-1} (Fig. 4), while the mean age of seawater
509 increases (Fig. 2) along the path of water masses. Altogether, this suggests intense *DOC*
510 recycling by abyssal microbial communities. Our computed *DOC* consumption rates are in
511 general very small and highly variable across regions and depth ranges (Table S1), some being
512 negative, meaning that *DOC* is being regenerated faster than it is consumed. In the abyssal
513 realm, we note a clear negative correlation of *DOC* consumption rates with seawater mean age
514 (R^2 = 0.74, p = 0.001; Fig. 10). While abyssal regions where waters are young (e.g., North
515 Atlantic) show relatively fast *DOC* consumption, abyssal regions where waters are old (e.g.
516 North Pacific) show net *DOC* production. This confirms that dissolved organic matter lability
517 decreases with age (Middelburg, 1989) as its composition shifts from carbohydrates and
518 protein-like compounds toward more refractory lipophilic forms (Benner et al., 1992; Ogawa
519 et al., 2001; Loh et al., 2004) and supports intense abyssal *DOC* recycling. Abyssal *DOC*
520 degradation rates generally decrease with seawater age, supporting the concept of emergent,
521 rather than intrinsic, recalcitrance of dissolved organic matter proposed by Dittmar et al.
522 (2021). According to this concept, individual organic constituents are continuously reworked,
523 within complex ecological networks encompassing all trophic levels, including phytoplankton,
524 bacteria, viruses and grazers. Note that Follett et al. (2014) reported a decreasing trend in the
525 *DOC* concentration with seawater age along the path of the deep branch of the conveyor belt,
526 in which *DOC* loss is not a gradual monotonic process, but shows some variability, for instance,
527 regions with strong *POC* surface export show local abyssal *DOC* concentrations. The low

spatial resolution of our analysis prevents us from seeing such spatial variability in abyssal *DOC* consumption rates.

The deep-ocean intense *DOC* cycling reported here is mostly fueled by *DOC* subducted from the surface and originating from *POC* degradation, which should altogether represent a 1 Gt *DOC* a^{-1} source to the deep ocean (Follett et al., 2014). However, there are other *DOC* sources that complicate the interpretation of our results. Net *DOC* production in the deeper part of the water column may originate from marine sediments, which represent the main sites of organic-matter consumption and burial in the ocean (Burdige & Komada, 2015; Lønborg et al., 2020), hosting microbes in densities up to 1000 times higher than in the upper water column (e.g., Hewson et al., 2001). As a result, *DOC* concentrations in sediments are often an order of magnitude higher than in the water column (Burdige & Gardner, 1998). Thus, marine sediments act as a major *DOC* source, releasing 0.35 Gt of *DOC* a^{-1}, which is comparable to the *DOC* input from rivers (Burdige & Komada, 2015). Moreover, Luther (2021) and Yamashita et al. (2023) recently reported refractory *DOC* release from hydrothermal vents. For these reasons, the *DOC* consumption rates presented here can be interpreted as a lower bound on the true gross *DOC* consumption rate occurring in the water column.

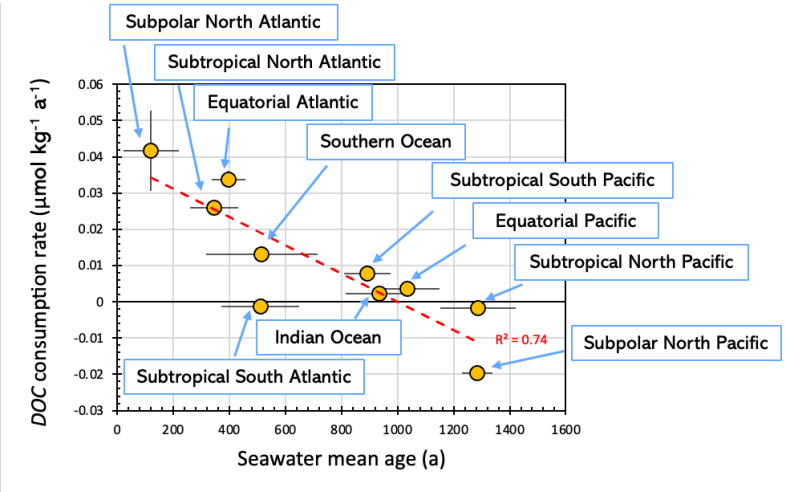

Figure 10. Regionally averaged abyssal *DOC* consumption rates as a function of regionally averaged abyssal seawater ages. Error bars represent the uncertainties associated with either *DOC* consumption rates or seawater mean age as well as the regional variability.

4.3. Seafloor respiration signal

While the *POC* consumption rates presented here should not be influenced by seafloor processes, *OUR* and *DOC* consumption-rate estimates for a given isopycnal could be affected by benthic processes if the isopycnal water mass incrops on the seafloor. In theory, seafloor respiration is reflected throughout the water column, as the oxygen being respired in the dark ocean is supplied by bottom waters. In practice, since our reconstructed *OUR* vertical profiles do not extend all the way to the ocean bottom, deeper isopycnals strongly affected by this benthic respiration may not be included in our analysis. Note that this considers ocean mixing occurring primarily along isopycnals, which is an incomplete picture since it neglects diapycnal mixing and topography-driven mixing, which may carry the oxygen deficit or *DOC* released from seafloor processes into the overlying water column.

Seafloor and total *OUR* were horizontally integrated, to obtain the vertical profiles plotted in Fig. 11. In all regions, total *OUR* declines systematically with water depth, while

seafloor oxygen consumption initially declines with water depth, but increases again because of ocean hypsometry (large parts of the ocean have depths between 3 to 6 km). Consequently, in all regions, except in the north subpolar Pacific, seafloor *OUR* can explain total *OUR* at depths below 2 to 4 km, depending on ocean basin. This pattern is very similar to that reported in Emerson and Hedges (2012) and Middelburg (2019) based on different approaches and datasets. Based on sediment oxygen consumption data, Middelburg (2019) concluded that sediment respiration dominates below 3 km depth because of hypsometry, which amplifies the seafloor respiration signal occurring for these depths. Thus, we conclude that it is very likely that the observed deep-water oxygen concentration changes reflect, to a large extent, respiration at the seafloor. That in all regions, *OUR* in the midnight zone and in the abyss always significantly exceeds the sum of *POC* and *DOC* consumption rates (Fig. 9) confirms that respiration signals from the seafloor can likely be felt even quite high in the water column.

Jahnke (1996) reported 120 Tmol O_2 a^{-1} for respiration below 1000-m depth, including 86 Tmol O_2 a^{-1} (72%) for *POC* respiration at the seafloor. According to another analysis, seafloor respiration accounts for 28% of respired O_2 below 1000-m depth (Andersson, 2004). Here, using the approach of Jørgensen et al. (2022), we find that over the 10 regions used in our study (Fig. 3a), seafloor *OUR* integrates to 74±8 Tmol a^{-1}. Overall, even though seafloor processes likely dominate total oxygen utilization in the abyss, for the entire water column, only (8.2±0.4)% (74/907) of oxygen utilization occurs at the seafloor, probably primarily through the benthic respiration of organic matter. While we interpret non-water-column oxygen utilization in the deep ocean as originating from benthic respiration, exceptions could occur near hydrothermal systems that act as a source of old and refractory *DOC* (Luther, 2021; Yamashita et al., 2023). Hydrothermal plumes also act as a source of powerful oxidants that can oxidize even the most refractory deep-ocean *POC* and *DOC* (Shaw et al., 2021). If that effect is important at a global scale, the fraction of the *POC* and *DOC* consumption rates that is due to aerobic respiration is overestimated in our interpretation.

Finally, important seafloor O_2 utilization that influences oxygen cycling throughout the water-column has implications for our understanding of the marine carbon cycle's response to environmental changes. Changes in the *POC* delivery to the seafloor in the Anthropocene could originate from multiple factors, e.g., migrations, overfishing, eutrophication/fertilization, and ocean afforestation. These perturbations would likely affect early diagenesis and benthic oxygen utilization, even at the deep seafloor. In turn, changes in benthic oxygen fluxes would be propagated throughout the water column, affecting microbial and larger heterotrophic communities populating the dark ocean.

4.4. Integrated budget

We find a global respiration rate below the euphotic zone of 907±165 Tmol O_2 a^{-1}. Subtracting from this rate the oxygen utilization rate at the seafloor (74±8 Tmol O_2 a^{-1}) gives an aphotic water-column respiration rate of 833±165 Tmol O_2 a^{-1}. Assuming a Redfield O_2:C ratio for aerobic respiration (1.3), this translates to a respiration rate of 640±127 Tmol C a^{-1}. This respiration rate is statistically indistinguishable from the global water-column organic carbon consumption rate of 727±182 Tmol C a^{-1} (511±179 Tmol of *POC* and 216±35 Tmol of *DOC*) that we derived in this study, using independent datasets. At the global scale, *OUR*, the *DOC* and *POC* consumption rates, and the seafloor oxygen utilization rates are all consistent with each other and coherent with a globally uniform O_2:C of 1.3. Even though many aspects of the marine carbon and oxygen cycles still deserve further attention, such as identifying *DOC* sources and sinks, or the fate of sedimentary organic carbon, we are now, thanks to decades of

high-quality oceanographic measurements, able to present an internally consistent integrated *OC* and O_2 budget that can be used to calibrate models and assure their validity.

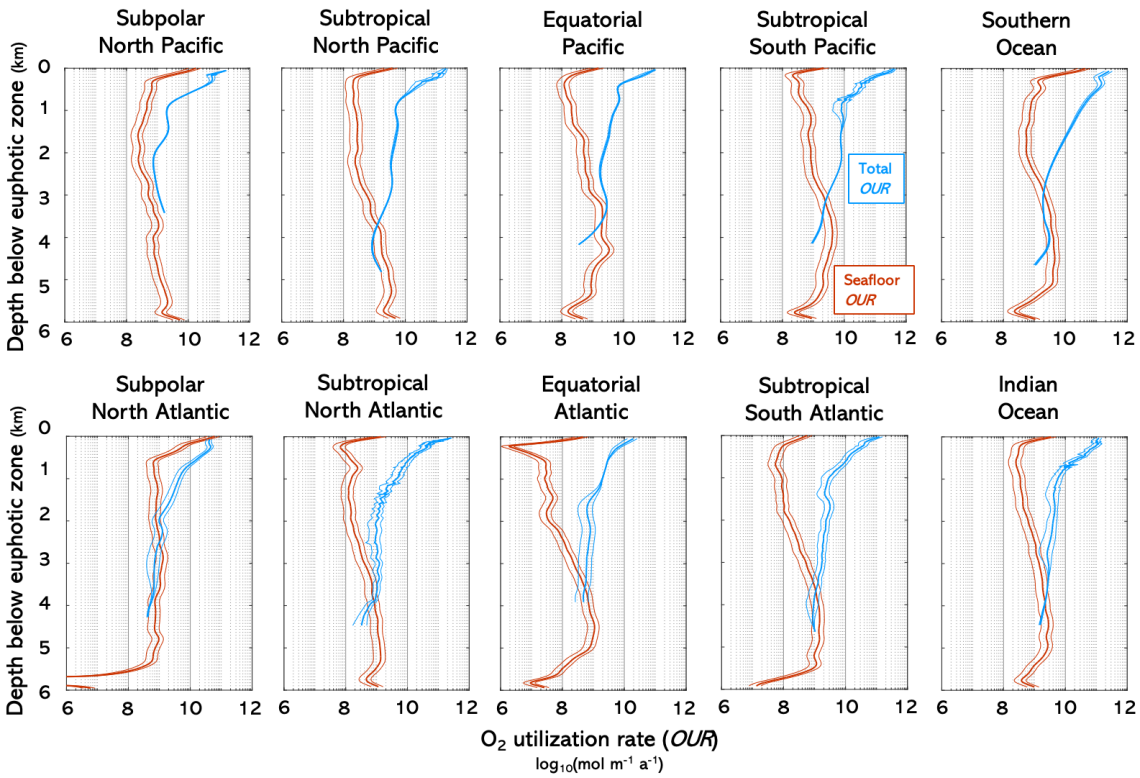

Figure 11. Regionally horizontally integrated averaged O_2 utilization rate (*OUR*) in the water-column per unit depth and at the seafloor as a function of depth below the euphotic zone. Water-column *OUR* corresponds to *TOU* changes with mean age along isopycnals, i.e., the profiles derived in this study and shown in Fig. 5. Seafloor *OUR* are computed from the methods presented in Jørgensen et al. (2022), using euphotic net primary production estimates from Oregon State University and GEBCO bathymetry.

5. Conclusion

We derived depth-profiles of oxygen utilization rate (*OUR*) and *DOC* consumption rate in 10 major biogeographical regions of the ocean. In the kilometer below the euphotic layer, *OUR* decreases by about two orders of magnitude, with the decrease being steeper in low-productivity regions such as subtropical gyres, where more *POC* is consumed near-surface and less reaches the deep ocean, than in low- and high-latitude regions. Seafloor oxygen consumption accounts for nearly all the *OUR* of the abyssal water column. *DOC* consumption rate also decreases by about two orders of magnitude in the kilometer below the euphotic zone. In the abyss, *DOC* consumption rate decreases with increasing seawater age. This is in line with the concept of emergent, rather than intrinsic, recalcitrance of dissolved organic matter. In the water-column, about a third of the respired organic carbon is *DOC* originating from subducted surface water, *POC* degradation, or seafloor and hydrothermal sources.

While our respiration rate profiles and integrated budget are improvements over earlier estimates, there remain considerable uncertainties. We anticipate that further development in the representation of ocean mixing in models will allow for more accurate products of seawater age and oxygen utilization, which may reduce the uncertainty of the respiration rates presented here. Our study also presents results across a set of biogeographical regions which could have

been defined differently and exclude high-latitude and coastal areas that should be the focus of future efforts.

We find a global *OUR* below the euphotic zone of 907±165 Tmol O_2 a^{-1}, 8% of which occurs at the seafloor. Using an Redfield O_2:C of 1.3, this translates to a respiration rate of 640±127 Tmol C a^{-1}, which is consistent with the sum of the *DOC* and *POC* consumption rates estimated in this study, i.e., 727±182 Tmol C a^{-1}. Our analysis shows that measurements of dissolved O_2 and *DOC*, seafloor O_2 utilization, and sediment-trap *POC* can all be reconciled in an integrated global budget.

Acknowledgements

This manuscript has benefited from discussions with many colleagues, in particular, members of the SCOR working group 161 ReMO (Respiration in Mesopelagic Ocean). We thank all of those who contributed to the creation of GLODAPv2 (Key et al., 2015; Lauvset et al., 2016; Olsen et al., 2016), the dissolved organic matter dataset (Hansell et al., 2021), the particulate flux dataset (Mouw et al., 2016), as well as the TTD age (Jeansson et al., 2021) and ^{14}C age (Gebbie & Huybers, 2012) products. This study has been conducted using E.U. Copernicus Marine Service Information. This research was supported by the Netherlands Organisation for Scientific Research (NWO-VENI grant VI.Veni.212.086 to O.S.) and the Netherlands Earth System Science Center. M. H. acknowledges funding from Australian Research Council (ARC) grant DP210101650.

Open research – availability statement

The TTD ages (Jeansson et al., 2021) are made available as GLODAPv2 affiliated data on the NOAA Ocean Carbon Data System website at https://www.ncei.noaa.gov/access/ocean-carbon-data-system/oceans/ndp_108/ndp108.html. Seawater chemistry data are available from the GLODAPv2.2016 in Key et al. (2015), Lauvset et al. (2016) and Olsen et al. (2016), sediment-trap data are available from Mouw et al. (2016), ^{14}C-derived ages are available from Gebbie & Huybers (2012), biome distributions are available from Fay and McKinley (2014), and the dissolved organic matter dataset is available from Hansell et al. (2015).

Supplementary materials

Table S1. Regionally-averaged rates in three depth zones, the twilight zone (E_z to E_z + 500 m), the midnight zone (E_z + 500 m to 3 km below sea level) and the abyss (3 km below sea level to the bottom). All rates are expressed in μmol kg^{-1} a^{-1}. *the rate could not be computed due to missing data, and was instead estimated as the average of the rates in all other regions of similar latitudes, e.g., all subtropical regions (see Fig. 3).

	Subpolar North Pacific	**Subtrop. North Pacific**	**Equat. Pacific**	**Subtrop. South Pacific**	**Subpolar North Atlantic**	**Subtrop. North Atlantic**	**Equat. Atlantic**	**Subtrop. South Atlantic**	**Indian Ocean**	**Southern Ocean**
O_2 utilization rate (*OUR*)										
Twilight zone	$4.8 \times 10^{0} \pm 0.7 \times 10^{0}$	$3.3 \times 10^{0} \pm 0.8 \times 10^{0}$	$2.6 \times 10^{0} \pm 0.2 \times 10^{0}$	$3.0 \times 10^{0} \pm 0.8 \times 10^{0}$	$4.1 \times 10^{0} \pm 0.6 \times 10^{0}$	$2.7 \times 10^{0} \pm 0.7 \times 10^{0}$	$2.3 \times 10^{0} \pm 0.3 \times 10^{0}$	$2.4 \times 10^{0} \pm 0.6 \times 10^{0}$	$2.8 \times 10^{0} \pm 0.7 \times 10^{0}$	$3.6 \times 10^{0} \pm 0.7 \times 10^{0}$
Midnight zone	$2.9 \times 10^{-1} \pm 0.1 \times 10^{-1}$	$3.5 \times 10^{-1} \pm 0.2 \times 10^{-1}$	$3.5 \times 10^{-1} \pm 0.2 \times 10^{-1}$	$4.5 \times 10^{-1} \pm 1.5 \times 10^{-1}$	$4.3 \times 10^{-1} \pm 0.7 \times 10^{-1}$	$3.1 \times 10^{-1} \pm 1.0 \times 10^{-1}$	$3.2 \times 10^{-1} \pm 0.3 \times 10^{-1}$	$4.1 \times 10^{-1} \pm 1.3 \times 10^{-1}$	$3.8 \times 10^{-1} \pm 1.2 \times 10^{-1}$	$1.4 \times 10^{0} \pm 0.1 \times 10^{0}$
Abyss	$1.0 \times 10^{-1} \pm 0.1 \times 10^{-1}$	$4.6 \times 10^{-2} \pm 0.3 \times 10^{-2}$	$9.5 \times 10^{-2} \pm 0.4 \times 10^{-2}$	$5.3 \times 10^{-2} \pm 0.2 \times 10^{-2}$	$1.3 \times 10^{-1} \pm 0.2 \times 10^{-1}$	$7.3 \times 10^{-2} \pm 2.3 \times 10^{-2}$	$9.3 \times 10^{-2} \pm 4.0 \times 10^{-2}$	$9.8 \times 10^{-2} \pm 3.2 \times 10^{-2}$	$9.6 \times 10^{-2} \pm 0.3 \times 10^{-2}$	$1.3 \times 10^{-1} \pm 0.1 \times 10^{-1}$
***POC* consumption rate**										
Twilight zone	$2.6 \times 10^{0} \pm 1.2 \times 10^{0}$	$1.6 \times 10^{0} \pm 0.5 \times 10^{0}$	$2.8 \times 10^{0} \pm 1.2 \times 10^{0}$	$2.2 \times 10^{0} \pm 0.2 \times 10^{0}$	$1.2 \times 10^{1} \pm 0.5 \times 10^{1}$	$1.8 \times 10^{0} \pm 0.4 \times 10^{0}$	$7.0 \times 10^{0} \pm 2.4 \times 10^{0}$	$1.3 \times 10^{0} \pm 0.4 \times 10^{0}$	$*1.7 \times 10^{0} \pm 0.4 \times 10^{0}$	$4.8 \times 10^{0} \pm 2.2 \times 10^{0}$
Midnight zone	$4.2 \times 10^{-2} \pm 1.9 \times 10^{-2}$	$1.3 \times 10^{-2} \pm 0.4 \times 10^{-2}$	$1.5 \times 10^{-1} \pm 0.6 \times 10^{-1}$	$1.4 \times 10^{-1} \pm 0.1 \times 10^{-1}$	$1.2 \times 10^{-2} \pm 0.5 \times 10^{-2}$	$2.2 \times 10^{-3} \pm 0.5 \times 10^{-3}$	$7.2 \times 10^{-2} \pm 2.4 \times 10^{-2}$	$2.3 \times 10^{-2} \pm 0.7 \times 10^{-2}$	$2.9 \times 10^{-2} \pm 0.7 \times 10^{-2}$	$3.9 \times 10^{-2} \pm 1.8 \times 10^{-2}$
Abyss	$1.6 \times 10^{-2} \pm 0.7 \times 10^{-2}$	$1.1 \times 10^{-2} \pm 0.4 \times 10^{-2}$	$-1.9 \times 10^{-2} \pm 0.8 \times 10^{-2}$	$4.4 \times 10^{-2} \pm 0.4 \times 10^{-2}$	$1.4 \times 10^{-3} \pm 0.5 \times 10^{-3}$	$3.0 \times 10^{-3} \pm 0.7 \times 10^{-3}$	$-5.7 \times 10^{-2} \pm 1.9 \times 10^{-2}$	$4.8 \times 10^{-3} \pm 1.5 \times 10^{-3}$	$5.1 \times 10^{-3} \pm 1.2 \times 10^{-3}$	$9.8 \times 10^{-3} \pm 4.5 \times 10^{-3}$
***DOC* consumption rate**										
Twilight zone	$3.0 \times 10^{-2} \pm 1.0 \times 10^{-2}$	$8.9 \times 10^{-2} \pm 2.3 \times 10^{-2}$	$1.7 \times 10^{-1} \pm 0.2 \times 10^{-1}$	$1.7 \times 10^{0} \pm 0.5 \times 10^{0}$	$2.6 \times 10^{-1} \pm 1.1 \times 10^{-1}$	$3.7 \times 10^{-1} \pm 0.8 \times 10^{-1}$	$3.9 \times 10^{-2} \pm 0.9 \times 10^{-2}$	$-6.3 \times 10^{-1} \pm 1.7 \times 10^{-1}$	$5.3 \times 10^{-1} \pm 0.9 \times 10^{-1}$	$4.8 \times 10^{0} \pm 0.4 \times 10^{0}$
Midnight zone	$-9.9 \times 10^{-4} \pm 8.9 \times 10^{-4}$	$3.7 \times 10^{-3} \pm 1.0 \times 10^{-3}$	$1.0 \times 10^{-2} \pm 0.1 \times 10^{-2}$	$5.0 \times 10^{-3} \pm 2.0 \times 10^{-3}$	$2.5 \times 10^{-1} \pm 0.7 \times 10^{-1}$	$1.9 \times 10^{-2} \pm 0.5 \times 10^{-2}$	$3.6 \times 10^{-3} \pm 4.4 \times 10^{-3}$	$1.9 \times 10^{-2} \pm 0.3 \times 10^{-2}$	$2.0 \times 10^{-3} \pm 1.8 \times 10^{-3}$	$-7.9 \times 10^{-5} \pm 251.2 \times 10^{-5}$
Abyss	$-2.0 \times 10^{-2} \pm 0.2 \times 10^{-2}$	$-1.8 \times 10^{-3} \pm 0.3 \times 10^{-3}$	$3.7 \times 10^{-3} \pm 0.3 \times 10^{-3}$	$7.7 \times 10^{-3} \pm 1.3 \times 10^{-3}$	$4.2 \times 10^{-2} \pm 1.1 \times 10^{-2}$	$2.6 \times 10^{-2} \pm 0.2 \times 10^{-2}$	$3.4 \times 10^{-2} \pm 0.2 \times 10^{-2}$	$-1.4 \times 10^{-3} \pm 1.3 \times 10^{-3}$	$2.2 \times 10^{-3} \pm 0.5 \times 10^{-3}$	$1.3 \times 10^{-2} \pm 0.1 \times 10^{-2}$

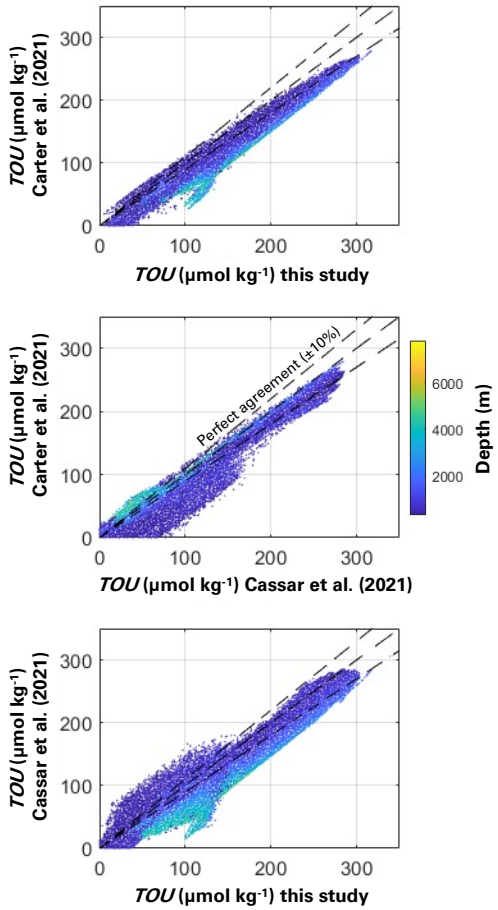

Figure S1. Comparison of *TOU* estimates from this study (GLODAPv2 and OCIM) with those from Carter et al. (2021) and Cassar et al. (2021). All data shown are deeper than 300 m and only in the defined biomes.

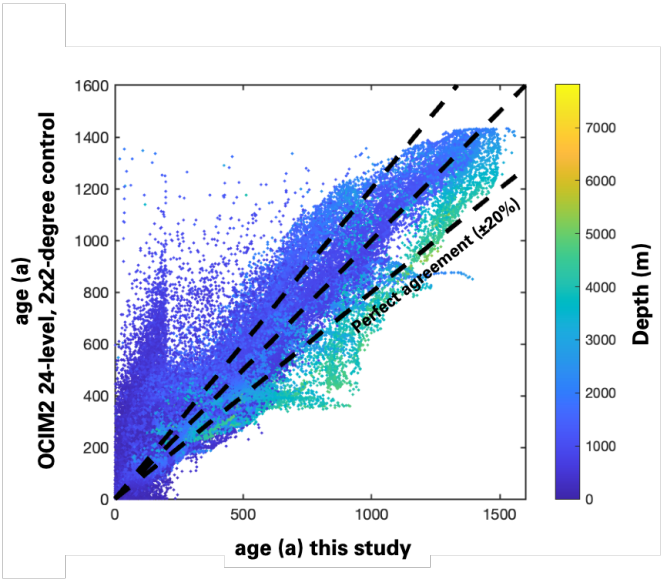

Figure S2. Comparison of seawater age estimates from this study with those from the OCIM2 model, in its 24-level, 2x2-degree control version (DeVries and Holzer, 2019).

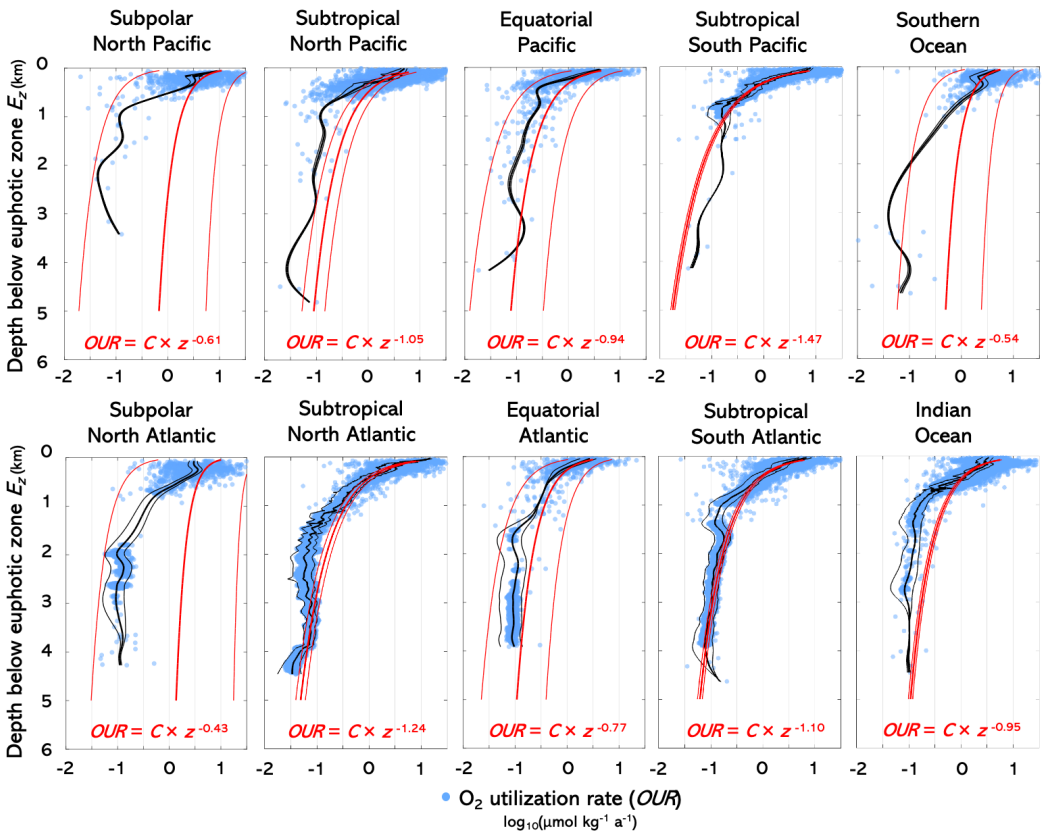

Figure S3. O_2 utilization rate (*OUR*) as a function of the water depth below E_z. Individual respiration rates resulting from 5000 Monte Carlo simulations are plotted as blue circles. The thick black lines are cubic smoothing splines used to interpolate discrete rates over depth and obtain regionally harmonized depth profiles. The surrounding thin black lines are cubic smoothing splines computed from individual rates plus or minus their associated uncertainty. Thick solid red lines are fitted power laws, whose equations are shown in the Figure, and the thin red lines represent plus or minus one uncertainty.

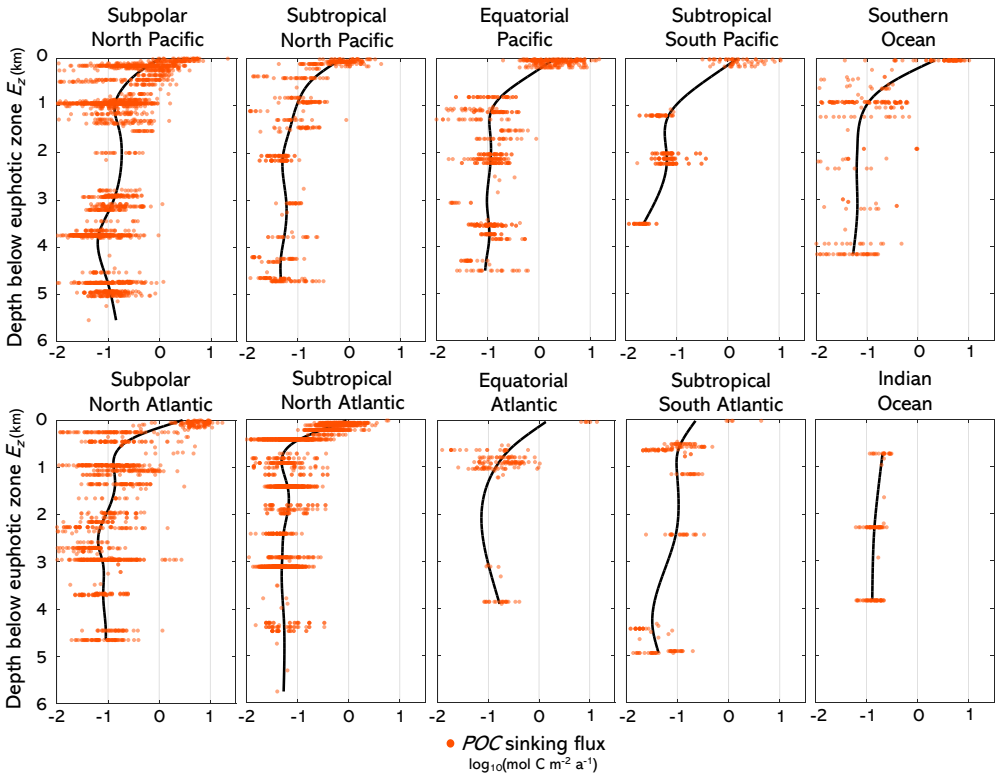

Figure S4. *POC* sinking fluxes as measured by sediment traps as a function of the water depth below E_z. Individual measurements are plotted as orange dots. The thick black lines are cubic smoothing splines used to interpolate discrete rates over depth and obtain regionally harmonized depth profiles.

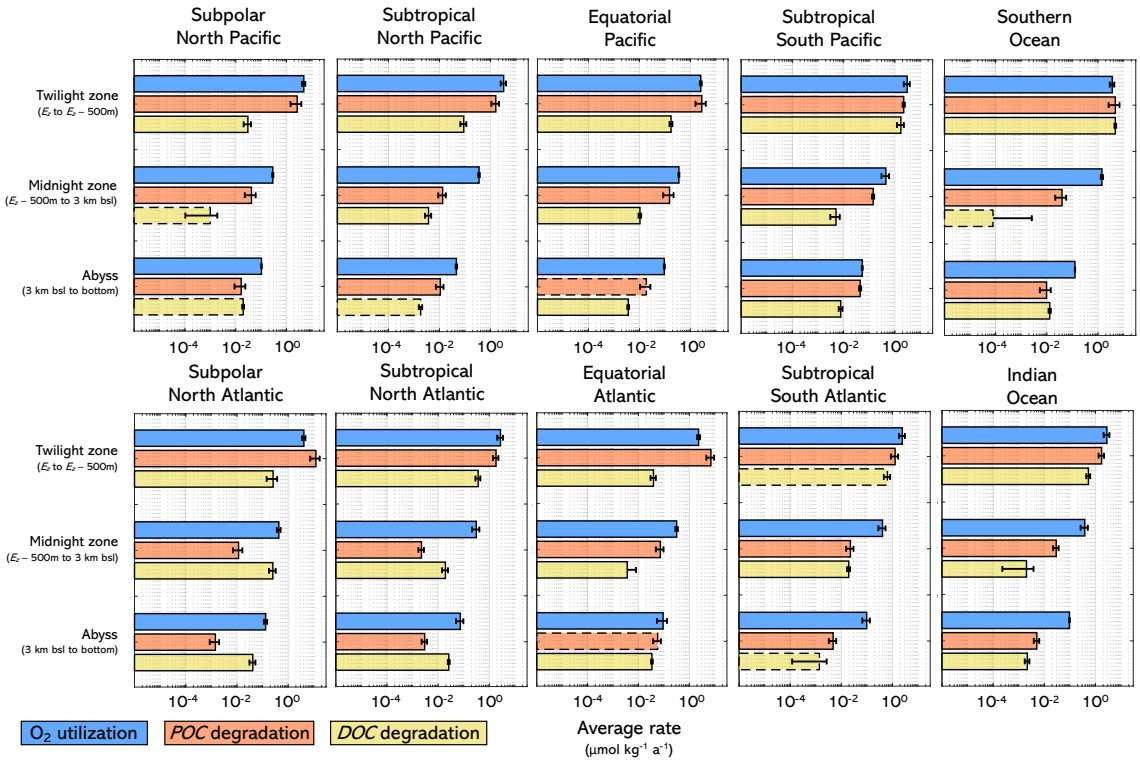

Figure S5. Regionally-averaged rates in three depth zones, the twilight zone (E_z to E_z – 500 m), the midnight zone (E_z – 500 m to 3 km below sea level) and the abyss (3 km below sea level to the bottom). All rates are expressed in μmol kg^{-1} a^{-1}. Dashed-contoured bars indicate negative values. Blue stands for oxygen utilization rate, orange is for *POC* consumption rate and yellow for *DOC* degradation rate.

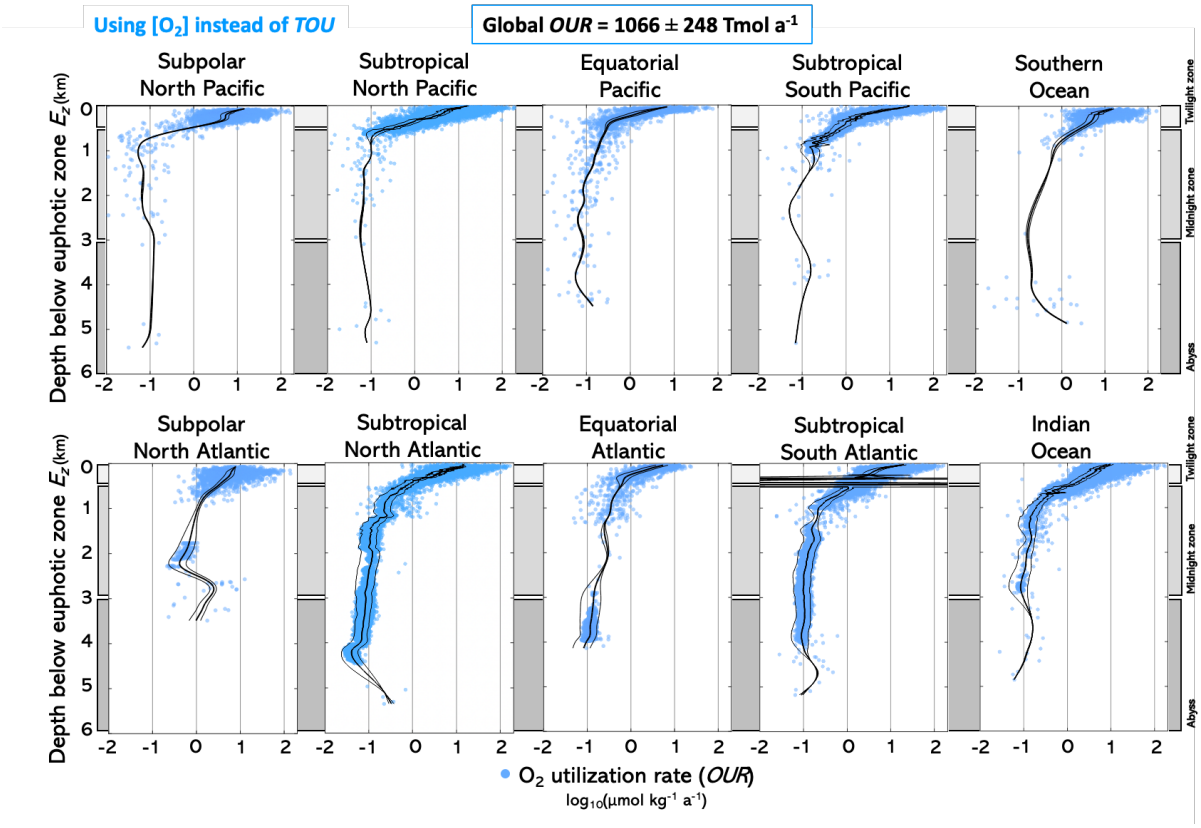

Figure S6. O_2 utilization rate (*OUR*), computed as the change in oxygen concentration [O_2] as a function of age, as a function of the water depth below E_z. This differs from the results presented in Fig. 5, in which *TOU* was used as a proxy for oxygen consumption, rather than [O_2]. Individual respiration rates resulting from 5000 Monte Carlo simulations are plotted as blue circles. The thick black lines are cubic smoothing splines used to interpolate discrete rates over depth and obtain regionally harmonized depth profiles. The thin black lines are cubic smoothing splines computed from individual rates plus or minus their associated uncertainty.

References

Anderson, L. A., & Sarmiento, J. L. (1994). Redfield ratios of remineralization determined by nutrient data analysis. *Global Biogeochemical Cycles*, *8*(1), 65–80.

Andersson, J. H., Wijsman, J. W. M., Herman, P. M. J., Middelburg, J. J., Soetaert, K., & Heip, C. (2004). Respiration patterns in the deep ocean. *Geophysical Research Letters*, *31*(3). https://doi.org/10.1029/2003GL018756

Antia, A. N., Koeve, W., Fischer, G., Blanz, T., Schulz-Bull, D., Schölten, J., Neuer, S., Kremling, K., Kuss, J., Peinert, R., Hebbeln, D., Bathmann, U., Conte, M., Fehner, U., & Zeitzschel, B. (2001). Basin-wide particulate carbon flux in the Atlantic Ocean: Regional export patterns and potential for atmospheric CO2 sequestration. *Global Biogeochemical Cycles*, *15*(4), 845–862. https://doi.org/10.1029/2000GB001376

Arístegui, J., Agustí, S., & Duarte, C. M. (2003). Respiration in the dark ocean. *Geophysical Research Letters*, *30*(2). https://doi.org/10.1029/2002gl016227

Arístegui, J., Agustí, S., Middelburg, J. J., & Duarte, C. M. (2005). Respiration in the mesopelagic and bathypelagic zones of the oceans. In P. A. del Giorgio & P. Williams (Eds.), *Respiration in Aquatic Ecosystems*.

Arístegui, J., Gasol, J. M., Duarte, C. M., & Herndl, G. J. (2009). Microbial oceanography of the dark ocean's pelagic realm. *Limnology and Oceanography*, *54*(5), 1501–1529.

Arístegui, J., Denis, M., Almunia, J., & Montero, M. F. (2002). Water-column remineralization in the Indian sector of the Southern Ocean during early spring. *Deep Sea Research Part II: Topical Studies in Oceanography*, *49*(9–10), 1707–1720. https://doi.org/10.1016/S0967-0645(02)00008-5

Baltar, F., Arístegui, J., Sintes, E., Gasol, J. M., Reinthaler, T., & Herndl, G. J. (2010). Significance of non-sinking particulate organic carbon and dark CO2fixation to heterotrophic carbon demand in the mesopelagic northeast Atlantic. *Geophysical Research Letters*, *37*(9), n/a-n/a. https://doi.org/10.1029/2010gl043105

Benner, R., Pakulski, J. D., McCarthy, M., Hedges, J. I., & Hatcher, P. G. (1992). Bulk Chemical Characteristics of Dissolved Organic Matter in the Ocean. *Science*, *255*(5051), 1561–1564. https://doi.org/10.1126/science.255.5051.1561

Berelson, W. M. (2001). Particle settling rates increase with depth in the ocean. *Deep-Sea Research II*, 49(1-3), 237–251. https://doi.org/10.1016/S0967-0645(01)00102-3

Broecker, W. S., Blanton, S., Smethie, W. M., & Ostlund, G. (1991). Radiocarbon decay and oxygen utilization in the Deep Atlantic Ocean. *Global Biogeochemical Cycles*, *5*(1), 87–117. https://doi.org/10.1029/90GB02279

Buesseler, K. O., Antia, A. N., Chen, M., Fowler, S. W., Gardner, W. D., Gustafsson, O., Harada, K., Michaels, A. F., Rutgers van der Loeff, M., Sarin, M., Steinberg, D. K., & Trull, T. (2007). An assessment of the use of sediment traps for estimating upper ocean particle fluxes. *Journal of Marine Research*, *65*, 345–416.

Buesseler, K. O., Boyd, P. W., Black, E. E., & Siegel, D. A. (2020). Metrics that matter for assessing the ocean biological carbon pump. *Proc Natl Acad Sci U S A*, *117*(18), 9679–9687. https://doi.org/10.1073/pnas.1918114117

Burdige, D. J., & Gardner, K. G. (1998). Molecular weight distribution of dissolved organic carbon in marine sediment pore waters. *Marine Chemistry*, *62*(1), 45–64. https://doi.org/10.1016/S0304-4203(98)00035-8

840 Burdige, D. J., & Komada, T. (2015). Sediment Pore Waters. In *Biogeochemistry of Marine*
841 *Dissolved Organic Matter* (pp. 535–577). Elsevier. https://doi.org/10.1016/B978-0-
842 12-405940-5.00012-1

843 Caesar, L., Rahmstorf, S., Robinson, A., Feulner, G., & Saba, V. (2018). Observed
844 fingerprint of a weakening Atlantic Ocean overturning circulation. *Nature*, *556*(7700),
845 Article 7700. https://doi.org/10.1038/s41586-018-0006-5

846 Cammen, L., Corwin, S., & Christensen, J. (1990). Electron transport system (ETS) activity
847 as a measure of benthic macrofaunal metabolism. *Marine Ecology Progress Series*,
848 *65*, 171–182. https://doi.org/10.3354/meps065171

849 Carter, B. R., Feely, R. A., Lauvset, S. K., Olsen, A., DeVries, T., & Sonnerup, R. (2021).
850 Preformed Properties for Marine Organic Matter and Carbonate Mineral Cycling
851 Quantification. *Global Biogeochemical Cycles*, *35*(1).
852 https://doi.org/10.1029/2020gb006623

853 Cassar, N., Nicholson, D., Khatiwala, S., & Cliff, E. (2021). Decomposing the Oxygen Signal
854 in the Ocean Interior: Beyond Decomposing Organic Matter. *Geophysical Research*
855 *Letters*, *48*(18), e2021GL092621. https://doi.org/10.1029/2021GL092621

856 Craig, H. (1971). The deep metabolism: Oxygen consumption in abyssal ocean water.
857 *Journal of Geophysical Research (1896-1977)*, *76*(21), 5078–5086.
858 https://doi.org/10.1029/JC076i021p05078

859 De Boor, C. (1978). *A practical guide to splines* (Vol. 27). Springer-verlag.

860 del Giorgio, P. A., & Duarte, C. M. (2002). Respiration in the open ocean. *Nature*, *420*, 379–
861 384.

862 DeVries, T. (2014). The oceanic anthropogenic CO2 sink: Storage, air-sea fluxes, and
863 transports over the industrial era. *Global Biogeochemical Cycles*, *28*(7), 631–647.
864 https://doi.org/10.1002/2013GB004739

865 DeVries, T., & Holzer, M. (2019). Radiocarbon and Helium Isotope Constraints on Deep
866 Ocean Ventilation and Mantle- ^{3} He Sources. *Journal of Geophysical Research:*
867 *Oceans*, *124*(5), 3036–3057. https://doi.org/10.1029/2018JC014716

868 DeVries, T., & Primeau, F. (2011). Dynamically and Observationally Constrained Estimates
869 of Water-Mass Distributions and Ages in the Global Ocean. *Journal of Physical*
870 *Oceanography*, *41*(12), 2381–2401. https://doi.org/10.1175/jpo-d-10-05011.1

871 DeVries, T., & Weber, T. (2017). The export and fate of organic matter in the ocean: New
872 constraints from combining satellite and oceanographic tracer observations. *Global*
873 *Biogeochemical Cycles*, *31*(3), 535–555. https://doi.org/10.1002/2016GB005551

874 Dinauer, A., Laufkötter, C., Doney, S. C., & Joos, F. (2022). What controls the large-scale
875 efficiency of carbon transfer through the ocean's mesopelagic zone? Insights from a
876 new, mechanistic model (MSPACMAM). *Global Biogeochemical Cycles*, *n/a*(n/a),
877 e2021GB007131. https://doi.org/10.1029/2021GB007131

878 Dittmar, T., Lennartz, S. T., Buck-Wiese, H., Hansell, D. A., Santinelli, C., Vanni, C.,
879 Blasius, B., & Hehemann, J.-H. (2021). Enigmatic persistence of dissolved organic
880 matter in the ocean. *Nature Reviews Earth & Environment Volume*, *2*, 570–583.

881 Dunne, J. P., Sarmiento, J. L., & Gnanadesikan, A. (2007). A synthesis of global particle
882 export from the surface ocean and cycling through the ocean interior and on the
883 seafloor. *Global Biogeochemical Cycles*, *21*(4).
884 https://doi.org/10.1029/2006gb002907

885 Duteil, O., Koeve, W., Oschlies, A., Bianchi, D., Galbraith, E., Kriest, I., & Matear, R.
886 (2013). A novel estimate of ocean oxygen utilisation points to a reduced rate of
887 respiration in the ocean interior. *Biogeosciences*, *10*(11), 7723–7738.
888 https://doi.org/10.5194/bg-10-7723-2013

889 Emerson, S. & Hedges, J. (2012). Chemical Oceanography and the Marine Carbon Cycle.
890 Cambridge University Press, Cambridge.

891 Fay, A. R., & McKinley, G. A. (2014). Global open-ocean biomes: Mean and temporal
892 variability. *Earth System Science Data*, *6*(2), 273–284. https://doi.org/10.5194/essd-6-
893 273-2014

894 Feely, R. A., Sabine, C. L., Schlitzer, R., Bullister, J. L., Mecking, S., & Greeley, D. (2004).
895 Oxygen Utilization and Organic Carbon Remineralization in the Upper Water Column
896 of the Pacific Ocean. *Journal of Oceanography*, *60*, 45–52.

897 Follet, C. L., Repeta, D. J., Rothman, D. H., Xu, L. & Santinelli, C. (2014) Hidden cycle
898 dissolved organic carbon in the deep ocean. *Proceedings of the National Academy of*
899 *Sciences*, *111*(47), 16706–16711. https://doi.org/10.1073/pnas.1407445111

900 Gebbie, G., & Huybers, P. (2012). The Mean Age of Ocean Waters Inferred from
901 Radiocarbon Observations: Sensitivity to Surface Sources and Accounting for Mixing
902 Histories. *Journal of Physical Oceanography*, *42*(2), 291–305.
903 https://doi.org/10.1175/jpo-d-11-043.1

904 GEBCO Compilation Group (2022) GEBCO_2022 Grid
905 (doi:10.5285/e0f0bb80-ab44-2739-e053-6c86abc0289c)

906 Global Monitoring and Forecast Center. (2021). *Operational Mercator Ocean*
907 *biogeochemical global ocean analysis and forecast system at 1/4 degree.*
908 https://resources.marine.copernicus.eu/?option=com_csw&view=details&product_id=
909 GLOBAL_ANALYSIS_FORECAST_BIO_001_028

910 Guo, H., Kriest, I., Oschlies, A. & Koeve, W. (under review). Can oxygen utilization rate be
911 used to track the long-term changes of aerobic respiration in the mesopelagic ocean?
912 *Authorea*, https://doi.org/10.22541/essoar.167205906.61781285/v1.

913 Hansell, D. A. (2013). Recalcitrant Dissolved Organic Carbon Fractions. *Annu. Rev. Mar.*
914 *Sci.*, *5*, 421–445.

915 Hansell, D. A., & Carlson, C. A. (2014). *Biogeochemistry of Marine Dissolved Organic*
916 *Matter*. Academic Press.

917 Hansell, D. A., Carlson, C. A., Rainer, M. W., Álvarez-Salgado, X. A., Yamashita, Y.,
918 Romera-Castillo, C., & Bif, M. B. (2021). *Compilation of dissolved organic matter*
919 *(DOM) data obtained from global ocean observations from 1994 to 2020 (NCEI*
920 *Accession 0227166)*. NOAA National Centers for Environmental Information.

921 He, Y.-C., Tjiputra, J., Langehaug, H. R., Jeansson, E., Gao, Y., Schwinger, J., & Olsen, A.
922 (2018). A Model-Based Evaluation of the Inverse Gaussian Transit-Time Distribution
923 Method for Inferring Anthropogenic Carbon Storage in the Ocean. *Journal of*
924 *Geophysical Research: Oceans*, *123*(3), 1777–1800.
925 https://doi.org/10.1002/2017jc013504

926 Helm, K. P., Bindoff, N. L., Church, J. A. (2011). Observed decreases in oxygen content of
927 the global ocean. *Geophysical Research Letters, 38*(23).
928 https://doi.org/10.1029/2011GL049513

Henson, S. A., Sanders, R., Madsen, E., Morris, P. J., Le Moigne, F., & Quartly, G. D. (2011). A reduced estimate of the strength of the ocean's biological carbon pump. *Geophysical Research Letters*, *38*(4). https://doi.org/10.1029/2011GL046735

Hewson, I., O'Neil, J. M., Fuhrman, J. A., & Dennison, W. C. (2001). Virus-like particle distribution and abundance in sediments and overlying waters along eutrophication gradients in two subtropical estuaries. *Limnology and Oceanography*, *46*(7), 1734–1746. https://doi.org/10.4319/lo.2001.46.7.1734

Hinga, K. R. (1985). Evidence for a higher average primary productivity in the Pacific than in the Atlantic Ocean. *Deep Sea Research Part A. Oceanographic Research Papers*, *32*(2), 117–126. https://doi.org/10.1016/0198-0149(85)90023-8

Holzer, M. (2022). The Fate of Oxygen in the Ocean and Its Sensitivity to Local Changes in Biological Production. *Journal of Geophysical Research: Oceans*, *127*(8), e2022JC018802. https://doi.org/10.1029/2022JC018802

Holzer, M., Smethie, W. M., & Ting, Y. (2018). Ventilation of the Subtropical North Atlantic: Locations and Times of Last Ventilation Estimated Using Tracer Constraints From GEOTRACES Section GA03. *Journal of Geophysical Research: Oceans*, *123*(4), 2332–2352. https://doi.org/10.1002/2017JC013698

Ito, T., Follows, M. J., & Boyle, E. A. (2004). Is AOU a good measure of respiration in the oceans? *Geophysical Research Letters*, *31*(17), n/a-n/a. https://doi.org/10.1029/2004gl020900

Jahnke, R. A. (1996). The global ocean flux of particulate organic carbon: Areal distribution and magnitude. *Global Biogeochemical Cycles*, *10*(1), 71–88. https://doi.org/10.1029/95gb03525

Jeansson, E., Steinfeldt, R., & Tanhua, T. (2021). *Water Mass Ages Based On GLODAPv2 Data Product (NCEI Accession 0226793)*. NOAA, National Centers for Environmental Information.

Jenkins, W. J. (1982). Oxygen utilization rates in North Atlantic subtropical gyre and primary production in oligotrophic systems. *Nature*, *300*(5889), 246–248.

Jenkins, W. J. (1998). Studying subtropical thermocline ventilation and circulation using tritium and 3He. *Journal of Geophysical Research: Oceans*, *103*(C8), 15817–15831. https://doi.org/10.1029/98JC00141

Johannes, R. E. (1965). Influence of Marine Protozoa on Nutrient Regeneration1. *Limnology and Oceanography*, *10*(3), 434–442. https://doi.org/10.4319/lo.1965.10.3.0434

Jørgensen, B. B., Wenzhöfer, F., Egger, M., & Glud, R. N. (2022). Sediment oxygen consumption: Role in the global marine carbon cycle. *Earth-Science Reviews*, *228*, 103987. https://doi.org/10.1016/j.earscirev.2022.103987

Karstensen, J., Stramma, L., & Visbeck, M. (2008). Oxygen minimum zones in the eastern tropical Atlantic and Pacific oceans. *Progress in Oceanography*, *77*(4), 331–350. https://doi.org/10.1016/j.pocean.2007.05.009

Keeling, R. F., & Garcia, H. E. (2002). The change in oceanic O2 inventory associated with recent global warming. *Proceedings of the National Academy of Sciences*, *99*(12), 7848–7853. https://doi.org/10.1073/pnas.122154899

Key, R. M., Kozyr, A., Sabine, C. L., Lee, K., Wanninkhof, R., Bullister, J. L., Feely, R. A., Millero, F. J., Mordy, C., & Peng, T.-H. (2004). A global ocean carbon climatology: Results from Global Data Analysis Project (GLODAP). *Global Biogeochemical Cycles*, *18*(4). https://doi.org/10.1029/2004GB002247

975 Key, R. M., Olsen, A., van Heuven, S., Lauvset, S. K., Velo, A., Lin, X., Schirnick, C.,
976 Kozyr, A., Tanhua, T., Hoppema, M., Jutterström, S., Steinfeldt, R., Jeansson, E.,
977 Ishii, M., Perez, F. F. & Suzuki, T. (2015). Global Ocean Data Analysis Project,
978 Version 2 (GLODAPv2), https://doi.org/10.3334/CDIAC/OTG.
979 NDP093_GLODAPv2

980 Koeve, W., & Kähler, P. (2016). Oxygen utilization rate (OUR) underestimates ocean
981 respiration: A model study. *Global Biogeochemical Cycles*, *30*(8), 1166–1182.
982 https://doi.org/10.1002/2015gb005354

983 Lauvset, S. K., Key, R. M., Olsen, A., van Heuven, S., Velo, A., Lin, X., Schirnick, C.,
984 Kozyr, A., Tanhua, T., Hoppema, M., Jutterström, S., Steinfeldt, R., Jeansson, E.,
985 Ishii, M., Perez, F. F., Suzuki, T., & Watelet, S. (2016). A new global interior ocean
986 mapped climatology: The 1° × 1° GLODAP version 2. *Earth System Science Data*,
987 *8*(2), 325–340. https://doi.org/10.5194/essd-8-325-2016

988 Laws, E. A., Falkowski, P. G., Smith Jr., W. O., Ducklow, H., & McCarthy, J. J. (2000).
989 Temperature effects on export production in the open ocean. *Global Biogeochemical*
990 *Cycles*, *14*(4), 1231–1246. https://doi.org/10.1029/1999GB001229

991 Loh, A. N., Bauer, J. E., & Druffel, E. R. M. (2004). Variable ageing and storage of dissolved
992 organic components in the open ocean. *Nature*, *430*(7002), Article 7002.
993 https://doi.org/10.1038/nature02780

994 Lønborg, C., Carreira, C., Jickells, T., & Álvarez-Salgado, X. A. (2020). Impacts of Global
995 Change on Ocean Dissolved Organic Carbon (DOC) Cycling. *Frontiers in Marine*
996 *Science*, *0*. https://doi.org/10.3389/fmars.2020.00466

997 Luther, G. W. (2021). Hydrothermal Vents Are a Source of Old Refractory Organic Carbon
998 to the Deep Ocean. *Geophysical Research Letters*, *48*(17), e2021GL094869.
999 https://doi.org/10.1029/2021GL094869

1000 Maerz, J., Six, K. D., Stemmler, I., Ahmerkamp, S., & Ilyina, T. (2020). Microstructure and
1001 composition of marine aggregates as co-determinants for vertical particulate organic
1002 carbon transfer in the global ocean. *Biogeosciences*, *17*(7), 1765–1803.
1003 https://doi.org/10.5194/bg-17-1765-2020

1004 Mare, M. F. (1942). A study of a marine benthic community with special reference to the
1005 micro-organisms. *Journal of the Marine Biological Association of the United*
1006 *Kingdom*, *25*(3), 517–554. https://doi.org/10.1017/S0025315400055132

1007 Martin, J. H., Knauer, G. A., Karl, D. M., & Broenkow, W. W. (1987). VERTEX: carbon
1008 cycling in the northeast Pacific. *Deep Sea Research Part A. Oceanographic Research*
1009 *Papers*, *34*(2), 267–285.

1010 McDougall, T. J., & Barker, P. M. (2011). *Getting started with TEOS-10 and the Gibbs*
1011 *Seawater (GSW) Oceanographic Toolbox, 28pp., SCOR/IAPSO WG127, ISBN 978-0-*
1012 *646-55621-5.*

1013 Menzel, D. W., & Ryther, J. H. (1968). Organic carbon and the oxygen minimum in the
1014 South Atlantic Ocean. *Deep Sea Research and Oceanographic Abstracts*, *15*(3), 327–
1015 337. https://doi.org/10.1016/0011-7471(68)90009-0

1016 Middelburg, J. J. (1989). A simple rate model for organic matter decomposition in marine
1017 sediments. *Geochimica et Cosmochimica Acta*, *53*(7), 1577–1581.
1018 https://doi.org/10.1016/0016-7037(89)90239-1

1019 Middelburg, J. J. (2019). *Marine Carbon Biogeochemistry: A Primer for Earth System*
1020 *Scientists*. Springer International Publishing. https://doi.org/10.1007/978-3-030-
1021 10822-9

1022 Morel, A., Huot, Y., Gentili, B., Werdell, P. J., Hooker, S. B., & Franz, B. A. (2007).
1023 Examining the consistency of products derived from various ocean color sensors in
1024 open ocean (Case 1) waters in the perspective of a multi-sensor approach. *Remote*
1025 *Sensing of Environment*, *111*(1), 69–88. https://doi.org/10.1016/j.rse.2007.03.012

1026 Mouw, C. B., Barnett, A., McKinley, G. A., Gloege, L., & Pilcher, D. (2016). Global ocean
1027 particulate organic carbon flux merged with satellite parameters. *Earth System*
1028 *Science Data*, *8*(2), 531–541. https://doi.org/10.5194/essd-8-531-2016

1029 Naqvi, S. W. A., Shailaja, M. S., Dileep Kumar, M., & Sen Gupta, R. (1996). Respiration
1030 rates in subsurface waters of the northern Indian Ocean: Evidence for low
1031 decomposition rates of organic matter within the water column in the Bay of Bengal.
1032 *Deep Sea Research Part II: Topical Studies in Oceanography*, *43*(1), 73–81.
1033 https://doi.org/10.1016/0967-0645(95)00080-1

1034 Ogawa, H., Amagai, Y., Koike, I., Kaiser, K., & Benner, R. (2001). Production of Refractory
1035 Dissolved Organic Matter by Bacteria. *Science*, *292*(5518), 917–920.
1036 https://doi.org/10.1126/science.1057627

1037 Olsen, A., Key, R. M., van Heuven, S., Lauvset, S. K., Velo, A., Lin, X., Schirnick, C.,
1038 Kozyr, A., Tanhua, T., Hoppema, M., Jutterström, S., Steinfeldt, R., Jeansson, E.,
1039 Ishii, M., Pérez, F. F., & Suzuki, T. (2016). The Global Ocean Data Analysis Project
1040 version 2 (GLODAPv2) – an internally consistent data product for the world ocean.
1041 *Earth System Science Data*, *8*, 297–323. https://doi.org/10.5194/essd-8-297-2016

1042 Oschlies, A., Brandt, P., Stramma, L., & Schmidtko, S. (2018). Drivers and mechanisms of
1043 ocean deoxygenation. *Nature Geoscience*, *11*(7), 467–473.
1044 https://doi.org/10.1038/s41561-018-0152-2

1045 Pan, X., Achterberg, E. P., Sanders, R., Poulton, A. J., Oliver, K. I. C., & Robinson, C.
1046 (2014). Dissolved organic carbon and apparent oxygen utilization in the Atlantic
1047 Ocean. *Deep Sea Research Part I: Oceanographic Research Papers*, *85*, 80–87.
1048 https://doi.org/10.1016/j.dsr.2013.12.003

1049 Pomeroy, L. R., & Johannes, R. E. (1968). Occurrence and respiration of ultraplankton in the
1050 upper 500 meters of the ocean. *Deep Sea Research and Oceanographic Abstracts*,
1051 *15*(3), 381–391. https://doi.org/10.1016/0011-7471(68)90014-4

1052 Primeau, F. W., Holzer, M. & DeVries, T. (2013). Southern Ocean nutrient trapping and the
1053 efficiency of the biological pump. *Journal of Geophysical Research: Oceans*, *118* (5),
1054 2547–2564.

1055 Redfield, A. C. (1958). The biological control of chemical factors in the environment.
1056 *American Scientist*, *46*, 205–221.

1057 Reygondeau, G., Guidi, L., Beaugrand, G., Henson, S. A., Koubbi, P., MacKenzie, B. R.,
1058 Sutton, T. T., Fioroni, M. & Maury, O. (2017). Global biogeochemical provinces of
1059 the mesopelagic zone. *Journal of Biogeography*, *45*(2), 500-514,
1060 https://doi.org/10.1111/jbi.13149.

1061 Roth, A. (2020, September 22). Bringing the Ocean's Midnight Zone Into the Light. *The New*
1062 *York Times*. https://www.nytimes.com/2020/09/22/science/monterey-bay-aquarium-
1063 midnight-zone.html

1064 Sarmiento, J. L., Thiele, G., Key, R. M., & Moore, W. S. (1990). Oxygen and nitrate new
1065 production and remineralization in the North Atlantic subtropical gyre. *Journal of*
1066 *Geophysical Research: Oceans*, *95*(C10), 18303–18315.
1067 https://doi.org/10.1029/JC095iC10p18303

1068 Sarmiento, J. L. & Gruber, N. (2006). Ocean Biogeochemical Dynamics, Princeton Univ.
1069 Press, Princeton.

1070 Shaw, T. J., Luther, G. W., Rosas, R., Oldham, V. E., Coffey, N. R., Ferry, J. L., Dias, D. M.
1071 C., Yücel, M., & Thibault de Chanvalon, A. (2021). Fe-catalyzed sulfide oxidation in
1072 hydrothermal plumes is a source of reactive oxygen species to the ocean. *Proceedings*
1073 *of the National Academy of Sciences*, *118*(40), e2026654118.
1074 https://doi.org/10.1073/pnas.2026654118

1075 Siegel, D. A., Buesseler, K. O., Doney, S. C., Sailley, S. F., Behrenfeld, M. J., & Boyd, P. W.
1076 (2014). Global assessment of ocean carbon export by combining satellite observations
1077 and food-web models. *Global Biogeochemical Cycles*, *28*(3), 181–196.
1078 https://doi.org/10.1002/2013gb004743

1079 Sonnerup, R. E., Mecking, S., & Bullister, J. L. (2013). Transit time distributions and oxygen
1080 utilization rates in the Northeast Pacific Ocean from chlorofluorocarbons and sulfur
1081 hexafluoride. *Deep Sea Research Part I: Oceanographic Research Papers*, *72*, 61–71.
1082 https://doi.org/10.1016/j.dsr.2012.10.013

1083 Sonnerup, R. E., Mecking, S., Bullister, J. L., & Warner, M. J. (2015). Transit time
1084 distributions and oxygen utilization rates from chlorofluorocarbons and sulfur
1085 hexafluoride in the Southeast Pacific Ocean. *Journal of Geophysical Research:*
1086 *Oceans*, *120*(5), 3761–3776. https://doi.org/10.1002/2015jc010781

1087 Sutton, T. T., Clark, M. R., Dunn, D. C., Halpin, P. N., Rogers, A. D., Guinotte, J., Bograd,
1088 S. J., Angel, M. V., Perez, J. A. A., Wishner, K., Haedrich, R. L., Lindsay, D. J.,
1089 Drazen, J. C., Vereshchaka, A., Piatkowski, U., Morato, T., Błachowiak-Samołyk, K.,
1090 Robison, B. H., Gjerde, K. M., Pierrot-Bults, A., Bernal, P., Reygondeau, G. & Heino,
1091 M. (2017). A global biogeographic classification of the mesopelagic zone. *Deep Sea*
1092 *Research Part I*, *126*, 85–102. https://doi.org/10.1016/j.dsr.2017.05.006.

1093 Trossman, D. S., Thompson, L., Mecking, S., Warner, M. J., Bryan, F. O., & Peacock, S.
1094 (2014). Evaluation of oceanic transport parameters using transient tracers from
1095 observations and model output. *Ocean Modelling*, *74*, 1–21.
1096 https://doi.org/10.1016/j.ocemod.2013.11.001

1097 Wang, W., Cai, M., Huang, P., Ke, H., Liu, M., Liu, L., Deng, H., Luo, B., Wang, C., Zheng,
1098 X., & Li, W. (2021). Transit Time Distributions and Apparent Oxygen Utilization
1099 Rates in Northern South China Sea Using Chlorofluorocarbons and Sulfur
1100 Hexafluoride Data—Wang—2021—Journal of Geophysical Research: Oceans—
1101 Wiley Online Library. *Journal of Geophysical Research Oceans*, *126*(8).
1102 https://agupubs-onlinelibrary-wiley-
1103 com.proxy.library.uu.nl/doi/10.1029/2021JC017535

1104 Waugh, D. W. (2003). Relationships among tracer ages. *Journal of Geophysical Research*,
1105 *108*(C5). https://doi.org/10.1029/2002jc001325

1106 Weber, T., Cram, J. A., Leung, S. W., DeVries, T., & Deutsch, C. (2016). Deep ocean
1107 nutrients imply large latitudinal variation in particle transfer efficiency. *Proc Natl*
1108 *Acad Sci USA*, *113*(31), 8606–8611. https://doi.org/10.1073/pnas.1604414113

1109 Whitney, F. A., Freeland, H. J., & Robert, M. (2007). Persistently declining oxygen levels in
1110 the interior waters of the eastern subarctic Pacific. *Progress in Oceanography*, *75*(2),
1111 179-199. https://doi.org/10.1016/j.pocean.2007.08.007
1112 Williams, P. M., Druffel, E. R. M., Williams, P., & Druffel, E. (1988). Dissolved Organic
1113 Matter in the Ocean: Comments on a Controversy. *Oceanography*, *1*(1), 14–17.
1114 Yamashita, Y., Mori, M. & Ogawa, H. (2023). Hydrothermal-derived black carbon as a
1115 source of recalcitrant dissolved organic carbon in the ocean. *Science Advances 9*(6),
1116 eade3807. https://doi.org/10.1126/sciadv.ade3807.
1117